Multilayer Thin Films for SRF Accelerating Cavities

A Dissertation

presented to

the faculty of the School of Engineering and Applied Science

University of Virginia

In Partial Fulfillment

of the requirements for the Degree Doctor of Philosophy

by

Daniel Leo Bowring

May, 2011

APPROVAL SHEET

The dissertation is submitted in partial fulfillment of the

requriements for the degree of

Doctor of Philosophy

_____

Daniel Bowring (Author)

This dissertation has been read and approved by the examining Committee:

_____

(Dissertation advisor)

_____

_____

_____

_____

_____

Accepted for the School of Engineering and Applied Science:

_____

Dean, School of Engineering and Applied Science

May, 2011

Abstract

Multilayer films on the interior of a superconducting radio frequency (SRF) accelerating cavity have the potential to increase the lower critical magnetic field H_{c1} of the bulk cavity material [A. Gurevich, *Appl. Phys. Lett.* **88**, 012511 (2006)]. A cavity with enhanced H_{c1} can tolerate higher accelerating gradients, allowing for the construction of SRF particle accelerators with lower capital costs, and more stable beams and cryogenic systems. Multilayer films are composed of alternating layers of insulator and superconductor, each of which layer is thinner than the London penetration depth of the superconductor. This dissertation presents an experimental program for the evaluation of multilayer thin films for SRF, as well as the first evaluation of such films in the RF regime. A stripline disk resonator operating at 2.8 GHz supplies field to a small, flat multilayer sample, in which the superconducting film is (Nb,Ti)N and the insulating film is Al_2O_3. By measuring the Q of the resonator, H_{c1} may be measured and compared with equivalent bulk superconducting samples.

Acknowledgements

The work I performed during the course of my dissertation was extremely interdisciplinary. Looking back, it seems like I took on a new project (and a new learning curve) every week. I've been very fortunate to work with people who were willing to help me and, more importantly, to teach me. I'd like to acknowledge their contributions here.

First, this work would not have been possible without the guidance and support of my advisor, Blaine Norum. In particular, I'd like to thank him for getting me involved with accelerator physics, a field I've found to be extremely rewarding.

I've been very lucky to work with Larry Phillips for the past five years. He's been a great teacher and a good friend. Larry, call me when you finally start selling those vegetarian hamburgers.

I could not have made any films without the assistance and advice of Anne-Marie Valente-Feliciano and Josh Spradlin. Thank you both very much.

During the experimental design phase, I had good advice from and interesting discussions with - alphabetically - Lance Cooley, Jean Delayen, Tom Goodman, and Charlie Reece. Their contributions helped to make my experimental design smoother and more efficient.

Three technicians were especially helpful to me, and regularly went out of their way for the sake of my education. Scott Williams helped me to braize my UHV heater, as well as giving me advice with other hardware issues. Teena Harris acid-etched UHV parts for me so quickly, I could barely keep up with her. And Tom Elliot taught me ion beam etching and DC magnetron sputtering.

Tom passed away recently. He was a never-ending source of jokes and stories, and kept me laughing when things in the lab got difficult. He will be missed.

Thanks very much to Xin Zhao, Kang Seo, and Olga Trofimova, who helped me with materials characterization work. And although it wasn't ultimately mentioned in this dissertation, I did a fair amount of work in mechanically and chemically polishing niobium substrates. Liang Zhao and Hui Tian helped me with some electropolishing work. Thank you both.

One of the most important lessons I learned in grad school was that research is simply not possible without strong administrative support. Very warm thanks to Carolyn Camp, Crystal Baker, Vickie Thomas, Susan Hull, Tammie Shifflet, Dawn Shifflet, and Suzie Garrett for their hard work and attention to detail.

Thanks to Jerry Floro and Bobby Weikle, who made insightful and helpful suggestions regarding my analysis. Thanks also to my editors: Paul Mattione, Larry and Esther Bowring, and Anaïs Miodek.

My family is the foundation for this work, and for all my work. To my parents, my sister, and my extended family, thank you. I promise I won't bring my computer to Thanksgiving this year.

Finally, to Anaïs Miodek: thank you. Thank you. This is as much yours as it is mine. Let's get those pictures hung up.

For my grandparents, Sol and Anna Rolnitzky.

Contents

List of symbols

A	Vector potential
A_i	Surface area, thermal shielding layer i
a	Disk radius
a_0	Lattice parameter
a_{eff}	Effective disk radius
B	Magnetic induction
c	Speed of light
$\mathbb{C}$,$\mathbb{D}$	Simulation mesh topology matrices
D	Electric displacement
d	Film thickness
E	Electric field
E_0	Electric field amplitude
E_{acc}	Accelerating electric field
E_{F}	Fermi energy
E_z	Longitudinal electric field component
e	Electron charge
e_i	Emissivity of thermal shielding layer i
F_{e}, F_{12}	Emissivity factors
FWHM	Full width at half maximum
f	Frequency
f_{nmp}	Frequency of mode (n, m, p)
G	Geometry factor
G	Gibbs free energy
H	Magnetic field (magnitude)
H_{c1}	Lower critical magnetic field, superconductor
$H_{\mathrm{c1}}^{\mathrm{bulk}}$	H_{c1} specific to bulk materials
H_{c2}	Upper critical magnetic field
H_{pk}	Cavity peak magnetic field
H_{sh}	Superheating critical magnetic field, superconductor
H_{v}	Critical field for vortex penetration, multilayer film
H_ϕ	Axial magnetic field
h	Kapitza thermal conductance
$\hbar$	Reduced Planck's constant
J	Electric current density
J_n	Bessel function of the first kind
K	Shape factor, Scherrer equation
k	Thermal conductivity
k_{B}	Boltzmann's constant
k, q	Wavenumber
k_{c}	Cutoff wavenumber
L	Total thickness of superconducting layers, multilayer film

ℓ	Mean free path
ℓ_{d}	Drift tube length
ℓ_{p}	Pillbox cavity length
M	Scattering matrix element
m	Ion mass
N	Total layers of thermal shielding
n	Charge carrier density
$\hat{n}$	Unit normal vector
P	Dissipated power
P_{c}	Power dissipated in a conductor
P_{d}	Power dissipated in a dielectric
P_{r}	Radiated power
P_{V}	Simulated volume losses, disk resonator
$P(\mathrm{N}_2)$	Nitrogen partial pressure
$p_{i,f}$	Quasiparticle momenta
Q	Quality factor
Q_0	Unloaded Q
Q_0^{sim},Q_0^{calc}	Simulated, calculated Q_0
Q_{L}	Loaded Q
$\dot{Q}$	Heat transfer rate
q	Particle charge, cyclotron equation
RRR	Residual resistivity ratio
R_0	Residual surface resistance
R_{layers}	RF surface resistance, multilayer film material
R_{bulk}	RF surface resistance, bulk material
R_{p}	Pillbox cavity radius
R_{s}	RF surface resistance
$\tilde{R}_{\mathrm{s}}$	Global RF surface resistance, multilayer film
r	Radius of curvature, cyclotron equation
S, s	Surface of integration
S_{ij}	Scattering parameter
T	Drift tube period
T	Temperature
T_{bath}	Liquid helium bath temperature
T_{c}	Superconducting critical temperature
T_{m}	Melting temperature
TE_{nmp}	Transverse electric field mode
TM_{nmp}	Transverse magnetic field mode
t	Time
$\tan\delta$	Dielectric loss tangent
U	Electromagnetic field energy
u	Position in film, normal to surface
V	Volume of integration
V_0	Voltage across disk resonator
v	Particle speed

x	Coordinate normal to cavity surface
x_{mn}	Set of zeroes for J_n
(n, m, p)	Resonant mode indices
(u_i, v_j, w_k)	Simulation mesh vertex coordinates
Y_n	Bessel function of the second kind
Z	Atomic number
β	Speed normalized to c
β	Propagation phase constant
β	Crystallite width
β_{in}, β_{out}	Cavity coupling constants
Δ	Superconducting gap energy
$\Delta\omega$	Bandwidth
Δt	Drift tube transit time
ϵ	Electromagnetic permittivity
ϵ_0	Permittivity of free space
ϵ_{eff}	Effective dielectric constant
ϵ_{r}	Dielectric constant
κ	Ginzburg-Landau parameter
λ	London penetration depth
μ	Electromagnetic permeability
μ_0	Permeability of free space
η	Wave impedance of free space
η	Vortex drag coefficient
ω	Angular frequency
ϕ_0	Magnetic flux quantum
ρ	Charge density
(ρ, θ, z)	Cylindrical coordinates: radial, azimuthal, longitudinal
$(\hat{\rho}, \hat{\theta}, \hat{z})$	Unit vectors, cylindrical coordinates
σ	Conductivity
ξ	BCS coherence length, finite ℓ
ξ_0	BCS coherence length

Chapter 1

Introduction

Multilayer thin film coatings on the interior of a superconducting radio frequency (SRF) cavity have the potential to raise the effective lower critical magnetic field H_{c1} of the bulk cavity material [1]. A cavity with enhanced H_{c1} would allow for higher accelerating fields and/or less power dissipation, enabling the construction of less expensive SRF particle accelerators with more stable beam and cryogenic parameters. To date, however, multilayer films have not been evaluated in the RF regime. This dissertation presents experimental work to evaluate the efficacy of multilayer films for use in SRF accelerating cavities.

1.1 Accelerator background

Broadly, an accelerating cavity is a conducting structure capable of supporting electromagnetic fields. The shape of the cavity determines the shape of the fields. Those fields are then used in the acceleration of charged particle beams.

SRF cavities are complex systems; their design and construction pose many physics and engineering challenges. This chapter will motivate the need for such cavities and provide some historical context. In particular, the reasons for using superconductivity (the "S" in SRF) and radio frequency power (the "RF") in cavity systems will be discussed.

1.1.1 The transition from DC to AC accelerators

Prior to the 1930s, experimenters largely used α-particles from natural radioactive sources as probes in studies of nuclear structure [2]. Between 1930 and 1933, two separate groups developed methods of direct current (DC) ion acceleration for nuclear physics research.

Cockcroft and Walton published work on "artificial disintegration" in 1932 using a 300 kV DC generator [3]. Their design was, fundamentally, a low-frequency voltage signal fed through a tube rectifier to obtain DC voltages up to 600 kV.

Then, in 1933, R.J. Van de Graaff *et al.* published work on what is now known as a Van de Graaff generator [4]. In their device, insulating conveyor belts deposited accumulated charge on spherical electrodes. The voltage between electrodes was then used to accelerate ions through a discharge tube and into various targets. In 1937, a group at the Massachusetts Institute of Technology used a pair of 40-foot-high electrodes to create a 5.1 MV static potential [5].

Two main considerations limit the performance of DC accelerators: size and corona discharge. In the former case, the above-cited 5.1 MV potential was reached by constructing electrodes so massive they had to be moved on railroad tracks and stored in an "airship dock" - an airplane hangar, essentially. In the latter case, electrons subject to large accelerating voltages may ionize ambient gas molecules resulting in a current cascade, i.e. sparking capable of damaging or destroying the experimental apparatus.

Contemporary upper voltage limits for electrostatic accelerators fall between 25 and 30 MV [6,7]. Reaching these voltages requires elaborate engineering controls. For example, dielectric breakdown may be suppressed by filling the volume between electrodes with SF_6 - a highly dielectric gas - pressurized to more than 7 atm[1]. From a practical standpoint, the problems of corona discharge and vacuum physics make electrostatic generators unsuitable for producing voltages above a few tens of MV. Electrostatic facilities are now commonly used for materials analysis (Rutherford backscattering, mass spectroscopy, etc.) and ion implantation for the semiconductor industry, for example [8].

The problems associated with large static potentials were circumvented by a series of machine designs in which one large acceleration is replaced by many smaller accelerations. This natually leads to AC accelerator designs. A prominent example of this is the cyclotron, developed by E.O. Lawrence *et al.* in the 1930s [9]. This accelerator was one of the first to use high frequency, time-harmonic accelerating fields. The now-classic cyclotron arrangement consisted of two semi-circular hollow electrodes mounted in a per-

[1] SF_6 is non-toxic and non-flammable. However, the presence of humid air or coronal discharge effects may result in the synthesis of S_2F_{10} or HF, both of which are extremely toxic.

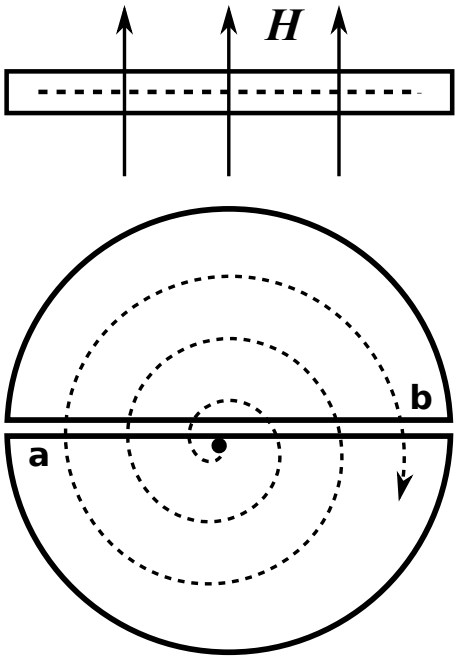

Figure 1.1: Side view (above) and plan view (below) of a typical cyclotron configuration. The applied magnetic field **H** is perpendicular to the ion's travel path (dashed line). **a** and **b** indicate points at which the ion is accelerated. While an ion travels between **a** and **b**, the voltage must change sign.

pendicular magnetic field, as in Figure 1.1. The motion of a charge q within one of the electrodes is given by the familiar cyclotron equation

$$\frac{mv^2}{r} = qvB$$

where B is the ambient magnetic inductance strength, v and m are the ion speed and mass, respectively, and r is the radius of path curvature. A potential difference across the gap between the electrodes provides the actual acceleration[2]. The voltage changes sign with a frequency such that the ions are accelerated each time they arrive at the gap: points **a** and **b** in Figure 1.1. The overall ion motion is described approximately by a spiral, with larger radii corresponding to higher kinetic energies. This approach, in which AC fields provide multiple accelerations to a beam, is the basis for RF accelerators and the associated cavities described below.

[2]The fledgling field of accelerator physics was then still establishing its units and nomenclature: Lawrence *et al.* excitedly anticipated "the production of 10,000,000 volt-protons" with this first cyclotron.

1.1.2 Drift tube accelerators

The accelerator layout most relevant to this dissertation was first conceptualized[3] by Gustav Ising in 1925 [10,11]. The design was improved upon and ultimately built by Rolf Wideröe in 1927 for his PhD thesis, for which it accelerated Na and K ions [11]. It was further developed by D.H. Sloan and E.O. Lawrence in the 1930s to accelerate Hg ions [12]. In both cases, heavy ions were chosen for acceleration. Light ions and elementary particles would ultimately accelerate to speeds approaching c - too fast for the electronic control systems that existed at the time.

In Wideröe's drift tube accelerator an array of collinear, hollow, conducting cylinders served as both the beam tube and the accelerating cavities (see Figure 1.2). The beam path was evacuated in order to maximize the mean free path of the accelerated ions. A voltage was applied to each drift tube and that voltage oscillated, setting up longitudinal, AC electric fields along the beamline.

In 1931, Sloan and Lawrence[4] used this approach to accelerate Hg^- ions to energies around 1.26 MeV [12]. This was accomplished using a series of 30 cylinders over a total path length of 1.14 m, with 10 MHz fields. The drift tubes were made progressively longer to account for the ions' acceleration. That is, the voltage phase shift between drift tubes had to be constant, regardless of ion speed. Slight errors in the oscillator control and the tube length were tuned away by variable inductances built into each tube's voltage control. Ultimately, Sloan and Lawrence concluded that the final ion energies were limited simply by the overall number of accelerating structures and the total length of the beam path.

Several features of the apparatus described in [12] are common to contemporary accelerator facilities: discrete accelerating structures (cavities) are held at a harmonically-

[3]Nuclear physics was just emerging in the 1910s and 1920s, and the limitations of natural sources were quickly apparent. Consequently, it is difficult to clearly establish who first developed the idea of "artificial" acceleration. Credit may go to the Russians L.V. Mysovskiĭ and V.N. Rukavishnikov, whose 1922 paper proposed a Tesla transformer to generate > 1 MV [10]. However, work was also presented in 1922 by A.K. Timiryazev along similar lines, and patented (but not academically published) by J. Slepian at Westinghouse, again in 1922. It seems that in the early 1920s, "artificial acceleration" was an idea whose time had come.

[4]Previous to this work, publications on drift tube accelerators were written in German or Swedish. The 1931 paper by Sloan and Lawrence is therefore discussed for convenience, being the first such work published in English.

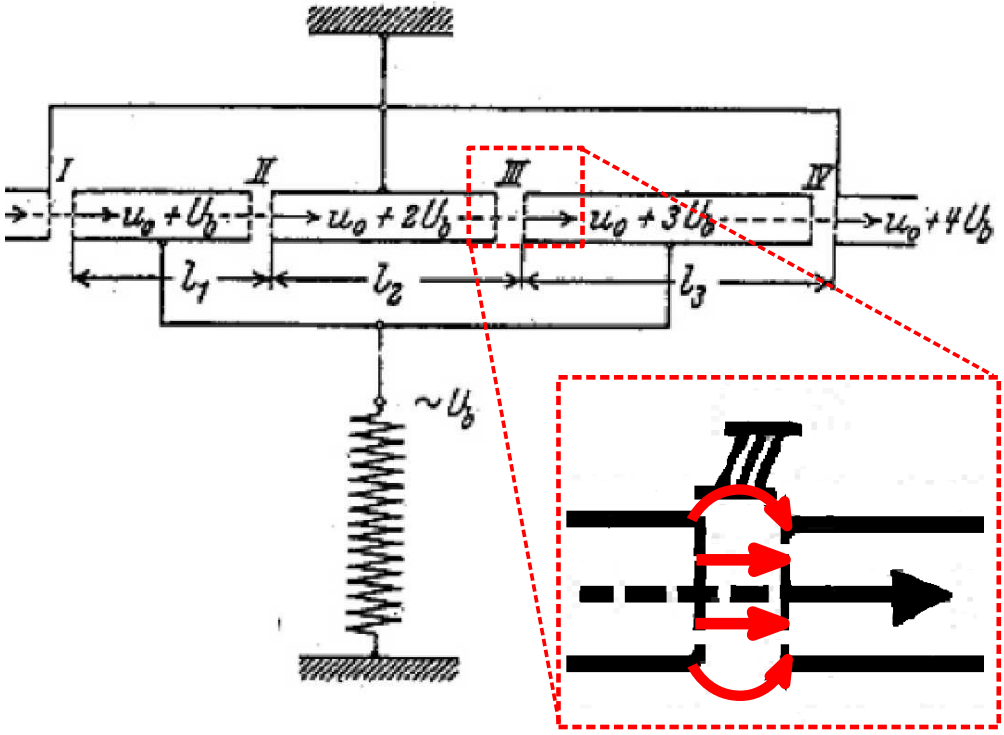

Figure 1.2: Drift tube accelerator diagram from R. Wideröe's PhD thesis, slightly modified from Reference [11]. The inset shows a closeup of the gap, with electric field lines in red. Note that the drift tubes get longer to accommodate the increasing speed of the ions.

varying potential and maintained at a fixed phase relative to each other; the beam path is evacuated in order to maximize the mean free path of accelerated particles; and the final kinetic energy of those particles is determined by each cavity's electric field strength and the overall length of the machine.

A good deal of work on accelerating structures was done during World War II, resulting in variations such as traveling-wave accelerators and multi-cell cavity structures [13][5]. Machines built in the 1950s and 1960s achieved final beam energies on the order of GeV. Contemporary machines may reach energies on the order of TeV, using cavities that operate at frequencies ranging from a few hundred MHz to several GHz (i.e. "radio frequencies").

1.1.3 The choice of RF frequencies

The previous section presents the case for AC voltage sources in accelerator applications. The drift tube accelerators discussed above, as well as most modern designs, run at radio frequencies (RF). To see why, take the example of the drift tubes shown in Figue 1.2. Ions in that design are accelerated at each gap between drift tubes: at points I, II, III, etc. Consistent acceleration occurs when the drift tube voltages are always π radians out of phase with each other - the so-called π-mode. In that mode, an ion "sees" an electric field maximum at the gap between drift tubes and is accelerated into the tube. While the ion is in the tube, the voltage of that tube must change polarity so that when the ion leaves the tube, it again sees an electric field maximum.

Consider the transit time Δt for a single particle to move from the beginning of one drift tube to the beginning of the next, a distance ℓ_{d}. During that time, the voltage on the tube must oscillate through half a period T. Assuming that the change in speed Δv is a small fraction of the total speed $v = \beta c$,

$$\begin{aligned} \Delta t &= T/2 \\ \ell_{\mathrm{d}}/\beta c &= 1/2f \\ f &= \beta c/2\ell. \end{aligned}$$

[5]Evidently, Léon Brillouin's work on electrons in periodic potentials extends past his well-known solid state work [14] to include electrons in periodic accelerating structures. See especially [15].

This relation holds true whether the above math is done in the reference frame of the drift tube or that of the particle.

Electrons in modern machines approach the speed of light almost instantly. In that case, a drift length $\ell_d = 10$ cm requires a frequency of 1.5 GHz. Lower frequencies require longer drift tubes: 100 MHz corresponds to a one-meter-long tube, and so on. RF frequencies are chosen to make the length of an accelerator and its component parts manageable[6].

Finally, note that the gap fields must radiate power, limiting the efficiency of the drift tube acceleration scheme. The problem of radiative losses at the gap is overcome by enclosing the gap between drift tubes - the region of acceleration - in a conducting surface. This is the basis for all accelerating cavities [16].

1.2 Cavity basics

The "RF" in SRF was addressed in Sections 1.1.1 and 1.1.3. In order to address the "S" an overview of cavity fundamentals is appropriate here. Various cavity parameters and figures of merit will be introduced in the context of a very simple cylindrical cavity: the "pillbox" geometry.

1.2.1 Pillbox cavities

A pillbox cavity is a hollow cylinder with closed ends, as shown in Figure 1.3. The cylindrical symmetry makes an analytic field solution possible. For simplicity, a pillbox cavity is discussed below with both a length ℓ_p and radius R_p of 10 cm.

Field solutions

The shape and frequency of the electromagnetic standing waves in a pillbox are analytically found by solving Maxwell's equations in cylindrical coordinates with boundary conditions set by the cavity walls. The following discussion is heavily abridged. For a more detailed approach, see Appendix A. Assuming a linear, isotropic medium and harmonic time-dependence $e^{i\omega t}$ with angular frequency ω for all fields, Maxwell's equations

[6] Issues unique to SRF further limit the choice of frequencies for superconducting cavities. See Section 1.2.

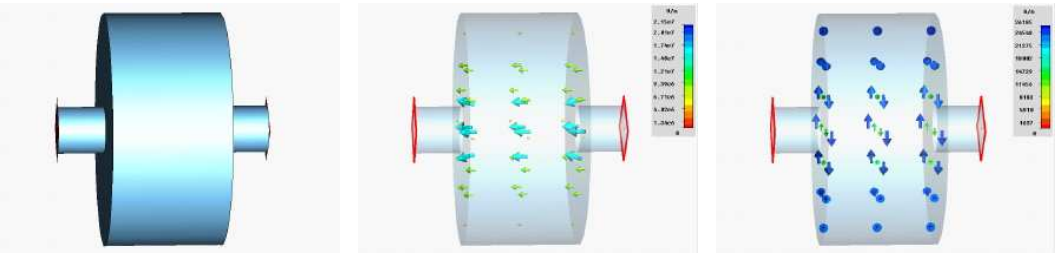

(a) Pillbox cavity. (b) Electric field lines. (c) Magnetic field lines.

Figure 1.3: Pillbox cavity operating in the TM_{010} mode.

may be written

$$\nabla \times \mathbf{E} = -\imath\omega\mu\mathbf{H} \tag{1.1a}$$

$$\nabla \times \mathbf{H} = \imath\omega\epsilon\mathbf{E} + \mathbf{J} \tag{1.1b}$$

$$\nabla \cdot \mathbf{D} = \rho \tag{1.1c}$$

$$\nabla \cdot \mathbf{B} = 0. \tag{1.1d}$$

Combining Equations 1.1a and 1.1b yields the Helmholtz wave equations

$$\left(\nabla^2 + \epsilon\mu\omega^2\right)\begin{bmatrix}\mathbf{E}\\ \mathbf{B}\end{bmatrix} = 0. \tag{1.2}$$

There are then two (coupled) sets of field solutions: one for the cases in which the electric field is longitudinal ($\mathbf{E} = E_z\hat{\mathbf{z}}$) and one in which the magnetic field is longitudinal. The former set of solutions are called transverse magnetic (TM) modes and the latter are called transverse electric (TE) modes. There are an infinite number of modes that satisfy the above equations. Modes are therefore labeled by indices according to their eigenvalues, TM_{nmp}, where n,m, and p denote field nodes along each of the basis vectors in whatever coordinate system.

In cylindrical coordinates (ρ, θ, z),

$$\frac{1}{\rho}\frac{\partial}{\partial\rho}\left(\rho\frac{\partial E_z}{\partial\rho}\right) + \frac{1}{\rho^2}\frac{\partial^2 E_z}{\partial\phi^2} + \frac{\partial^2 E_z}{\partial z^2} + \omega^2\mu\epsilon E_z = 0, \tag{1.3}$$

where the z-component of the electric field has been selected for simplicity. As with any standing wave solution in cylindrical geometry, the fields take the form of Bessel functions:

$$E_z(\rho, \phi, z) = E_0 J_n(k_c\rho)\cos(n\phi)\sin(\beta z) \tag{1.4}$$

where $k \equiv \sqrt{\omega^2 \mu\epsilon}$ and the cutoff wavenumber k_c is defined as

$$k_\mathrm{c}^2 = k^2 - \beta^2.$$

Application of the standard electromagnetic boundary conditions yields the dispersion relation

$$\frac{x_{nm}^2}{R_\mathrm{p}^2} = \omega^2 \mu\epsilon - \frac{p^2\pi^2}{\ell_\mathrm{p}^2}$$

where $k_\mathrm{c} R_\mathrm{p} = x_{mn}$, the set of zeroes to the Bessel function J_n. The resonant frequency $f = \omega/2\pi$ is then written

$$f_{nmp} = \frac{c}{2\pi\sqrt{\mu\epsilon_r}} \sqrt{\left(\frac{x_{mn}}{R}\right)^2 + \left(\frac{p\pi}{\ell}\right)^2}. \tag{1.5}$$

Implicit in the above statement is the relation between c and the dielectric constant ϵ_r. That is, $c = 1/\sqrt{\mu\epsilon_0\epsilon_r}$. The cavity material here is assumed to be nonmagnetic, such that $\mu = \mu_0$.

The indices (n, m, p) give the various eigenfrequencies of the cavity fields. The fundamental, accelerating mode is denoted TM_{010} - this field has a longitudinal electric field with no nodes, suitable for continuous acceleration through the entire length of the cavity. Since $n = p = 0$ and $\beta = 0$ for this mode, Equation 1.5 simplifies to

$$f_{010} = \frac{c}{2\pi\sqrt{\epsilon_r}} \left|\frac{x_{nm}}{R_\mathrm{p}}\right|.$$

For $\ell = 10$ cm and $\epsilon_r = 1$ (i.e. vacuum), $f_{010} = 1.1$ GHz. The magnetic field corresponding to Equation 1.4 is found directly using Maxwell's equations, specifically Equation 1.1a. For the TM_{010} mode,

$$\mathbf{H}(\mathrm{TM}_{010}) = -\frac{iE_0}{\eta} J_1(k\rho)\hat{\phi} \tag{1.6}$$

where $\eta = \sqrt{\mu/\epsilon} = 377\ \Omega$ is the wave impedance of free space.

Stored energy and power dissipation

The energy U stored in the cavity fields can be found from Equation 1.4 or 1.6. Solving for U in terms of the magnetic fields will be useful later on, so that approach will be followed below. Since the time-averaged field energy is distributed equally between electric and magnetic fields,

$$U = \frac{1}{2}\mu \int_\mathrm{V} |\mathbf{H}|^2 dV \tag{1.7}$$

for a volume of integration V. The integral is done by substituting Equation 1.6 and using the identity

$$\int J_\nu(\alpha\rho)\rho d\rho = \frac{\rho^2}{2}\left[J_\nu^2(\alpha\rho) - J_{\nu-1}(\alpha\rho)J_{\nu+1}(\alpha\rho)\right].$$

Given the boundary condition $J_0(kR) = 0$ discussed above, the second term on the right vanishes, so

$$U = \frac{\pi\ell_\mathrm{p}\mu R_\mathrm{p}^2 E_0^2}{2\eta^2} J_1^2(kR_\mathrm{p}). \tag{1.8}$$

The power P dissipated by the cavity walls is

$$P = \frac{1}{2}\langle R_\mathrm{s}\rangle \int_S |\mathbf{H}|^2 dS. \tag{1.9}$$

Here, $\langle R_\mathrm{s}\rangle$ is the normalized average value of the surface resistance over the whole cavity. This discussion assumes that the surface is uniform, so $\langle R_\mathrm{s}\rangle = R_\mathrm{s}$. The integral is evaluated on a surface S that includes the walls of the cavity at $\rho = R$ as well as those at $z = 0, \ell$. Then

$$P = \frac{R_\mathrm{s}E_0^2}{2\eta^2}\left[2\pi R_\mathrm{p}^2 J_1^2(kR_\mathrm{p}) + \ell_\mathrm{p}R_\mathrm{p}J_1^2(kR_\mathrm{p})\right]. \tag{1.10}$$

Quality factor Q

A common metric for comparing cavities - or any resonator - is the quality factor, Q. The Q-value is, roughly speaking, a dimensionless measure of the efficiency of a cavity,

$$Q_0 = \omega\frac{U}{P}. \tag{1.11}$$

The subscript denotes an "unloaded" Q which describes only the cavity and not the surrounding components or the beam being accelerated. A loaded Q_L would account for beam loss, inter-cavity coupling, and other, more elaborate loss mechanisms. Q_0 is large when the cavity stores large amounts of energy and the cavity walls dissipate very little power. A commonly-cited example of a high-Q structure is a bell that rings clearly for a long time after being struck.

Using Equations 1.8 and 1.10, the Q_0 of the pillbox cavity in the TM_{010} mode is then

$$Q_0 = \frac{\omega\mu\ell_\mathrm{p}R_\mathrm{p}}{2R_\mathrm{s}(R_\mathrm{p} + \ell_\mathrm{p})}. \tag{1.12}$$

The above expression for Q can be written as the product of two factors, one which is *a priori* calculable and one, R_s, which is not. The surface resistance may be estimated from first principles or from tables and handbooks, but an exact value depends heavily on factors like material quality and surface preparation. Since these properties can vary significantly from sample to sample, precise value of R_s must be measured. This leads naturally to another figure of merit, the geometry factor G:

$$Q_0 = \frac{G}{R_\mathrm{s}}. \tag{1.13}$$

For the pillbox in question, $G = \omega\mu\ell_\mathrm{p}R_\mathrm{p}/2(R_\mathrm{p} + \ell_\mathrm{p}) = 227\ \Omega$. (Geometry factors for the CEBAF 1.5 GHz cavities are around 290 Ω.) In the TM_{010} mode, $f \propto 1/R_\mathrm{p}$ which suggests that G is entirely a measure of the aspect ratio of a cavity, and can be calculated or simulated from first principles. Measuring Q using, for example, a vector network analyzer will then give a precise value for R_s.

Q_0 is then a way of gauging the efficiency - so to speak - of a cavity. It also determines the fractional bandwidth:

$$Q_0 = \frac{\omega_0}{2\Delta\omega}. \tag{1.14}$$

Equation 1.14 is derived from the generalized resonator lumped circuit model.

Resonant electron loading and non-pillbox cavity geometries

Multipacting is a resonant process by which stray electrons impact the inner walls of a cavity and secondary electrons are emitted[7]. If the whole process occurs in phase with the RF fields, a resonant positive feeback can occur: a cloud of electrons builds up in the cavity and draws energy from the fields, sharply lowering the cavity's Q [19]. Note that this is a much more significant phenomenon in superconducting cavities. Since resistive losses are negligible in superconducting cavities, other phenomena like multipacting become evident. Normal-conducting cavity losses are dominated by other factors. Since multipacting informs modern SRF cavity design and drives the departure from more elementary geometries, a brief discussion is appropriate here.

[7]The word itself is a modification of "multipactoring", which seems to have been coined by Philo T. Farnsworth, the inventor of television. He published a series of patents in the 1930s that described amplifiers based on intentional multipactoring. [17, 18].

The process by which "stray" electrons enter the cavity, and by which secondary electrons are emitted, can be described to arbitrary levels of complexity. In particular, the number of secondary electrons emitted per primary impact is a complicated function of the kinetic energy and incident angle of the primary; the relative phase between the cavity fields and the primary electron orbit; the electric field strength; and the surface quality of the cavity. This latter issue is very involved, and depends heavily on the composition and abundance of the oxides (NbO, Nb_2O_5) and atmospheric adsorbates (H_2O, CO_2, etc.) on the inner cavity surface. These surface compounds affect the yield of secondary electrons, but may also alter the time that secondaries require for emission, therefore changing the phase relationship between secondaries and cavity fields [20].

In practice, multipacting is modeled with computer codes and measured in high-power cavity tests via thermometry and spectral analysis [21, 22]. The introduction of curved cavity geometries, first spherical and then elliptical, as well as surface treatment techniques, have essentially renderend multipacting a non-issue in $\beta = 1$ cavities[8] [23]. The choice of an elliptical geometry also reduces the ratio of peak magnetic field to accelerating electric field $H_{\rm pk}/E_{acc}$ (see Section 1.5) and facilitates the easy flow of chemical etchants and rinses through a multi-cell cavity [24].

Elliptical cavity geometries are now standard for $\beta = 1$ applications. Examples include the Continuous Electron Beam Accelerator Facility (CEBAF) at Thomas Jefferson National Accelerator Faciliy [25], the Cornell Electron Storage Ring (CESR) [26], the Spallation Neutron Source (SNS) at Oak Ridge National Laboratory [27], the Large Hadron Collider at CERN [28], the planned Internaitonal Linear Collider (ILC) [29], and many others. A standard elliptical 5-cell, 1.5 GHz CEBAF cavity is shown in Figure 1.4a. The electric field within a single cell is shown in Figure 1.4b and the corresponding magnetic field is shown in Figure 1.4c.

1.3 Superconducting Cavities

This section addresses the choice of superconducting materials for RF cavities. It also presents a brief overview of the phenomenology and theory of superconductivity.

[8] $\beta = v/c = 1$.

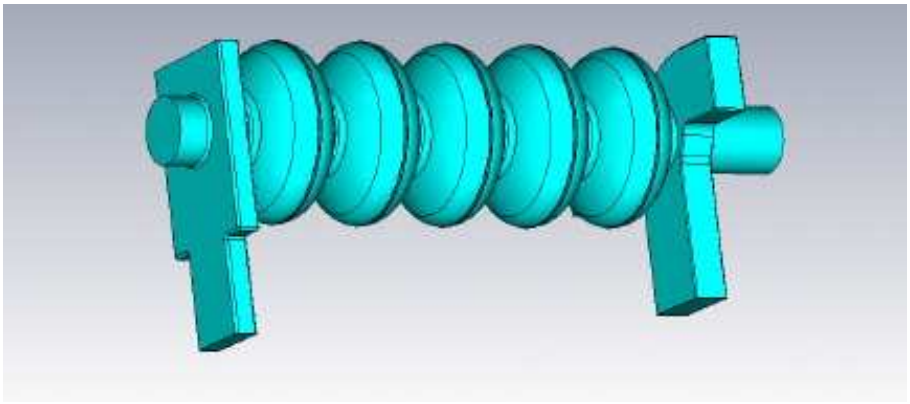

(a) Simulation (CST Microwave Studio) of a CEBAF 5-cell cavity. At the left-hand side is the input RF power coupler. On the right-hand side is the HOM output coupler.

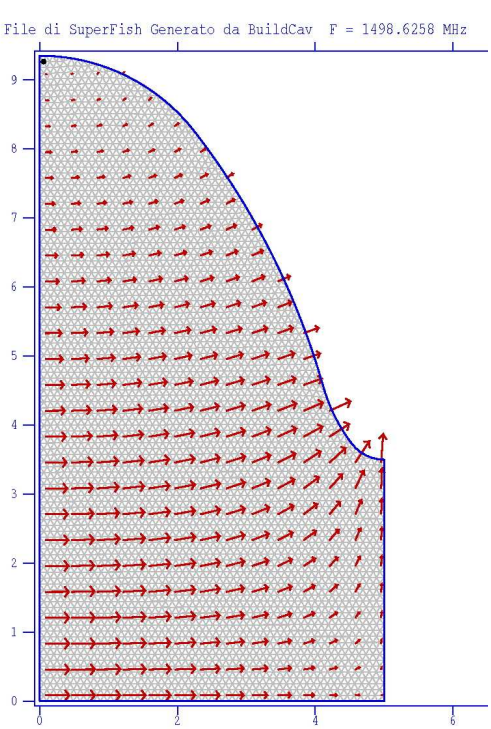

(b) Electric field lines (red) in CEBAF cavity.

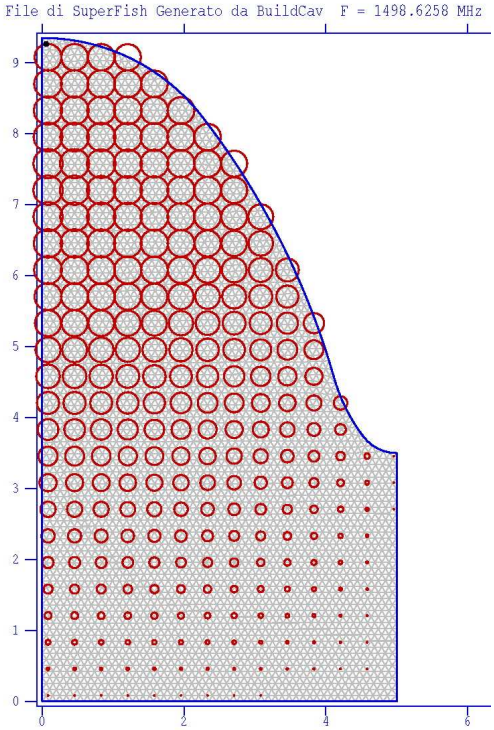

(c) Magnetic field lines (red) in CEBAF cavity.

Figure 1.4: Simulations of a standard 5-cell 1.5 GHz CEBAF Nb cavity, showing mechanical and field structures. The average accelerating field in such a cavity is 7.5 MV/m and the unloaded $Q \approx 4 \times 10^9$. For the Poisson SuperFISH finite element simulations (b) and (c), cell boundaries are shown in blue, field lines are shown in red, and gray lines show the finite element mesh. The simulation exploits the vertical and horizontal symmetries of the cavity: only a quarter of the cross section is shown. The beam line runs along the horizontal axis. Axes show size in cm. Thanks to G. Ciovati for providing the initial input file for this simulation.

1.3.1 Room temperature vs. superconducting accelerators

Whether an accelerator uses superconducting or normal conducting cavities depends on specific physics goals, as well as environmental[9], political, and budgetary constraints [25,30,31]. Copper is typically used for room temperature machines since it is highly conductive, cheap to buy, and easy to machine. However, at continuous, high RF gradients, copper cavities dissipate a significant amount of power.

To some extent this dissipation can be ameliorated by lowering the duty cycle of the beam, which is the ratio between the time the beam is on and the total elapsed time. A beam with a duty cycle of unity is referred to as operating in continuous wave (CW) mode. Normal conducting cavities with duty cycles on the order of 10^{-5} have reached accelerating gradients well in excess of 100 MV/m [32]. The choice between this type of pulsed-power acceleration and CW operation is made based on desired physics measurements and on detector design considerations. For example, in CEBAF, electrons are scattered off a target nucleus, perhaps liberating nucleons or mesons in the process. Establishing which liberated nucleons coincide with which scattered electrons is termed a coincidence measurement [33]. In pulsed-power accelerators, many electrons arrive simultaneously at the target, making such coincidence measurements very difficult. CW machines supply a more diffuse, continuous stream of electrons, facilitating such measurements.

Superconducting cavities were first used in the 1970s in order to achieve high-energy, continuous beams [34]. For CW machines, liquid helium is used to cool superconducting cavities down to a few degrees Kelvin, below their critical temperature[10]. Since currents flow without resistance in a superconductor, power dissipation is much less of a concern in SRF cavities.

Normal vs. superconducting pillbox cavity

Consider the pillbox cavity introduced in Section 1.2.1. Cavities constructed from different materials but with identical geometries will have varying Q values depending on their various surface resistances R_s, as in Equation 1.11. An expression for the surface resistance

[9] Here, "environmental" refers to seismic stability, land availability, etc.

[10] The critical temperature T_c is the temperature below which a superconductor has zero electrical resistivity.

of a "good" normal conductor, i.e. one with minimal attenuation, comes straight out of Maxwell's equations: $R_s = \sqrt{\omega\mu_0/2\sigma}$ where σ is the conductivity. Copper then, at 1.1 GHz, has a surface resistance of approximately 9 mΩ. Calculating the RF surface resistance of a superconductor from first principles is not at all straightforward [35]. This issue will be addressed in more detail later; for now, a rough estimate of 20 nΩ is adequate [36].

In addition to reduced power consumption, accelerators may use SRF technology for reasons of operational cost reduction,[11] improved beam quality, and linac stability [25, 31, 36, 37].

1.4 Superconductivity basics

Phenomenological aspects of superconductivity are reviewed here, along with some rudimentary theoretical background. Only the issues relevant to this dissertation are discussed. For a rigorous treatment, see References [38–40].

Superconductivity is a second-order phase transition (that is, a discontinuity in the heat capacity at some critical temperature) occurring in some materials. This phase transition is characterized by zero DC electrical resistivity below some critical temperature T_c. Such a transition was first observed by Heike Kamerlingh Onnes in 1911, when he and his lab staff cooled mercury down to liquid helium temperatures and measured a complete loss of resistivity below 4.2 K.

As the resistivity vanishes, surface currents are able to instantaneously compensate for any applied magnetic fields. Superconductors therefore exhibit perfect diamagnetism in addition to perfect conductivity. Interior magnetic fields are expelled from the material's interior and external, applied fields are screened. This is known as the Meissner effect.

The London penetration depth is a consequence of the perfect diamagnetism of a superconductor. Beneath the surface of a superconductor, fields decay like $e^{-x/\lambda}$ where x is the coordinate normal to the surface. λ is the London penetration depth, analogous to the skin depth of a normal conductor. Kittel [41] treats the interaction between a plane wave vector potential $\mathbf{A}(\mathbf{x}) = e^{i\mathbf{q}\cdot\mathbf{x}}$ and the ground state of a superconductor. The

[11] Dissipated power is related to cost reduction, but the two are not isomorphic. See Section 1.5.2.

resulting relationship between the vector potential **A** and the current density **j** is termed the London equation

$$\mathbf{J}(\mathbf{x}) = -\frac{ne^2}{m}\mathbf{A}(\mathbf{x})$$

after F. and H. London, who obtained the same result through phenomenological arguments in 1935 [42]. In the above equation, n, m, and e refer to the density, mass, and charge of charge carriers, respectively. Using Ampere's Law (Equation 1.1b) this can be written as

$$\nabla^2\mathbf{H} = \frac{1}{\lambda^2}\mathbf{H}$$

or, in one dimension,

$$\mathbf{H} = \mathbf{H_0}e^{-x/\lambda}. \tag{1.15}$$

Implicitly, $\lambda^2 = m/ne^2\mu$ in MKS units. The London penetration depth for bulk Nb at $T = 0$ K is 36 nm. In other materials, the penetration depth varies widely: thin aluminum films may have $\lambda \sim 14$ nm while less conventional organic superconductors have demonstrated penetration depths on the order of mm [43, 44].

In general, the transition from the superconducting state to the normal conducting state can be mediated by an increase in temperature, magnetic field, or electrical current above some critical value. For example, the upper RF critical field of bulk Nb is approximately 180 mT. Above this field, a cavity can be expected to "quench" - that is, be driven into the normal state.

The first theory of superconductivity was presented in 1957 by Bardeen, Cooper, and Schrieffer [45]. In broad terms, the so-called BCS theory demonstrates a bound state with energy $E < E_\mathrm{F}$ below the Fermi energy E_F for electron pairs ("Cooper pairs"), given an arbitrarily weak attractive two-body potential. For superconductors such as Nb, this attraction between electrons comes from a combination of (a) an interaction between lattice phonons and Cooper electrons; and (b) a screening of the typical electronic Coulomb repulsion by the surrounding conduction electrons. The end result is a non-local attraction between two electrons which, together, act roughly as a single charge-carrying boson for supercurrents. The size of a Cooper pair is characterized by the coherence length ξ_0. For Nb, $\xi_0 = 39$ nm. In imperfect crystals, for which the mean free path ℓ of

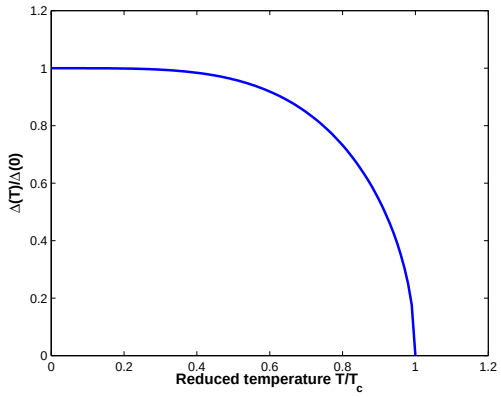

Figure 1.5: Approximate temperature dependence of the gap size Δ for a generic superconductor, as a function of reduced temperature T/T_c.

electron motion is significant, $1/\xi = 1/\xi_0 + 1/\ell$. Note that in both cases, the coherence length is much larger than any realistic interatomic spacing, such that it is possible for many Cooper pairs to overlap each other within a superconductor.

In practice, Equation 1.15 is only valid for superconductors that operate in the local limit. If $\lambda \gg \xi$, then the vector potential $\mathbf{A}$ will vary over the characteristic size ξ of a Cooper pair, complicating the expected value of λ.

The bound state energy E is typically within $k_\mathrm{B}T_\mathrm{c}$ of E_F. Above the Fermi surface, there exists an energy gap 2Δ - the energy required for pair breaking. This gap is one way to characterize the supercondcting state. The temperature dependence of Δ is shown in Figure 1.5 and illustrates temperature-mediated transitions from the superconducting to the normal conducting state. Niobium is a strong candidate for SRF applications because it has a relatively large gap: $\Delta(0)/k_\mathrm{B}T_\mathrm{c} = 1.9$ [36].

One last phenomenon relevant to the current discussion of SRF cavities is the issue of magnetic surface energy. As the strength of an applied magnetic field increases, the Meissner effect breaks down and some flux may penetrate the superconductor. Materials are classified as either Type I or Type II, depending on whether the interface between superconducting and normal regions has positive or negative surface energy, respectively. For Type II materials, the free energy is minimized by a maximization of the surface area between SC and NC regions. This manifests physically as a regular distribution

of flux vortices. These are quantized, much like charge, in units of the flux quantum $\phi_0 = 2.07 \times 10^{-15}$ T·m^2, with a size approximately equal to the coherence length ξ. Type II superconductors are then characterized by two critical magnetic fields: a lower critical field H_{c1}, above which magnetic flux vortices penetrate; and an upper critical field H_{c2} above which the material is driven into the normal conducting state. Below H_{c1}, the Meissner effect is perfect and no flux penetrates.

It is possible for the superconducting state to persist metastably above H_{c2}, up to the superheating critical field H_{sh}. There is some suggestion in the literature that this field, and not H_{c1}, is the limiting field of superconducting cavities [46, 47]. The H_{c1}-vs-H_{sh} debate is beyond the scope of this dissertation. Since surface defects and impurities can restrict cavity operation to fields well below H_{c1}, the lower critical field will be treated as the limiting field in this dissertation.

1.5 SRF cavities

SRF cavities make possible a wider variety of accelerator designs and may allow a significant power savings in the process. However, there are certain issues unique to SRF cavities that must then be addressed. In particular, the choice of material in cavity fabrication is very important. The following section motivates the use of Nb as a cavity material, as well as the limitations of that material.

1.5.1 Niobium for SRF cavities

Bulk niobium is used in virtually all SRF machines now operating. Some low-gradient cavity designs, such as those at SUNY Stony Brook in New York or the University of Washington in Washington state, have used lead/tin resonators as a way to reduce capital costs [48]. However, for high-gradient, low-loss applications, Nb is the clear material of choice [49]. Among the thousands of known superconductors, SRF cavity applications are practically restricted to the elemental superconductors. Difficulties related to stoichiometry and formability, as well as low values of H_{c1}, make the use of even the relatively well-understood B1 and A15 compounds non-trivial in bulk applications[12]. Nb, by con-

[12]Recent promising efforts with bulk Nb_3Sn have been presented [50]. This approach is still very much in the R&D phase and, as a general rule, Nb is used for cavity fabrication.

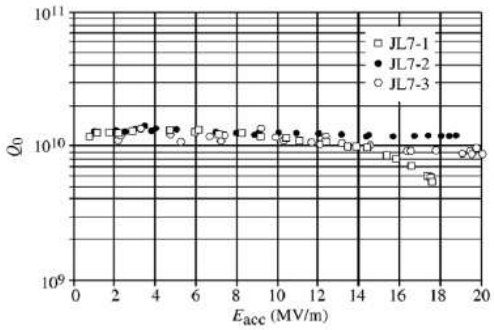

Figure 1.6: Q vs. E curve for 7-cell CEBAF upgrade cavities [51].

trast, can be mined in large quantities, refined, and formed with conventional machines. Furthermore, it is the elemental superconductor with the highest critical temperature T_c (9.2 K) and the highest critical field H_c. It also has a relatively large energy gap Δ, as discussed in the previous section.

1.5.2 Q vs. E curves

As discussed in Section 1.3.1, P is typically very small for superconductors, resulting in measured Q-values on the order of 10^{10}. As the accelerating field E increases, field-dependent phenomena like multipacting may dissipate power in the form of heat, raising the local temperature, driving sections of the cavity into the normal state, and precipitating a quench. So-called Q vs. E curves demonstrate cavity performance limits. The shape of such a curve may assist in the diagnosis of multipacting or field emission [36]. An example of such a curve is shown in Figure 1.6. A Q vs. H curve looks very similar, and can be used to determine the lower critical field H_{c1} of an SRF cavity. This will be discussed in more detail in later chapters.

1.6 Limitations of bulk Nb

Although SRF cavities present some advantages to their normal conducting counterparts, there are limits to the performance of bulk Nb. In particular, at high gradients, cavity performance can be limited by magnetic field quenching. As previously stated, the RF critical magnetic field for Nb is ∼180 mT. Since E and H are coupled in a cavity, this

places an upper limit on the accelerating gradient. It is not unusual for carefully prepared single-cell cavities to approach this limit [52,53]. There is some sense, then, that bulk Nb is slowly reaching its fundamental performance ceiling [54].

In addition to the 180 mT performance ceiling, other concerns drive research into new SRF materials. For example, Nb has poor thermal conductivity. Local heating on the interior surface can drive an entire cavity into the normal state [55]. Other materials might be more efficient than Nb at transferring heat into the surrounding liquid helium bath, and would allow for a significant improvement in cavity stability.

Finally, there are cost considerations [56]. Higher gradients would mean that fewer cavities would be necessary for a given beam energy. This in turn implies capital cost savings. In the same vein, material with $T_c > 9.2$ K would require less cooling than Nb, saving on cryogenic costs.

There are several approaches to the problems presented above. One approach is to construct cavities out of new materials with higher critical fields or temperatures [57,58]. Another is to coat a bulk Cu cavity with a thin superconducting film. Since fields (and therefore currents) are contained within a penetration depth of the metal surface, only a layer of thickness $\sim \lambda$ on the cavity interior is responsible for superconductivity itself. The underlying Cu substrate can serve as mechanical support, thermal stabilizer, and magnetic shielding [49, 56, 59]. This thin film approach was implemented at CERN for the upgrade to LEP [60]. Along these lines, a multilayer thin film coating may be used to enhance the RF critical magnetic field of a cavity [1]. This last approach will be discussed in depth in the next chapter.

Chapter 2

A Multilayer Film Approach to SRF Cavities

The basis of this dissertation is the multilayer film approach presented by Gurevich [1], in which the inner surface of an SRF cavity is coated with alternating thin superconducting and insulating films. In this context, "thin" means thinner than the London penetration depth of the superconducting films. This type of system, with films of this thickness, has electrodynamic and thermodynamic properties that are complex but potentially useful for SRF cavities. This chapter presents a review of Gurevich's paper, as well as an analysis of the physics of multilayer films and the practical issues involved in their implementation.

2.1 A. Gurevich, Applied Physics Letters 88, (2006).

As discussed in the previous chapter, niobium SRF cavities are limited by the lower critical magnetic field $H_{c1} \sim 180$ mT. Typical cavity behavior is such that cavities quench above this threshold. To first approximation, the accelerating field increases linearly with increasing magnetic field. Neglecting dissipative mechanisms like material defects, H_{c1} then represents an upper limit on the energy any SRF cavity might impart to a particle beam.

The exponential behavior seen in Equation 1.15 can be exploited to screen magnetic fields from the bulk of an SRF cavity. In Figure 2.1, a 150 nm (Nb,Ti)N film damps the cavity field by nearly 50% [1]. The insulating film in the multilayer structure serves to

[1]For simplicity, this chapter deals largely with multilayer films composed of one insulating layer and one superconducting film deposited on a niobium substrate. Generally, the insulator is - in this chapter

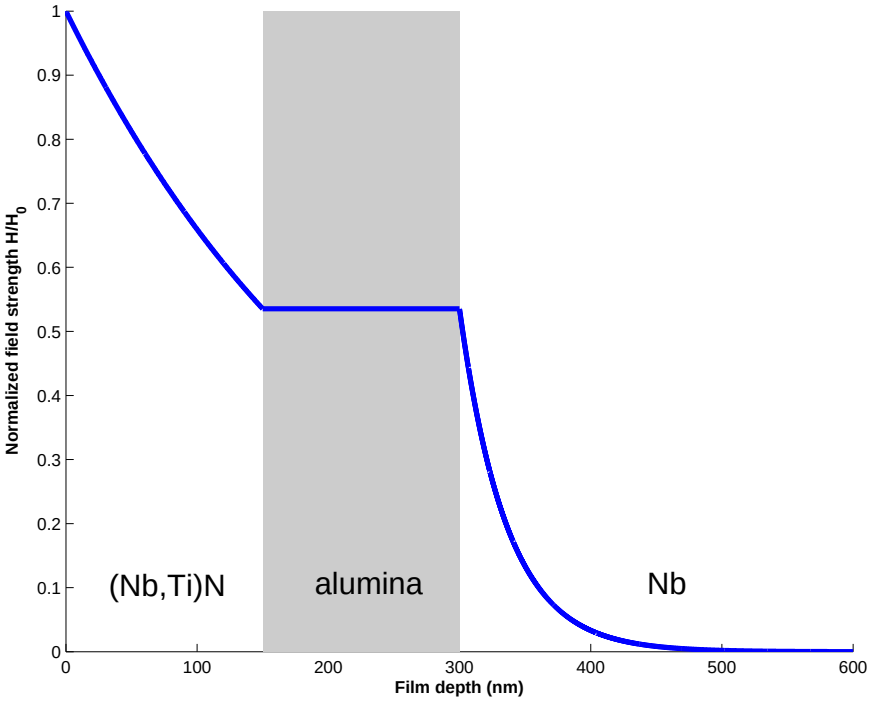

Figure 2.1: Screening of a cavity field in a multilayer resonator. The horizontal axis denotes the distance $\mathbf{H} \times \hat{\mathbf{n}}$ penetrates into the cavity wall (nm). This figure shown field screening in a hypothetical (Nb,Ti)N / Al_2O_3 multilayer film, deposited on a Nb substrate. Note that the magnetic field decays to approximately half its value within the thin film.

electrically separate the thin film from the bulk superconductor, preventing current from moving between the two materials. In this fashion, strong cavity fields $H > H_{c1}^{\text{bulk}}$ are prevented from directly quenching the superconducting bulk. It follows that the thin film layer's critical fields, specifically H_{c1}, become the limiting factor in cavity performance. This is advantageous since thin film superconductors may potentially outperform bulk Nb for SRF applications [49, 59, 61].

A consequence of this layering scheme is to increase the overall H_{c1} and Q_0 of the cavity. The increase in H_{c1}follows from energy considerations in the Meissner state of a thin film in the multilayer system. When a type-II superconductor is in the Meissner

and for the sake of argument - aluminum oxide and the superconducting film is niobium-titanium nitride. These specific materials are chosen for reasons addressed in the next chapter.

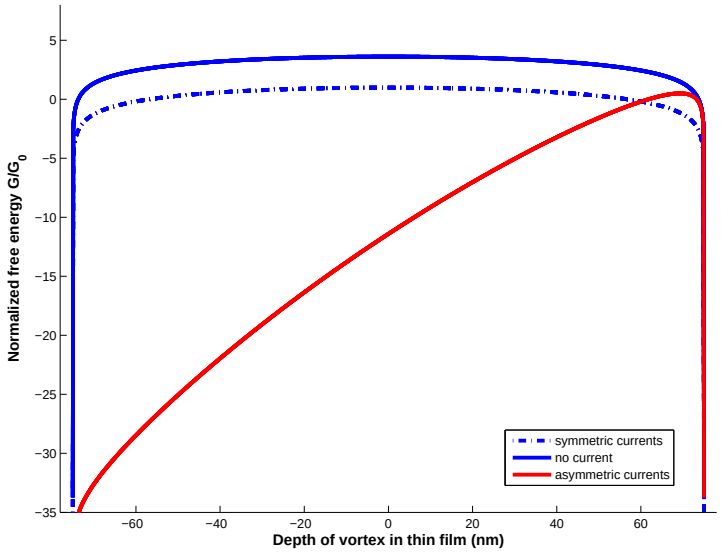

Figure 2.2: Normalized vortex free energy for three different configurations: no surface currents (solid blue line), a free-standing film in a uniform magnetic field (dashed blue line), and a multilayer film with asymmetric surface currents on front and back faces (red line). The film is Nb-Ti-N, with $\lambda \approx 240$ nm, $d = 150$ nm, $\xi_0 \approx 4$ nm [63, 64]. The red line illustrates the free energy barrier to vortex penetration.

state, magnetic flux vortices develop. In the presence of an RF field these vortices oscillate, dissipating energy in the form of heat. Multilayer films create a free energy barrier to vortex penetration in the bulk layer, minimizing this source of losses. Consider the Gibbs free energy per unit length of a single flux vortex moving in a thin film of thickness d, coherence length ξ, and penetration depth λ [1, 62]:

$$G/L = \frac{\phi_0^2}{4\pi\mu_0\lambda^2} \ln\left[\frac{d}{1.07\xi}\cos\frac{\pi u}{d}\right] - \phi_0 \int_u^{d/2} J(z)dz. \tag{2.1}$$

Here, $-d/2 < u < d/2$ is the position of the vortex and J is the current density in the film. The first term in Equation 2.1 is the kinetic energy of a moving vortex and the second term is the Lorentz force contribution from the net current across the film. The normalized free energy $G/G_0 = G/(\phi_0^2/4\pi\mu_0\lambda^2)$ is shown in Figure 2.2. Evidently, in a film with asymmetric Meissner currents it becomes energetically favorable for vortices to leave the multilayer film at the surface. Equivalently, the distribution of currents in a multilayer film creates a surface barrier for vortex penetration, raising the effective H_{c1}.

This is the basis of the multilayer film approach.

Gurevich illustrates this surface barrier via the vortex equation of motion

$$\eta\dot{u} = -\frac{\partial G}{\partial u} = \frac{\phi_0^2}{4\mu_0\lambda^2}\tan\frac{\pi u}{d} - \phi_0 J. \tag{2.2}$$

η is the drag coefficient of a moving vortex. Similar to the standard image charge problem, vortices moving near the surface of a superconductor experience a force due to induced surface currents. These can be modeled as an image vortex. Very near ($u \approx d/2 - \xi$) the surface of the superconducting film, Equation 2.2 is approximated by

$$\eta\dot{u} \approx \frac{\phi_0^2}{4\pi\mu_0\lambda^2\xi} - \frac{H}{\lambda}.$$

A negative force on the vortex $\eta\dot{u} < 0$ pushes it out of the film. The critical field for multilayer vortex penetration H_{v} then occurs at $\eta\dot{u} = 0$, or

$$H_{\mathrm{v}} \approx \frac{\phi_0}{4\pi\lambda\xi} \tag{2.3}$$

which for (Nb,Ti)N is roughly fifteen times H_{c1}.

2.2 Thermal effects

Using the thermal feedback model of Gurevich and Mints [65] it is possible to estimate the thermal behavior of the multilayer structure. This is a nontrivial consideration: if the thin films are poor thermal conductors, RF heating at the film surface will cause thermal quenching regardless of any enhanced H_{c1}. To this end, Gurevich estimates the maximum tolerable RF fields using a heat balance equation, in which the Joule heating from the cavity fields is entirely conducted through the cavity walls and into a surrounding liquid helium bath.

$$\frac{1}{2\mu_0^2}R_{\mathrm{s}}B^2 = h(T - T_{\mathrm{bath}}) \tag{2.4}$$

where h is the Kapitza thermal conductance ($\mathrm{W/m^2K}$) between the cavity wall and the bath, held at temperature $T_{\mathrm{bath}} \sim 2$ K. R_{s} is the RF surface resistance of the cavity wall

$$R_{\mathrm{s}} = \frac{A\omega^2}{T}e^{-\Delta/k_{\mathrm{B}}T} + R_0. \tag{2.5}$$

Note that when in the limit $T_{\mathrm{bath}} \to T$, any amount of Joule heating will quench the cavity. B here is the maximum tolerable RF field strength.

In Equation 2.5, A is a coefficient that weakly depends on frequency ω and temperature T. For these purposes, A may be treated as approximately constant [1,36]. The first term follows analytically from the BCS theory of superconductivity. The second term, R_0, is the residual surface resistance. This term is constant with temperature and, as of this writing, is not *a priori* calculable. R_0 must be measured. Values of A, $\Delta(T)$, and R_0 vary between superconductors and depend on film deposition or bulk processing techniques. For the calculations that follow, approximate values of R_s are estimated based on the data in References [36, 61, 63].

Two assumptions are implicitly made by using Equations 2.4 and 2.5. First, the *a priori* temperature-dependence of R_s can only be estimated, as discussed above. Second, the form of Equation 2.5 is derived from Fermi's Golden Rule for transition rates between states of a superconductor, mediated by some weak interaction between a BCS quasiparticle and an incident photon with energy $\hbar\omega$ and momentum $\hbar\mathbf{k}$. This interaction is described by a matrix element $M\left(\mathbf{p}_i, \mathbf{p}_f, \hbar\omega, \hbar\mathbf{k}\right)$, where $\mathbf{p}_{i,f}$ are the initial and final quasiparticle momenta. A straightforward calculation of R_s is only possible if the matrix element M is constant, which is only a reasonable assumption for temperatures $T \lesssim 0.5T_\mathrm{c}$ [35].

Equations 2.4 and 2.5 are therefore approximations. They are insufficient to predict the real-world thermal behavior of any specific cavity - one with material defects, impurities, etc. - but are nevertheless useful in comparing the thermal conductivity of several different cavity coatings. A rough estimate of $R_\mathrm{s}(T)$ is shown in Figure 2.3a. For a cavity with a multilayer coating of total superconductor thickness L, the overall surface resistance $\tilde{R}_\mathrm{s}$ becomes

$$\tilde{R}_\mathrm{s} = \left(1 - e^{-2L/\lambda}\right) R_\mathrm{layers} + e^{-2L/\lambda} R_\mathrm{bulk}. \tag{2.6}$$

Based on Equations 2.4 and 2.6, an appropriate choice of material for the multilayer superconductor will reduce R_s and therefore increase the maximum tolerable RF magnetic field B_b. From Equation 1.13, this also has the effect of increasing the cavity's Q-value.

From the values for R_s in Figure 2.3a, an assessment of the thermal behavior of a multilayer system can be made. Figure 2.3b is obtained using Equations 2.4 and 2.6.

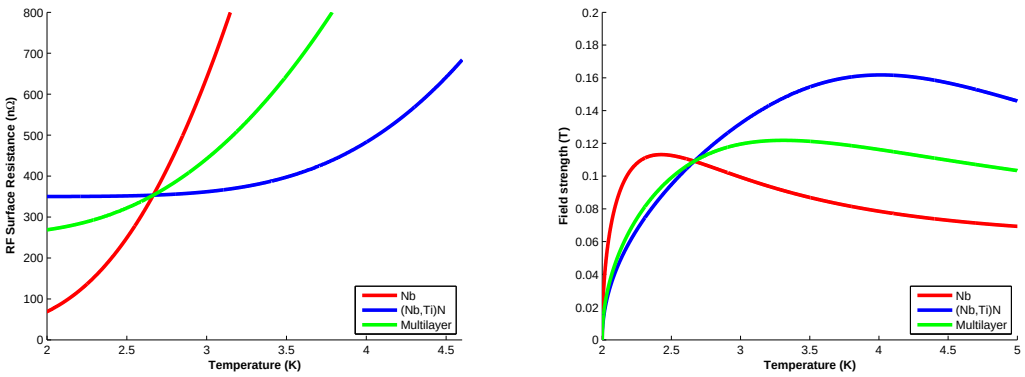

(a) Surface resistance vs. temperature.

(b) Magnetic field vs. cavity surface temperature.

Figure 2.3: R_s for various cavity types, as well as the effect of R_s on thermal conductivity. In both figures, the red line represents the behavior of a bulk Nb cavity, blue represents a hypothetical bulk (Nb,Ti)N cavity, and green shows a cavity treated with a multilayer film.

Since $\tilde{R}_s < R_{s,Nb}$ above $T \approx 2.75$ K, it is reasonable to expect that NbTiN multilayers will not add to the thermal burden of a cavity.

The net effect of the multilayer film approach is to increase both the Q_0 of a cavity and its effective H_{c1} - the field strength at which quenching occurs. The increase in H_{c1} occurs for the reasons discussed above. An increase in H_{c1} corresponds linearly with an increase in the maximum achievable accelerating gradient. All other cavity performance factors aside, doubling the effective H_{c1} is equivalent to doubling the accelerating gradient. The increase in Q_0 comes from the surface resistance of the superconducting thin film layers used in the multilayer structure, as in Equation 2.6. Using multilayer thin films with lower surface resistance means an overall reduction in Ohmic losses at the cavity walls, which in turn means increased Q_0. These increases are shown schematically in Figure 2.4.

2.3 Limits of multilayer performance

Evidently, the multilayer thin film approach may yield improvements in Q and H_{c1}. Some natural questions arise based on the above predictions: How thin is too thin? Since thick films would allow more exponential field damping, what is the incentive to make thin films? And finally, the above calculations are made for a single thin superconducting film

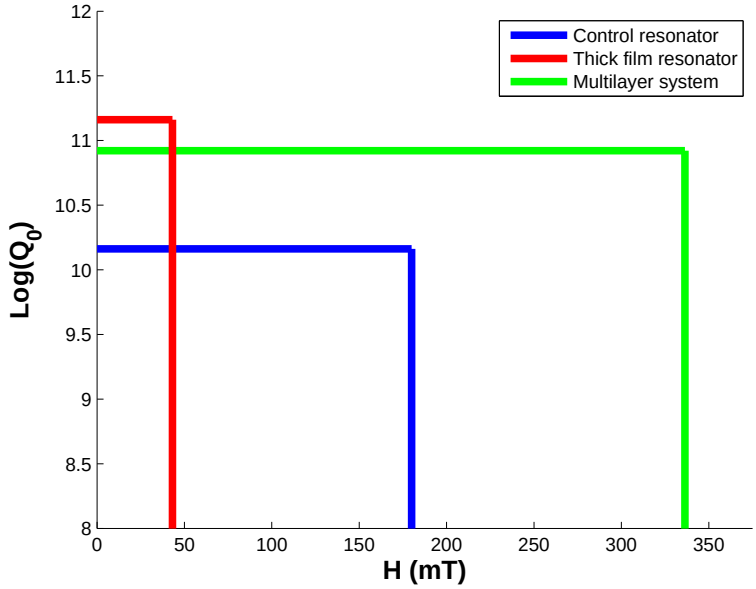

Figure 2.4: Q_0 vs. H for a standard CEBAF-type elliptical 1.5 GHz cavity. A bulk Nb cavity is shown in blue. The red curve represents an equivalent cavity made (somehow) from bulk Nb_3Sn, with concomitant lowering of R_s and H_{c1}. The green curve shows a Nb cavity treated with a multilayer coating of Nb_3Sn. This curve demonstrates the improvements in Nb cavity performance made possible by multilayer coatings.

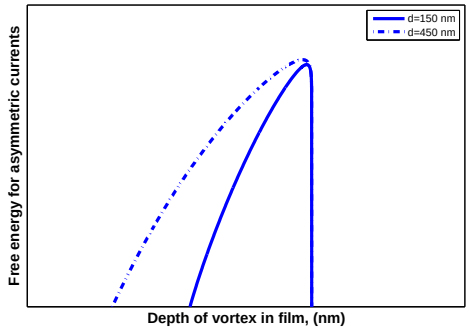

Figure 2.5: Comparison of free energy gradients in thin and thick films. Note that thin films provide a larger vortex free energy gradient. Evidently thin films suppress vortex entry more effectively than thick films.

deposited on a single dielectric film. Adding more film layers might provide additional field screening, but how would this affect thermal performance?

Regarding the limits of film thickness, there are practical limits to how thin a film might be. Film quality is highly dependent on the underlying substrate quality. A nonuniform substrate - or one whose lattice is not well matched to the film's lattice structure - may contribute significantly to the defect density of the film. Furthermore, depending on growth conditions, film uniformity may improve with thickness as internal stresses are relieved and as grains grow at different rates. (See References [66,67], e.g., for more details.) In general, it is difficult to control the uniformity of very thin films. There are also lower limits to the thickness of the dielectric film. The dielectric layer must be large enough to prevent Josephson coupling [68]. Additionally, the dielectric layer must be appreciably thicker than the mean surface roughness of the substrate on which it sits, such that there is no risk of electrical contact between superconducting layers.

Uniformity is easier to control in thicker films, and thick films allow for more field damping. However, films that are too thick actually benefit less from the multilayer approach. Specifically, thick films will ultimately have a lower H_{c1}. From Equation 2.2, the maximum tolerable magnetic field in a cavity, H_v, depends on the vortex free energy gradient across a film. This free energy gradient in a thick film is lower than that in an equivalent thin film (see Figure 2.5). There is then a tradeoff between film uniformity and vortex exclusion.

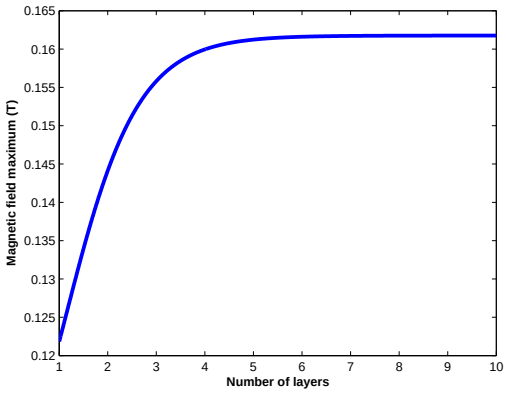

Figure 2.6: Maximum allowable field strength (via the heat balance equation) as a function of the number of thin film layers. For NbTiN with $\lambda \approx 240$ nm, no additional thermal benefit is obtained for $\gtrsim 4$ layers.

One last question arises in considering the implementation of multilayer films: If one superconductor/insulator film layer is effective at screening vortices and increasing the effective H_{c1} of the cavity, will more layers be more effective? Is there an upper limit on the number of superconductor/insulator film layers? Here, the main performance limit is the thermal conductivity of the multilayer structure. Adding more layers makes it more difficult for heat to pass from the inner cavity surface out to the surrounding liquid helium bath. The heat balance equation indicates that, for the NbTiN/Al_2O_3 films considered in this chapter, there is no benefit to using more than roughly four superconductor/insulator films. This is shown graphically in Figure 2.6.

Apart from issues of implementation, the model discussed in Reference [1] makes one very significant assumption: it treats all superconducting surfaces as perfectly smooth. The vortex image arguments of Equation 2.2 are made in one dimension for planar surfaces. For real-world films with any appreciable surface roughness, such arguments may be qualitative at best. There exists some work in the literature that accommodates surface roughness in predicting the behavior of superconductors [69, 70]. However, in this context, a full treatment of vortex dynamics at an arbitrarily rough interface is beyond the scope of this dissertation.

Finally, a disclaimer: Surface resistance, penetration depth, mean free path, and coherence length are all parameters which depend strongly on film quality and therefore on

deposition technique, substrate preparation, etc. Consequently, calculations of increased R_s and Q_0 require a detailed knowledge of the form of the BCS surface resistance, as in Equation 2.5. Figures 2.1-2.6 represent rough estimates of film behavior, using data aggregated from many previous studies.

2.4 Prior work on multilayer films

To date, there are two groups that have reported preliminary results on multilayer films. The work of these groups differs substantially from the work presented in this dissertation. Their results are summarized here.

C. Antoine *et al.*, CEA Saclay, France

In this work [71], alternating 15 nm layers of NbN (superconductor) and MgO (insulator) were deposited on 250 nm-thick Nb film substrates via magnetron sputtering. The DC magnetization response of the samples was then studied using SQUID magnetometry. The results of this work tend to suggest a difference in the magnetization of films due to the presence of a multilayer coating. However, the authors conclude that the sensitivity of moment measurements combined with sample edge effects made further work necessary.

R. Russo *et al.*, various institutions, Italy

In this work [72], alternating 80 nm layers of Nb and Al_2O_3 were deposited on 250 nm-thick Nb film substrates via DC and RF magnetron sputtering. The film response was studied using inductive third-harmonic measurements, in which a "pancake coil" applied a 1 kHz magnetic field to small, flat multilayer samples. The same coil is then used to detect third-harmonic voltage responses induced by vortex motion in the film. These measurements indicate an improvement in H_v (as defined in Section 2.1) due to multilayer coatings, as shown in Figure 2.7.

The studies described above give interesting indications of the efficacy of multilayer films in postponing the onset of flux penetration. Note, however, that these studies are conducted at DC or at very low (kHz) frequencies, complicating any potential cavity predictions vis-a-vis RF surface resistance. Furthermore, neither study makes *a priori*

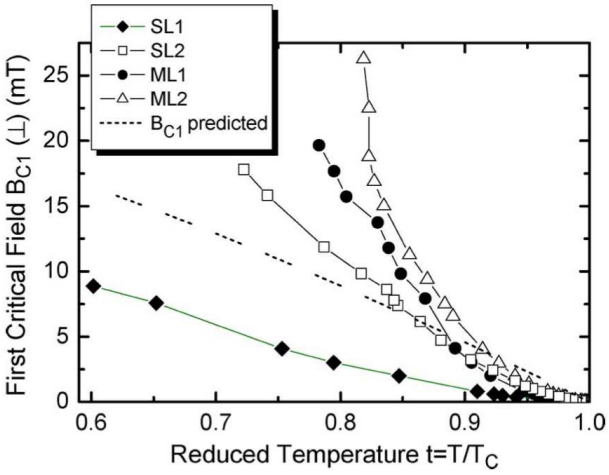

Figure 2.7: Results from Russo *et al.*, reproduced from Reference [72]. A clear improvement in H_v (termed B_{c1} in the plot) is evident.

predictions of film behavior based on Reference [1]. This makes it difficult to interpret results. The next chapter of this dissertation presents experimental design details of the current work.

Chapter 3

Experimental design

This chapter presents the design of an experimental program to evaluate multilayer films for SRF. Rather than deposit multilayer films on the interior of a 1.5 GHz elliptical cavity, small flat samples are evaluated using a microstrip disk resonator. The motivations for this choice are presented below, along with finite difference simulation results and other experimental design work. Ultimately, the goal is to measure the Q of resonators with various film configurations and compare that experimental data with the predictions of Gurevich [1]. The results should fit curves similar to those in Figure 2.4.

The entire experimental apparatus is described. This includes the supply and control of liquid helium to maintain the resonator in the superconducting state, as well as the supporting RF power and vacuum control systems.

3.1 Small samples

The multilayer thin film approach was developed specifically for use in SRF cavities. From that perspective it would seem logical to treat a series of cavities with thin film coatings and then directly evaluate Q and H_{c1}. In practice however, the parameter space of cavity development is enormous. Starting from a bulk Nb ingot, producing a single CEBAF-type Nb cavity typically involves a linear combination of the following steps [23, 36, 46, 73–76]:

- purification of bulk Nb ingot via electron-beam melting
- forging, annealing, and rolling or slicing sheets from Nb ingot
- deep drawing of sheet Nb into half cavity cells

- trimming and grinding of half-cells
- electron beam welding
- buffered chemical polishing
- electropolishing
- baking at various temperatures in ultra-high vacuum
- high peak RF power processing
- high-pressure rinsing with ultra-pure water
- component assembly in cleanrooms

These steps may vary in order and duration, depending on institutional practice and design goals. Critically, each of these fabrication steps may affect the final cavity performance in subtle ways. For example, contaminants on the cavity surface may contribute to field emission, lowering the Q-value. But once the cavity exhibits the symptoms of field emission, it is difficult to say which step in the production process introduced this problem. This is essentially a solved problem in the context of mass cavity production, during which largely-successful production algorithms are followed and cavity yields of less than 100% are acceptable. But in the context of the present work, it is necessary to understand multilayer film behavior on a fundamental level. If a resonator treated with multilayer films exhibits a Q-value that is lower than predicted, does that effect come from unpredicted vortex dissipation, indicating anomalous mulitlayer behavior? Or does the effect come from, e.g., defects introduced during the installation of contaminated power couplers in the cleanroom assembly phase? Or overly-warm acid temperatures during the electropolishing phase? Or persistent hydrocarbon contaminants from deep-drawing? These issues do not even address the additional difficulties involved in depositing films of uniform texture and thermodynamic phase over large, complex surface topologies like elliptical cavities.

This work evaluates multilayer films in the small sample regime. From a certain perspective, this may make it more difficult to draw conclusions about multilayer behavior in actual elliptical cavities. On the other hand, it eliminates the vast majority of the steps listed above, drastically simplifying the production process. This simplification, in turn,

supports the repeatability of measurements and the confidence in any conclusions drawn.

3.2 Experimental requirements

Within the small sample regime, there are several requirements for any experimental design. Some come directly from the math in Chapter 2 and some are practical considerations.

First, applied magnetic fields must be parallel to the film surface. Vortex penetration occurs at much lower field strengths when those fields are oriented perpendicular to the film surface [38]. Parallel fields not only defer the onset of vortex penetration, but they also mimic the TM_{010} accelerating mode of an elliptical cavity, as shown in Figure 1.4c.

In addition, the highest magnetic field anywhere in the resonator/sample system must be confined to the sample surface. High fields elsewhere may propagate extraneous vortices and complicate Q measurements. Equivalently, the sample itself must have lower H_{c1} than any other part of the experimental apparatus. To ensure low values of H_{c1}, films must have very high values of the Ginzburg-Landau parameter $\kappa = \lambda/\xi$, since $H_{c1} \propto \log(\kappa)/\kappa$. This has the extra benefit of simplifying the London penetration depth, as discussed briefly in Chapter 1.

Choosing a film with low H_{c1} is superficially contradictory to the idea of improving H_{c1} using multilayer coatings. However, this design criterion ensures that dissipative vortices enter the sample before they enter any other part of the experimental apparatus. The goal here is to facilitate measurements of Q.

As discussed in Chapter 2, Gurevich's model of multilayer films predicts very specific behavior. A conclusive evaluation of the Gurevich model therefore does *not* require surpassing 180 mT in treated Nb samples. Instead, theoretical predictions of multilayer behavior may be directly compared to experimental data by means of Q vs. H graphs like the one shown in Figure 2.4. This approach allows for the clarity of measurement described above, in which dissipative vortices have an obvious source and film performance is ideally unambiguous.

Finally, issues such as field emission and multipacting would greatly complicate any useful measurement of multilayer performance. Preliminary designs based on a TE_{011}

coaxial cavity (similar to the system designed by Ciovati [77]) were rejected for this reason.

The above three requirements are satisfied by a circular disk resonator operating in the TM_{01} mode.

3.3 Disk resonators

Disk resonators are widely used as microwave antennas and filters [78, 79]. As such, their behavior is well understood. The basic idea is to excite standing RF fields between a circular disk and a ground plane, separated by some dielectric medium. The fields may be solved analytically by applying magnetic wall boundary conditions to Maxwell's equations in cylindrical coordinates (ρ, θ, z). There is no significant difference between the math required here and the math already presented for pillbox cavities in Appendix A. The eigenvalue solutions are Bessel functions of order n:

$$E_z(\rho, \phi, z) = E_0 J_n(k\rho)\cos(n\phi) \tag{3.1}$$

where $k \equiv \sqrt{\omega^2 \mu_0 \epsilon}$. The main difference between this system and a pillbox cavity is that variations in z are neglected; at microwave frequencies, any integral number of half-wavelengths will be much larger than the thickness of the dielectric. Within the dielectric material, the fields are therefore approximately constant in z. The associated magnetic field is

$$H_\phi = -\frac{\imath\omega\epsilon}{k} E_0 J_n'(k\rho)\cos(n\phi) \tag{3.2}$$

where the prime denotes a derivative in ρ.

To satisfy the requirement that the magnetic field be parallel to the sample, the TM_{01} mode is chosen. Then

$$E_z(\rho) = E_0 J_0(k\rho), \tag{3.3}$$

$$H_\phi(\rho) = -\frac{\imath\omega\epsilon}{k} E_0 J_1(k\rho). \tag{3.4}$$

There is no $\hat{\rho}$-component to the magnetic field in the TM_{01} mode. Imposing magnetic wall boundary conditions constrains the radius of the disk a:

$$J_1(ka) = 0 \qquad \Rightarrow \qquad ka = 3.832$$

where 3.832 is the first zero of $J_1(k\rho)$. This sets the frequency f of the resonator:

$$f = \frac{3.832c}{2\pi\sqrt{\epsilon_r}a} \tag{3.5}$$

where c is the speed of light in vacuum and $\epsilon_r = 9.4$ is the dielectric constant of the insulating layer. A small sample size would help ensure film uniformity during deposition, so a choice of $a = 2$ cm yields a frequency of 3.0 GHz. Given the availability of S-band RF equipment at Jefferson Lab, this is an appropriate choice.

The magnetic wall boundary condition is an approximation that assumes there are no fringe magnetic fields at the disk edge, and that all fields are contained within the dielectric layer. Wolff and Knoppik [80] have determined an effective disk radius a_{eff} that accounts for fringe effects, and an effective dielectric constant ϵ_{eff}, since some of these fringe fields are in air rather than in the dielectric layer[1]. Given the corrections $a \to a_{\text{eff}} = 2.27$ cm and $\epsilon_r \to \epsilon_{\text{eff}} = 9.0$, the expected frequency of the disk resonator is, from Equation 3.5, 2.7 GHz.

Say that, for a given stored energy U in the disk fields, the total Q of the system can be written as

$$Q = \frac{\omega U}{\sum_i P_i} \tag{3.6}$$

where P_i are all the possible sources of power loss. Neglecting, for the moment, loss sources external to the disk, there are three terms in the above sum: conductor losses P_c, dielectric losses P_d, and radiative losses P_r. Q can be written in a convenient form that illustrates the contribution of each loss source:

$$\frac{1}{Q_0} = \frac{P_c + P_d + P_r}{\omega U} = \frac{1}{Q_c} + \frac{1}{Q_d} + \frac{1}{Q_r}. \tag{3.7}$$

Given the magnetic field of the TM_{01} mode $H = H_0 J_1(k\rho)$, the stored energy U in the resonator is

$$U = \pi\mu_0 h a^2 H_0^2 \left|J_2(ka)\right|^2$$

for dielectric thickness h and disk radius a. The cutoff wavenumber k is determined from the magnetic wall boundary condition introduced above: $k = 3.832/a$. The power

[1] During cryogenic measurements, these fringe fields are partially contained in liquid helium rather than air. The dielectric constant of liquid helium at 4.2 K is 1.05, lowering the value of ϵ_{eff} by about 3% [81].

dissipated in the conductor walls is calculated in a similar way from Equation 1.9:

$$P_{\mathrm{c}} = \pi a^2 R_{\mathrm{s}} H_0^2 \left|J_2(ka)\right|^2 . \tag{3.8}$$

Then accounting for the small fraction of the fields stored within the London penetration depth of the disk resonator and ground plane,

$$Q_{\mathrm{c}} = \frac{\omega\mu_0}{R_{\mathrm{s}}}\left(h+\lambda\right) = 8.5\times 10^4.$$

The contribution to Q from dielectric losses depends only on the loss tangent, $\tan\delta$, which for Al_2O_3 at 4.2 K and 3 GHz is on the order of 10^{-5} [82]. Then

$$Q_{\mathrm{d}} \approx 10^5.$$

Finally, the contribution to Q from radiation losses depends on U and on the radiated power P_{r}, which is treated by a number of authors [78, 83, 84]. Following the approach of Derneryd [78], the radiation source is approximated by a ring of magnetic current at $\rho = a$, between the disk and the ground plane. The radiated power is, ultimately,

$$P_{\mathrm{r}} = \frac{\pi a^2\omega^2}{4\eta_0 c^2}\left|V_0\right|^2 \int_{\theta=0}^{\pi} \left|J_1\left(ka\sin\theta\right)\right|^2 \sin\theta d\theta \tag{3.9}$$

where V_0 is the voltage between the disk and the ground plane. For thin dielectric layers (thickness h), this voltage is assumed to be constant: $V_0 = E_0 h$. The integral in θ must be evaluated numerically. From P_r, $Q_{\mathrm{r}} = 2780$ is the radiative contribution to Q_0. Then finally, using Equation 3.7,

$$Q_0 = 2700. \tag{3.10}$$

Surface waves are another potential source of loss in the disk resonator. Together, the dielectric layer and the conducting ground plane act as a waveguide for radiative modes that do not contribute to the far field [85,86]. This leads to a lowering of the Q which can be calculated from finite difference field simulations. This is discussed more in Section 3.6.2.

3.4 Finite difference electromagnetic field simulations

Disk resonator behavior can be modeled using any number of industry-standard simulation codes. The code used most frequently during this work was Microwave Studio, published

by Computer Simulation Technologies (CST) AG[2] in Darmstadt, Germany. CST Microwave Studio is a finite difference code, in which Maxwell's equations are discretized and solved on a variable 3D mesh with user-specified boundary conditions [87, 88].

Less generally, electromagnetic fields are defined as vectors on a discrete grid. Topological constraints - imposed by Maxwell's equations - are expressed as matrix operators that act on these field vectors. As an example, consider Faraday's law of induction as treated by Weiland [88]. In integral form, for a surface of integration $\mathbf{s}$ and a corresponding area element $\mathbf{A}$,

$$\oint \mathbf{E} \cdot d\mathbf{s} = -\iint \frac{\partial \mathbf{B}}{\partial t} \cdot d\mathbf{A}. \tag{3.11}$$

A solution is sought in some finite volume that may be described by a 3D, orthogonal grid, the vertices of which are described by coordinates (u_i, v_j, w_k), where (u, v, w) are coordinate axes and (i, j, k) are indices denoting position along their respective axes. Equation 3.11 must hold for each distinct grid element, so for a single grid element in the $u - v$ plane the left-hand side may be written generally as

$$\begin{aligned}\oint \mathbf{E} \cdot d\mathbf{s} = (u_{i+1} - u_i)E_{u,i} + (v_{j+1} - v_j)E_{v,j} - (u_{i+1} - u_i)E_{u,i+1} \\ - (v_{j+i} - v_j)E_{v,j+1} + \mathcal{O}(u^2, v^2)\end{aligned}$$

In this rough notation[3], $E_{u,i}$ denotes the i^{th} vertex along $\hat{\mathbf{u}} \cdot \mathbf{E}$. The right-hand side of Equation 3.11 may be written in a similar way. The vectors containing field information are denoted $\mathbf{e}$ and $\dot{\mathbf{b}}$.

Next, to account for variations in coordinate systems and mesh topology, some matrix operators are introduced. $\mathbb{C}$ contains sign information to obtain the correct sense for path integration, and $\mathbb{D}_s$ and $\mathbb{D}_A$ contain topological information about the mesh structure along the path integral and the grid element area, respectively. Then Equation 3.11 may be rewritten

$$\mathbb{C}\mathbb{D}_s\mathbf{e} = -\mathbb{D}_A\dot{\mathbf{b}}. \tag{3.12}$$

Similar operations may be carried out to write all four of Maxwell's equations in matrix form on a specific grid geometry. Further matrices contain permittivity and permeabil-

[2] http://www.cst.com/

[3] For efficient computation, the three dimensions of $\mathbf{E}$ may be stored in a one-dimensional vector, in which case the indexing conventions are slightly different.

ity information on the grid. After some linear algebra, the Helmholtz wave equation is obtained:

$$\left[\tilde{\mathbb{D}}\tilde{\mathbb{C}}\mathbb{D}\right]\left[\tilde{\mathbb{D}}\tilde{\mathbb{C}}\mathbb{D}\right]^{\mathrm{T}}\mathbf{e} = \omega^2\mathbf{e} \qquad \Leftrightarrow \qquad \nabla^2\mathbf{E} = \omega^2\mathbf{E}. \tag{3.13}$$

The exact structure of the matrix $\tilde{\mathbb{D}}\tilde{\mathbb{C}}\mathbb{D}$ is specified in Reference [87], but is irrelevant to this discussion. The important point is that the Helmholtz equation may be written as a matrix problem with eigenvectors $\mathbf{e}$ and eigenvalues ω - fields and frequencies that may be solved computationally. In fact, since the matrices tend to be sparse, such computations on modern machines are not very intensive [88]. Eigenmode solutions in simple (i.e. pillbox) geometries may be solved on a modern desktop PC in a few minutes.

Figure 3.1a shows a finite difference simulation of the transverse magnetic field strength under a disk resonator. The scattering parameters for this structure are shown in Figure 3.2a, from which $f_{01} = 2.7455$ GHz. The difference between this value and the calculated frequency (2.7 GHz) is accounted for by the presence of the variable couplers. The mesh density during simulation also contributes to variations in f_{01}. That is, the size of a mesh cell determines the field shape, which in turn determines how the boundary conditions are satisfied. Figure 3.2b shows a plot of f_{01} for the same structure at varying mesh densities.

3.5 Complete experimental design

The object of this dissertation is to establish a program for the verification of the Gurevich model [1]. This is accomplished by applying fields to multilayer films using a microstrip disk resonator operating in the TM_{01} mode. The Q of the resonator varies inversely with dissipated power in the resonator. Therefore, a sharp drop in Q past some critical magnetic field H_{v} indicates the onset of flux penetration. Q measurements of this type are straightforward, easily conducted at TJNAF, and have been done in the past by other groups [47].

The end goal of the program is a reproduction of the Q vs. H graph in Figure 2.4. This is accomplished by making three separate resonators.

1. **Control resonator.** The control resonator is a straightforward instance of a microstrip disk resonator, with a Nb ground plane, aluminum oxide dielectric layer,

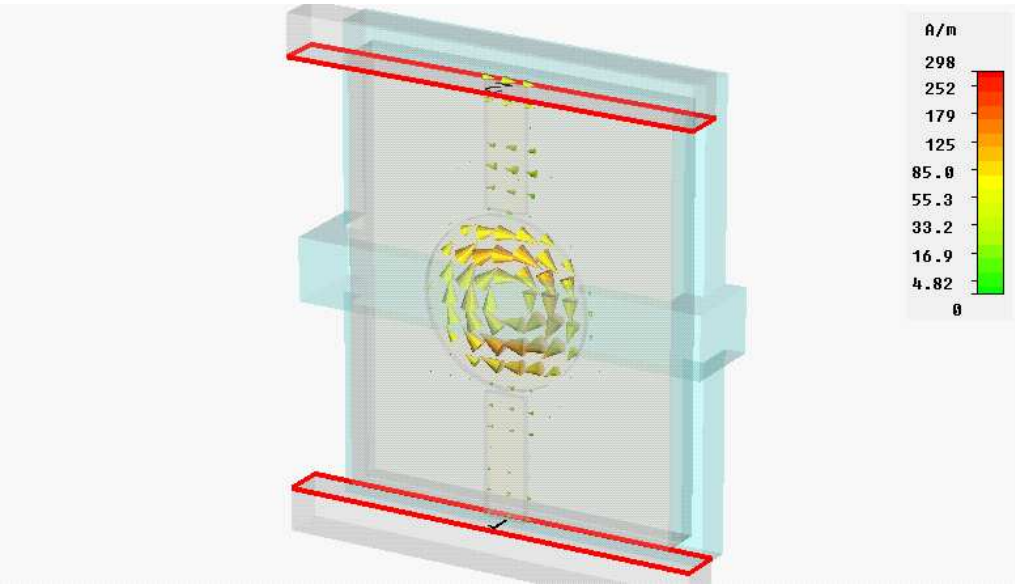

(a) Simulation with magnetic field lines.

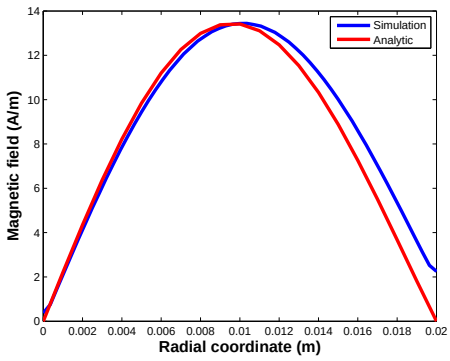

(b) H vs. ρ (radial coordinate).

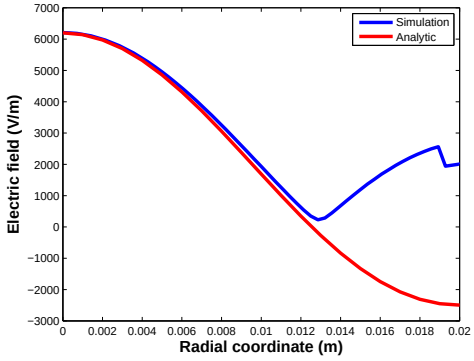

(c) E vs. ρ. Note edge effects.

Figure 3.1: CST Microwave Studio frequency domain simulation of the transverse magnetic field. Arrow size indicates field strength. The disk resonator is capacitively coupled to microstrip transmission lines. The red rectangles in Figure 3.1a indicate "waveports" - regions in the simulation through which RF power is introduced. Comparison is made in Figures 3.1b and 3.1c between simulation results and analytic calculations. Edge effects are clearly evident.

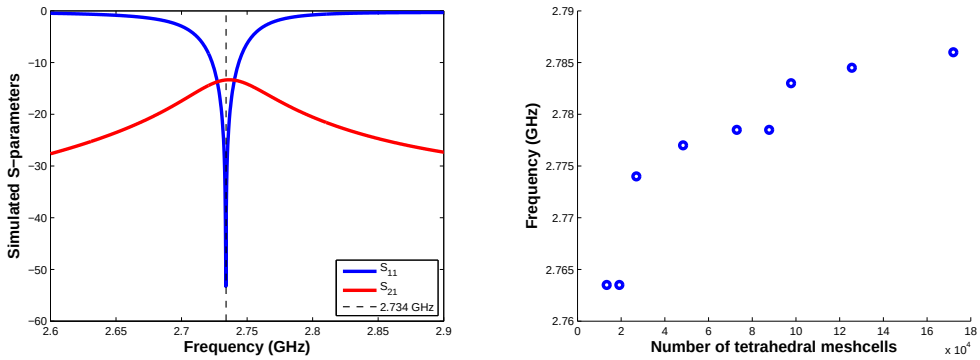

(a) S_{11} and S_{21}, simulated.

(b) Variation of f_{01} with mesh density.

Figure 3.2: S-parameters for the disk resonator, simulated using CST Microwave Studio. The resonant frequency of the TM_{01} mode varies with tetrahedral mesh density.

and a Nb disk. See Figure 3.3. As the name suggests, measurements with this resonator establish a baseline for Q, H_v, and the surface resistance.

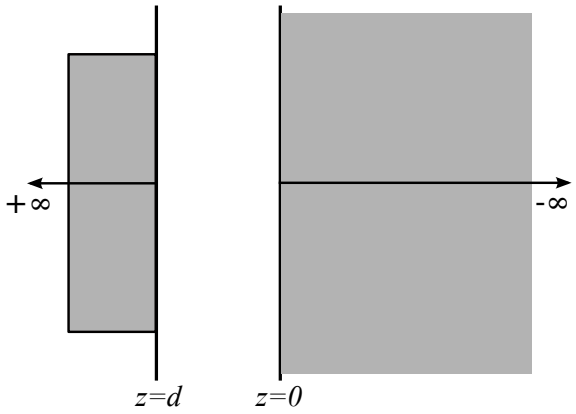

Figure 3.3: Cross section of the **control resonator**. The gray regions represent Nb (disk at $z > d$ and ground plane at $z < 0$) and the white region represents Al_2O_3. The thickness d here is unimportant. As long as $d < c/2f$, there will be no z-variation in the fields. The limits of $z \to \pm\infty$ merely represent the fact that the Nb layers here are much, much thicker than the penetration depth $\lambda_L = 36$ nm.

2. **Thick film resonator.** The multilayer films will use (Nb,Ti)N in the superconducting film layers. The thick film resonator evaluates H_v for (Nb,Ti)N by itself. Again, the purpose of this configuration is to establish a baseline for multilayer performance. This is accomplished by depositing a thick film of (Nb,Ti)N on a sapphire substrate. "Thick" here means substantially thicker than the penetration depth of

(Nb,Ti)N, on the order of a micron. At that thickness, the magnetic field decays almost to zero within the film. It is practically equivalent to a bulk (Nb,Ti)N ground plane. On top of the ground plane, a thin aluminum oxide film is deposited, and a Nb disk resonator tops the structure. See Figure 3.4. Note that for (Nb,Ti)N, H_{c1} is approximately 40 mT, roughly 20% of the value for bulk Nb. This satisfies the experimental requirements discussed in Section 3.2 that vortices enter the film at a lower magnetic field than anywhere else in the test apparatus. This, in turn, makes it significantly easier to associate a degradation of Q with flux penetration in the (Nb,Ti)N as opposed to the Nb disk or other parts of the test apparatus.

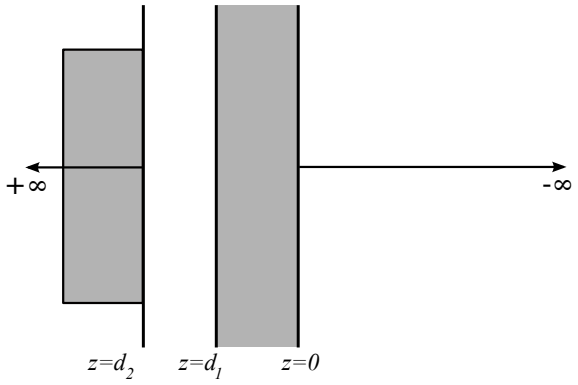

Figure 3.4: Cross section of the **thick film resonator**. The gray region at $z > d_2$ represents the Nb disk, the gray region at $d_1 > z > 0$ represents the thick (Nb,Ti)N film, and the white regions represent Al_2O_3. The (Nb,Ti)N film is termed "thick" since $d_1 \gg \lambda_L$.

3. **Multilayer resonator.** The behavior of the multilayer resonator should follow the physics outlined in Chapter 2. It consists of a bulk Nb ground plane on which is deposited a thin Al_2O_3 layer, a thin (Nb,Ti)N layer, and another Al_2O_3 layer. A Nb disk resonator is fixed atop this structure. See Figure 3.5.

In all three cases, Q_0 should be dominated by conductor losses. That is, the RF surface resistance leads to more dissipation than, say, dielectric losses. In principle, following the analysis of Derneryd, there should be no radiation losses [78]. In practice, the radiation loss from an actual disk resonator is "practically impossible" to calculate from first principles [89]. Radiative losses will be measured.

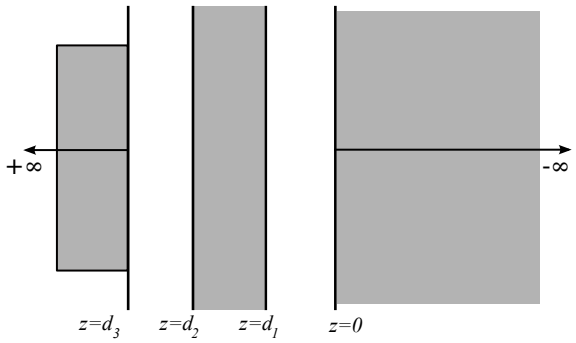

Figure 3.5: Cross section of the **multilayer resonator**. The rightmost and leftmost gray regions represent Nb, the center gray region is a (Nb,Ti)N film, and the white regions represent Al_2O_3. If the penetration depth of (Nb,Ti)N is approximately 250 nm, the thickness $d_2 - d_1$ must be less than that: 150 nm for the sake of argument.

The above resonator schemes will generate the Q-vs-H plot shown in Figure 3.6a. Beside it is a reproduction of Figure 2.4 from Chapter 2, for comparison. Several comments are warranted. First, the differences between the two graphs are explained by (a) the relatively high R_s and low H_{c1} of (Nb,Ti)N compared with Nb, and (b) the low stored energy and significant variations in the geometry factor between disk resonator configurations. These differences ensure that the above configurations satisfy the experimental requirements outlined in Section 3.2. The multilayer film described in Figure 3.5 still allows a higher value of H_v than does the control resonator. Furthermore, in developing the predictions shown in Figure 3.6a, data on R_s, H_{c1}, and other properties of (Nb,Ti)N films were extracted from References [57, 61, 63, 64, 90–92]. The values obtained from this literature survey were used for planning and design of the figures shown above. The deposition and evaluation of (Nb,Ti)N films are discussed in the next chapter.

The choice of niobium-titanium nitride warrants some attention here. Most notably, (Nb,Ti)N films have a higher surface resistance than films of, e.g., NbN or Nb_3Sn. This makes the multilayer effects less dramatic. Particularly, the Q-values of multilayer (Nb,Ti)N resonators will be lower than those of equivalent Nb_3Sn resonators. However, dramatically high Q-values are a side effect of multilayer implementation. Such values are not required in order to observe an increase in H_v, the field strength at which vortices penetrate the layers. Primarily then, (Nb,Ti)N was chosen for its relatively low value of H_{c1}, the importance of which has been discussed above. In addition, films with reliable

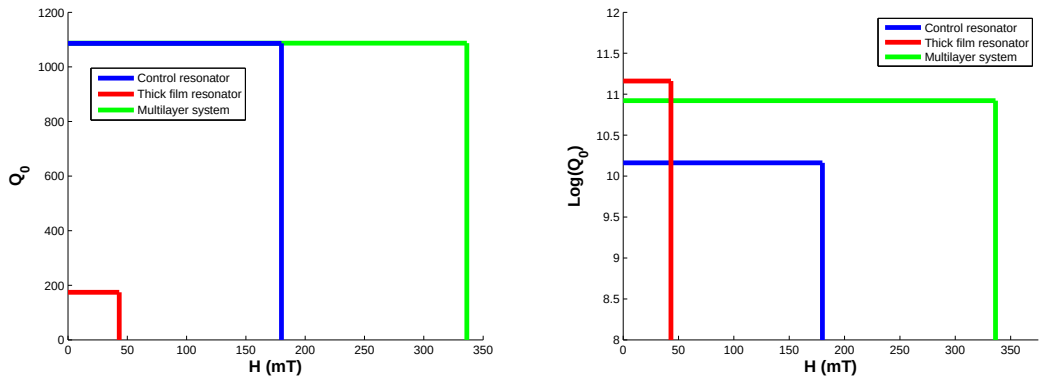

(a) Q vs. H plots for the three disk resonator configurations.

(b) Same layering scheme for bulk Nb elliptical cavity.

Figure 3.6: Predicted Q vs. H curves for the three disk resonator layering schemes, as well as Figure 2.4, reproduced here for the sake of comparison. The differences stem from the relatively low value of H_{c1} in (Nb,Ti)N, along with its relatively high surface resistance. The disk resonator also has a very small stored energy U, further lowering Q. The calculation of Q is discussed in Sections 3.3 and 3.6.2.

values of T_c are easily made. (T_c is a useful parameter for film characterization since in an approximate sense, $T_c \propto \Delta$ and the gap energy Δ conveys significant information about critical fields, surface impedance, etc.) Finally, the means of creating (Nb,Ti)N films are readily available at TJNAF. All these points will be discussed more in Chapter 4.

Finally, it bears repeating that this dissertation does not describe an attempt to surpass 180 mT in bulk Nb. Rather, it attempts to verify the predictions made by Gurevich regarding multilayer film performance. (This justifies the differences between Figures 3.6a and 3.6b.)

3.6 Apparatus

The disk resonator shown in Figure 3.1a is, by itself, not experiment-ready. It requires the support of a broad experimental infrastructure. Liquid helium is required to cool the superconductors past their critical temperatures, which in turn requires that measurements and adjustments be done under vacuum. This section describes the supplementary hardware required to make measurements on a superconducting microstrip disk resonator.

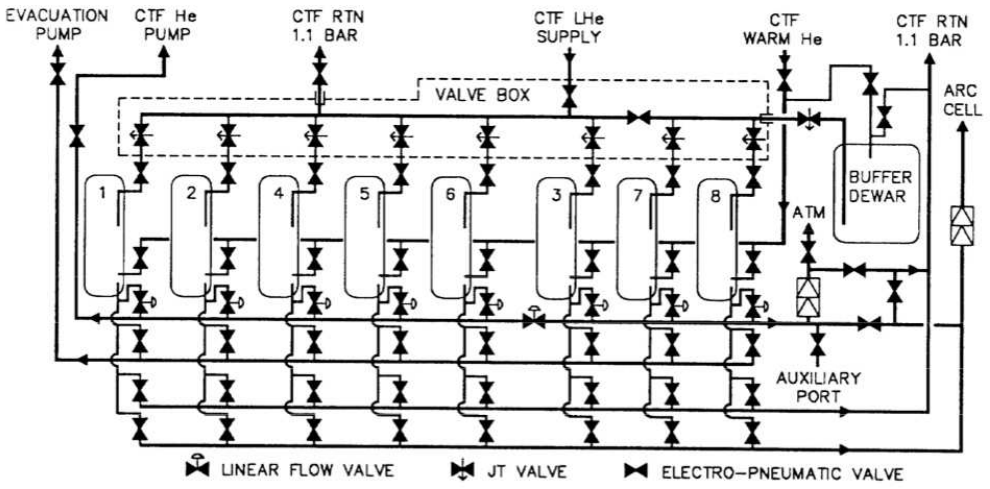

Figure 3.7: VTA block diagram, reproduced from [93].

3.6.1 The Vertical Test Area and its RF control systems

At TJNAF, cavity measurements at liquid helium temperatures are typically made in the vertical test area (VTA). The VTA consists of eight vertical liquid helium (LHe) dewars, connected by a network of valves and transfer lines to the liquid helium plant at the nearby cryogenic test facility (CTF). A system of mechanical and electrical interlocks regulates the flow of liquid helium from the CTF into each dewar individually, allowing multiple simultaneous cavity tests. The operation of the VTA is described in Reference [93]. The dewars vary in size between "small" (136 liters usable volume, 183 cm deep) and "large" (1197 liters, 336 cm deep). The majority are shielded to protect users from radiation and/or strong magnetic fields during high-power RF testing. A schematic is shown in Figure 3.7.

The insertion of a cavity into the dewar requires some specialized equipment. Cavities are hung on dewar inserts that are lowered via bridge crane into the dewars. Dewar inserts provide thermal insulation during measurements, house electrical and mechanical feedthroughs for instrumentation, provide mechanical support for cavities, and are generally mounted with a top plate that seals the dewar for operation under vacuum. Dewar insert drawings are shown in Figures 3.8-3.16.

Once the dewar insert is in place, a seal is made at the dewar/insert interface using

two concentric rubber O-rings and vacuum grease. The dewar is then evacuated to a few hundredths of a millibar and a rate-of-rise leak check is performed. If the vacuum seal is sufficiently robust, liquid helium is checked for contaminants and then introduced to the dewar. Temperature in the dewar is controlled via LHe flow rate and by heaters that can deposit up to 140 W into the helium bath. All these procedures are interlocked and monitored by various mechanical and electrical systems, which systems are designed specifically for the VTA and housed in a separate control room to shield operators from any high-field effects.

When the cavity (or in this case, the disk resonator) is in place and held at the correct temperature, RF power is supplied and tests can be conducted.

3.6.2 The dewar insert

The specific dewar insert used for the present work is shown in Figure 3.8. It incorporates, from top to bottom, haul points for crane manipulation, RF and mechanical feedthroughs, thermal shielding, mechanical support, variable couplers, and the sample holder. It is used in conjunction with one of the small, 136 L dewars.

Top plate

The top plate, shown in Figure 3.9, performs several functions. First, it serves as a flange that seals the dewar. It also houses dumbbells that serve as feedthroughs for electrical and mechanical instrumentation. Finally, along the perimeter are three evenly-spaced, rectangular haul points. The insert weighs approximately 35 kg and so must be lowered into the dewar using a crane. These haul points are where the crane attaches to the insert.

RF power delivery

RF power is coupled into the dewar through the two feedthroughs shown in Figure 3.10. These feedthroughs are SMA-type couplers welded into two mini conflat flanges. Below the flange is a length of 141-R semirigid coaxial 50 Ω line that conveys power down to the bottom of the insert, where the disk resonator is mounted.

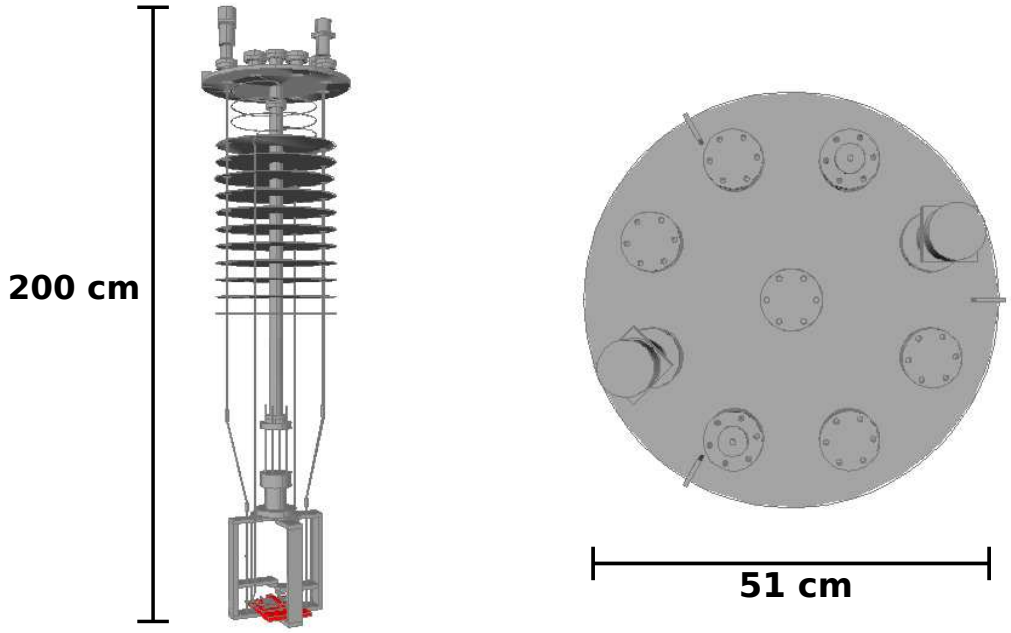

(a) Side view, with sample holder. (b) Top view.

Figure 3.8: Dewar insert.

Thermal shielding

Parallel plates are introduced between the disk resonator and the top plate to mitigate heat transfer via radiation. The Stefan-Boltzmann law is modified to describe power flow $\dot{Q}$ between two surfaces at temperatures T_1 and T_2 in arbitrary geometries:

$$\dot{Q} = F_{\mathrm{e}} F_{12} \sigma A_1 \left(T_2^4 - T_1^4\right).$$

A_1 is the area of the first surface, and F_{e} and F_{12} are factors accounting for emissivity and the relative orientation of the first and second surfaces, respectively. Inserting N layers of shielding between the top and bottom surfaces modifies F_{e}. From Barron [94],

$$\frac{1}{F_{\mathrm{e}}} = \frac{1}{e_1} + \frac{1}{e_2} + \frac{2}{e_{\mathrm{s}}} - 2 + (N-1)\left(\frac{2}{e_{\mathrm{s}}} - 1\right)$$

where e_1, e_2, and e_{s} are the emissivities of the top, bottom, and shielding layers, respectively. Eleven thin disks provide thermal radiation shielding between the top and bottom of the dewar. These are shown in Figure 3.11a. (The central axis in that figure is mechanical support for the shielding and other instrumentation.) F_{e} is shown in Figure 3.11b as a function of N.

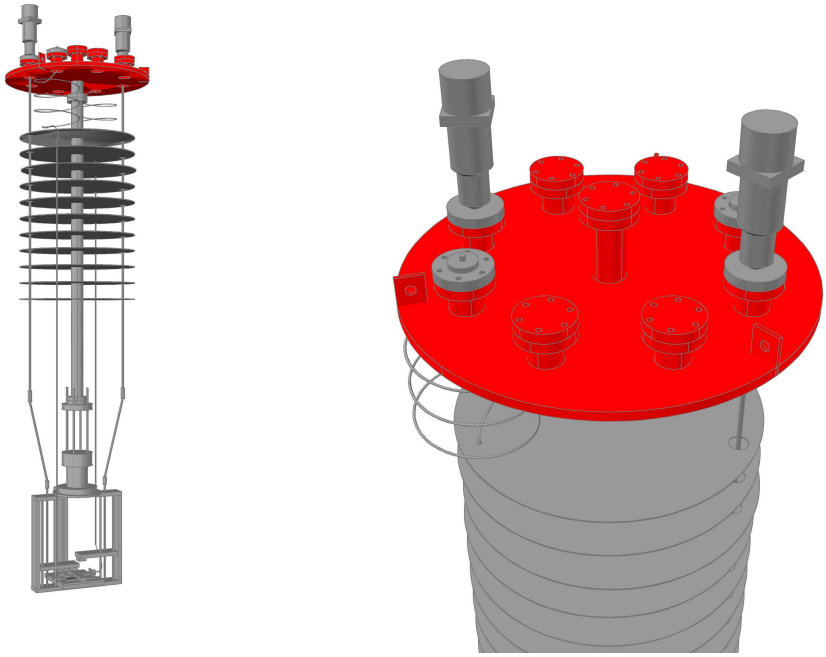

(a) Top plate on dewar insert. (b) Top plate closeup.

Figure 3.9: Top plate of dewar insert, shown in red. The top plate houses feedthroughs for all the RF lines and instrumentation.

Heat may also be transferred via convection at vacuum pressure. In principle, heat transfer by convection has the same N-dependence as that by radiation. However, at typical VTA pressures this mechanism is much less dominant that radiation and its quantitative description is omitted here.

Variable couplers

The disk is capacitively coupled to the input/output microstrip line. The gap between microstrip and disk can be modeled as a capacitive π-network, as in [80]. The overall gap reactance can be controlled simply by moving a metal plate closer to or farther from the gap. This is the function of the horizontal arms held directly above the sample in Figure 3.12.

These couplers run up and down on ball screws, which in turn are connected via universal joints to axles that terminate at the top plate. There, they are attached to rotary feedthroughs and Superior Electric M061-CS02 unipolar step motors, shown in Figure 3.13. The position of the step motors is controlled via an Arcus Performax motor

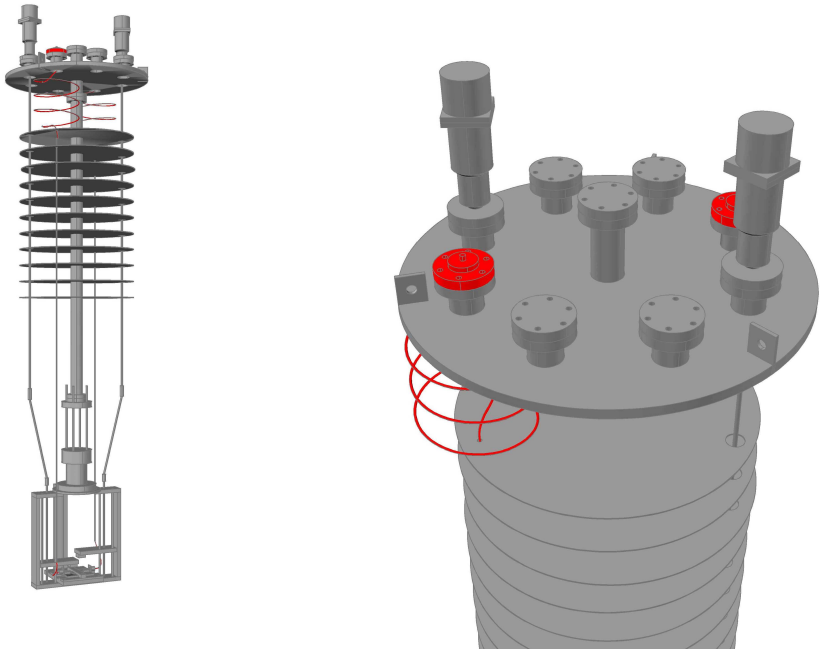

(a) RF feedthroughs. (b) Feedthrough closeup.

Figure 3.10: RF feedthrough lines, shown in red. SMA-type couplers at the top plate are attached to 141-R transmission lines that, in turn, feed power to the disk resonator.

control unit and accompanying Labview software.

In adjusting the coupling to the disk resonator, the objective is a clear measurement of Q_0. Recall that $\sum P_i$ from Equation 3.6 encompasses all the possible sources of power loss in the system. Some of these P_i, such as RF losses from superconducting surface resistance, are inherent properties of the resonator material. Other dissipative mechanisms, such as lossy transmission lines or imperfect couplers, do not yield any information about the disk resonator itself and should be neglected. These terms are incorporated into a new, "loaded" Q_L. Then Equation 3.6 may be rewritten in a more suggestive form:

$$\frac{1}{Q_\mathrm{L}} = \frac{\sum_i P_i}{\omega U} \tag{3.14}$$

$$= \frac{1}{Q_0} + \frac{1}{Q_\mathrm{in}} + \frac{1}{Q_\mathrm{out}} + \cdots \tag{3.15}$$

$$\equiv \frac{1}{Q_0}\left(1 + \beta_\mathrm{in} + \beta_\mathrm{out} + \cdots\right) \tag{3.16}$$

$$\tag{3.17}$$

where Q_in and Q_out represent power leaking out the resonator's input and output couplers.

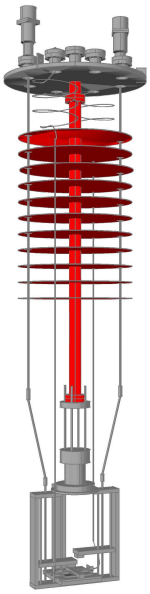

(a) Dewar insert shielding.

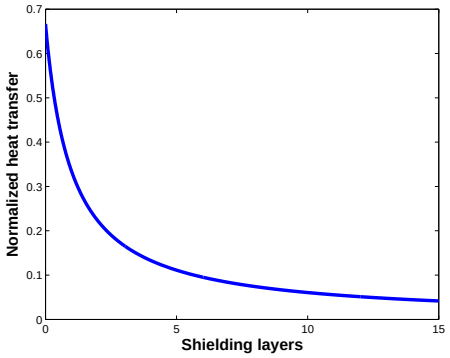

(b) Normalized $\dot{Q}$ vs. N.

Figure 3.11: Thermal shielding plates, shown in red, reduce the radiative power transfer between the room temperature environment above the top plate and the liquid helium bath at the bottom of the dewar.

(The ellipsis indicates other sources of loss.) The β_i are coupling constants, used to characterize the relative strength of the different loss mechanisms in a particular structure.

Assume that the possible loss sources now include power leakage from the input and output couplers: P_{in} and P_{out}, respectively. P_{out} can be minimized by adjusting the coupling platforms so that $\beta_{\text{out}} \ll 1$. That is, the output coupling strength is reduced as far as is practical. The input coupler is adjusted to achieve "critical coupling", where $\beta_{\text{in}} = 1$. Then Equation 3.14 gives

$$\frac{1}{Q_{\text{L}}} = \frac{2}{Q_0} \tag{3.18}$$

and so Q_0 can easily be inferred from direct measurements. Critical coupling is easily observed on a polar plot of S_{11}.

The action of the variable couplers was simulated using Microwave Studio. The height d of the variable couplers above the disk/microstrip gap was varied to produce coupling coefficients in the range $1 > \beta_{in} \geq 0$, with $\beta_{\text{out}} \ll 1$. Figure 3.14 shows a polar plot of S_{11} (magnitude and phase) for different values of d.

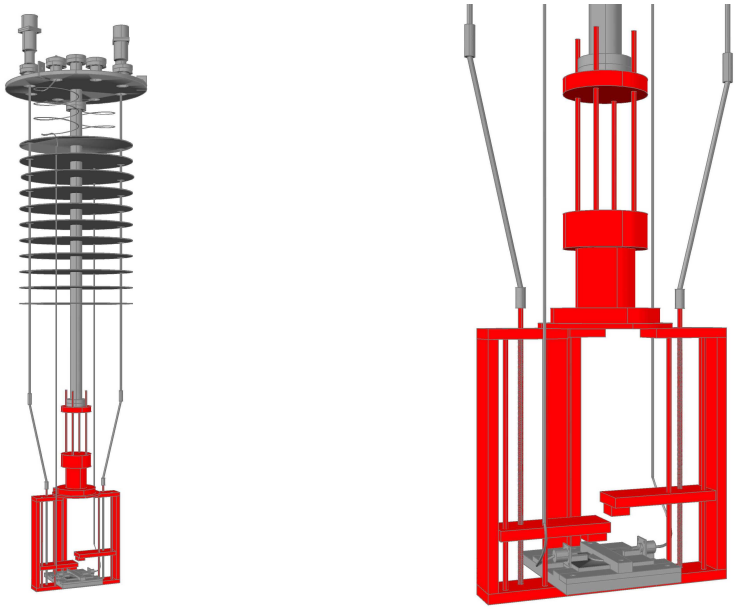

(a) Variable couplers and support.

(b) Coupler closeup.

Figure 3.12: Variable couplers allow for adjustment of RF coupling during low-temperature testing. The surrounding structure serves as mechanical support.

Once the system is critically coupled, surface wave losses can be estimated. The total normalized loss is $1-|S_{11}|^2-|S_{21}|^2 = 0.95$. Microwave Studio separates this into "surface" and "volume" losses [88]; surface losses depend on the RF surface resistance R_s, while volume losses P_V stem from the loss tangent $\tan\delta$ in the various dielectric materials of the resonator system and are calculated according to Equation 3.19:

$$P_\mathrm{V} = \pi f \tan\delta \epsilon_0 \epsilon_\mathrm{r} \int |E|^2 \partial V. \tag{3.19}$$

Simulation then indicates that volume losses compose 37.1% of the total losses. Similarly, the total unloaded Q from simulation is $Q_0^{\mathrm{sim.}} = 1100$. Assuming that dielectric and surface wave losses are the only volume losses, the contribution to Q from surface waves is estimated to be $Q_\mathrm{SW} \approx 1800$.

This allows an estimation of the input power required to generate a given magnetic field strength under the disk resonator. Using Equations 3.8-3.9, as well as the above calculations, the peak magnetic field vs. input power is shown in Figure 3.15.

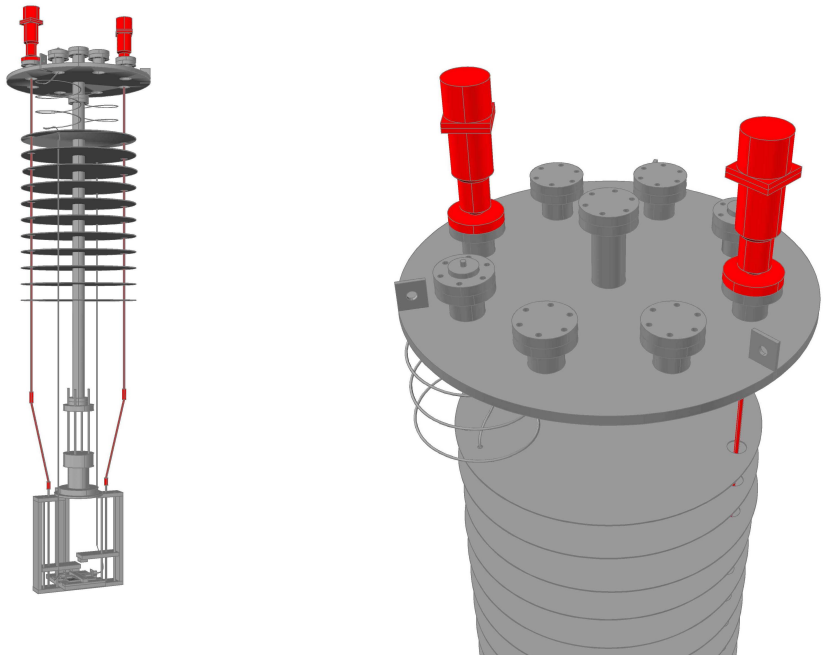

(a) Step motors. (b) Step motor closeup.

Figure 3.13: Step motors allow real-time control of the RF coupling stages during low-temperature testing.

Sample holder

Finally, the sample holder is mounted at the bottom of the dewar insert, as shown in Figure 3.16. An exploded view of the sample holder itself is shown in Figure 3.6.2. The sample holder fixes the sample in place and provides rigid termination points for the 141-R line in the form of fixed SMA-type RF connectors.

The sample also holds the resonator disk in place. The presence of peripheral hardware is a potential complication, in that extra material may modify the resonator fields or shift the resonant frequency. These effects were studied using Microwave Studio for finite difference simulations.

The sample is immersed in liquid helium. Since the resonator fields are contained entirely in dielectric regions, there is no opportunity for field emission or multipacting. Considering the apparatus as a whole, it can be seen that it satisfies all the design requirements set forth in Section 3.2.

Ideally, one sample per day can be measured. The vast majority of this time is spent in

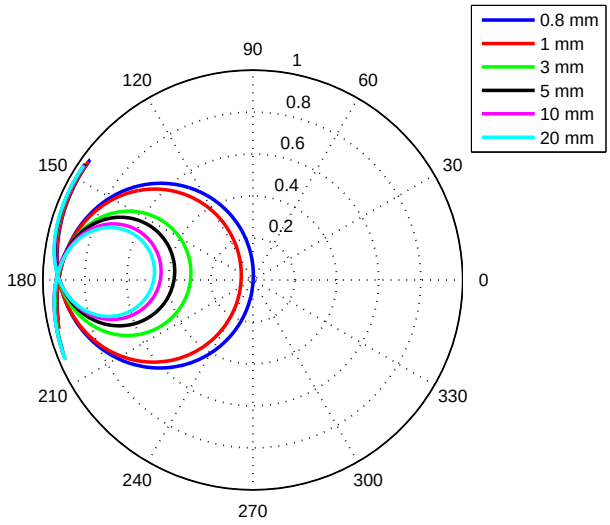

Figure 3.14: Polar plot of S_{11} for various values of coupler stage height d. The radial coordinate is $|S_{11}|$ and the angular coordinate in the phase, in degrees. Critical coupling is achieved for $d = 0.8$ mm, shown by the blue line.

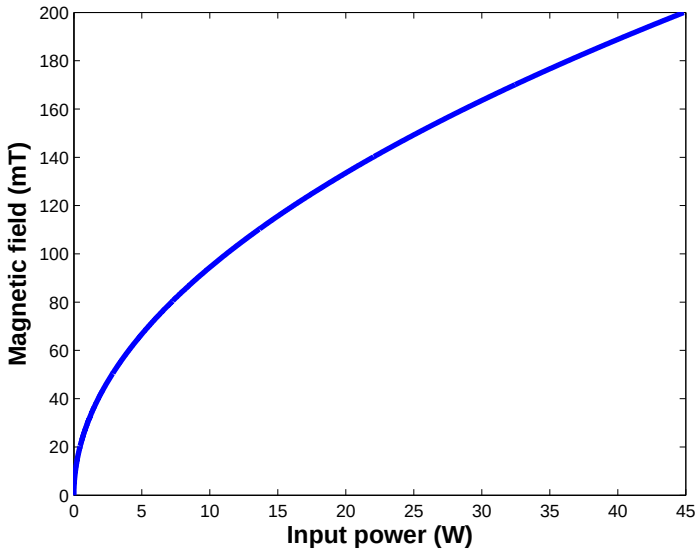

Figure 3.15: Peak magnetic field (mT) applied to the sample, as a function of input power (W).

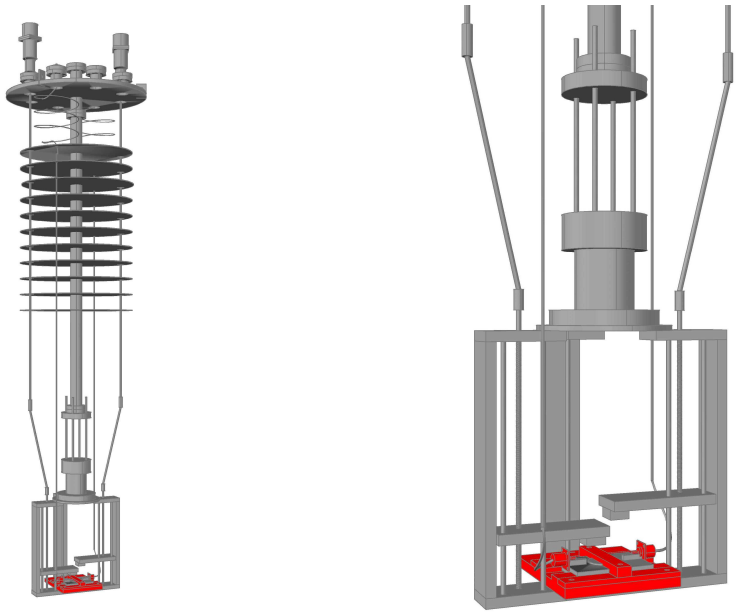

(a) Sample holder. (b) Closeup.

Figure 3.16: The sample holder fixes the disk resonator in place, permitting the variable couplers to function.

waiting for the dewar to warm after testing. Cooling to cryogenic temperatures typically requires 1-2 hours, since the “small” dewars are used.

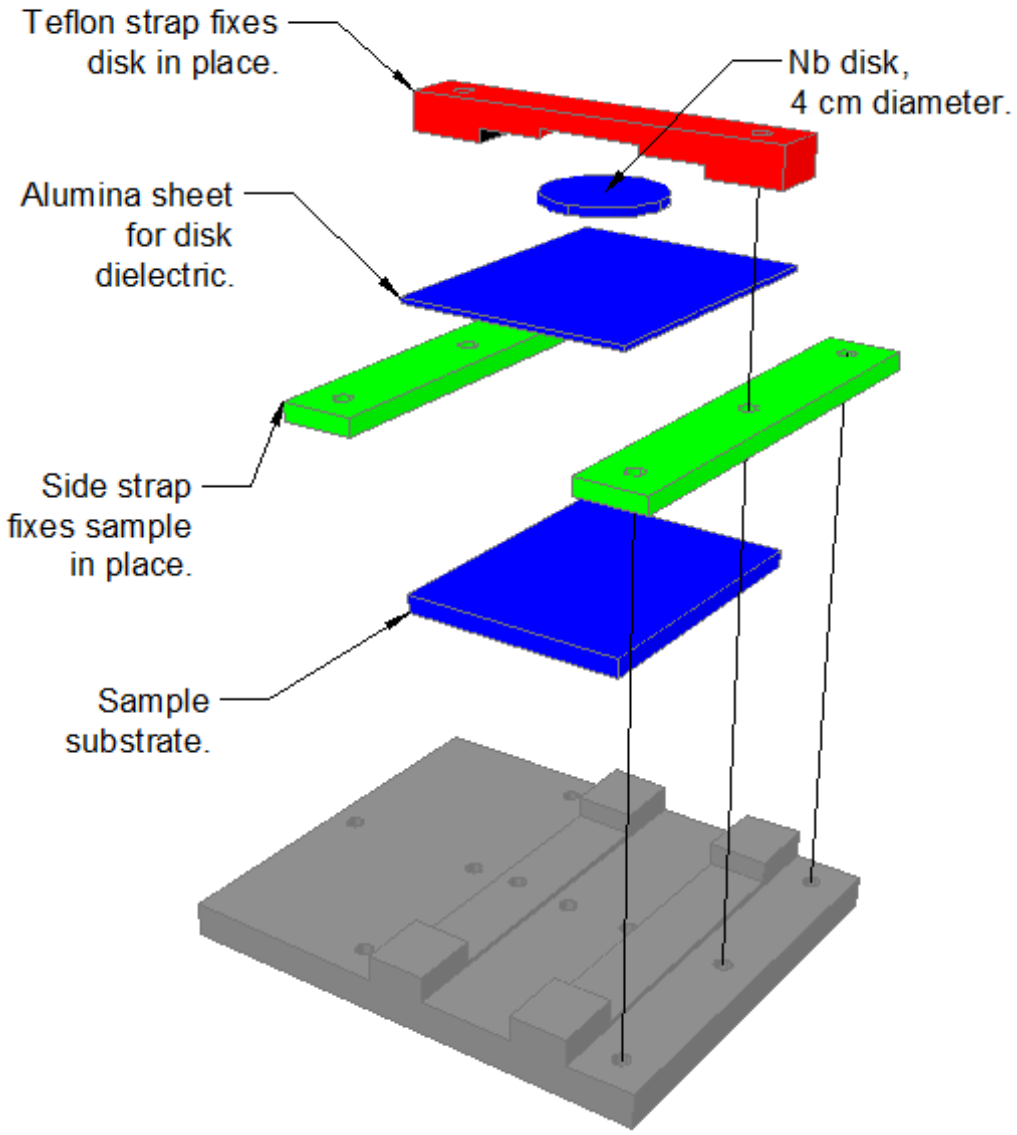

Figure 3.17: An exploded view of the sample holder, showing its several components. The same Nb disk and dielectric layer were used for every measurement.

Chapter 4

Thin films

The multilayer system in this work is composed of alternating thin films of niobium-titanium nitride and aluminum oxide - (Nb,Ti)N and Al_2O_3. These films were deposited in an ultra-high vacuum chamber via magnetron sputtering. The material properties of these films are described below, along with the methods of deposition and an analysis of the resulting material and superconducting properties.

4.1 Niobium-titanium nitride

(Nb,Ti)N was chosen for its specific superconducting properties. That is, it has a low value of H_{c1} and a high κ (see Section 3.5). It is also more mechanically and thermodynamically stable at room temperatures, and is deposited at lower substrate temperatures than similar superconducting nitrides [57, 61]. Finally, Jefferson Lab has several facilities available for the deposition of thin films via magnetron sputtering. For these reasons, (Nb,Ti)N is a very suitable material for this work.

Niobium-titanium nitride has applications in the fields of SRF, astrophysics, and the tool industry. It has been tested in SRF as a superconducting coating in elliptical copper cavities [63, 95]. As discussed in Section 1.6, the idea here is to improve the thermal conductivity, as well as the critical fields and temperatures of an elliptical cavity by using thin films of materials other than Nb. Copper cavities with thin (Nb,Ti)N coatings tend to have lower Q-values than bulk Nb cavities, and quench at lower gradients. (This is likely due to the relatively high surface resistance of (Nb,Ti)N below 4.2 K.) The same material is used in astrophysics for the fabrication of broadband THz mixers, used as components

in particle detectors [64, 96, 97]. The interest here is in thermodynamic stability, critical temperature, and low shot noise. Finally, (Nb,Ti)N has a hardness similar to that of TiN and is used to coat high-speed stainless steel cutting tools [98, 99].

From a materials science perspective, niobium-titanium nitride is not very well understood, either in terms of phase stability or in terms of the structure-process-properties relationship. The phase diagram of the Nb-Ti-N system is almost entirely unmapped. Several sources give isothermal or isobaric sections of the phase diagram, as in Figure 4.1, but only at temperatures above 1200°C [90, 100, 101]. Phase equilibrium data is unavailable at lower temperatures, likely because of the material's refractory nature. More recent works tend to focus on fabrication via reactive magnetron sputtering, but there is no apparent effort made to establish whether the resultant phases are in equilibrium.

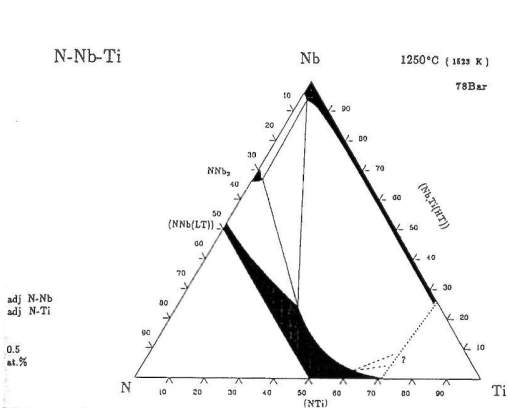

(a) Ternary phase isotherm at 1200°C.

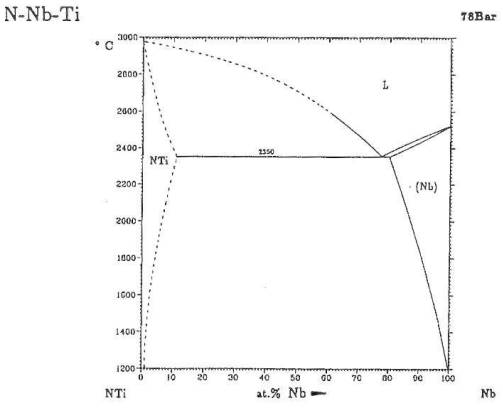

(b) T vs. x for $Nb_x(TiN)_{1-x}$ from 1200 to 3000°C.

Figure 4.1: The most complete Nb-Ti-N phase diagram available, reproduced from [100]. The notation "78Bar" in the upper right of both is a citation referring to a work in German: R. Kieffer, H. Nowotny, P. Ettmayer and G. Dufek, *Neue Untersuchungen über die Mischbarkeit von Überganhsmetallnitriden und -karbiden.* Metall, Berlin, **26**, 701-708 (1972).

Critical temperatures up to 18 K are achieved in (Nb,Ti)N by reactive diffusion of nitrogen in Nb-Ti alloys [101]. However, as is typical of diffusion-based fabrication processes, multiple phases and regions of stoichiometry coexist along the diffusion profile. Furthermore, the accidental incorporation of oxygen has been difficult to avoid, given the reactivity of both Nb and Ti [57, 90, 102, 103]. The formation of various phases has been correlated with the Nb/Ti ratio in the initial, un-nitrided sample [103]. Magnetron sput-

tering of thin films has the advantage of yielding fewer phases and less texture, depending on substrate preparation. In contrast to bulk nitridation, sputtered thin films tend to have critical temperatures in the range 12-15 K. This is likely the case because films with nm-scale grains have a much shorter mean free path than the corresponding bulk material. Magnetron sputtering is a more appropriate choice for the present work, since a UHV sputtering system already exists at Jefferson Lab, and because the temperatures required for reactive diffusion ($\gtrsim 1300°C$) are above the melting point (1085°C) of some copper system hardware.

The literature tends to be vague regarding the crystal structure of (Nb,Ti)N. Many authors make no attempt at any crystallographic analysis whatsoever, but only empirically relate the process conditions to the resulting critical temperature. Deposition processes are therefore optimized for this single parameter and no other analysis is done. This is especially true for SRF and astronomy applications, in which the end goal is a complicated device with many fabrication steps. The most explicit statement about the crystal structure of (Nb,Ti)N seems to be that it is a cubic, NaCl type[1] crystal structure, in which Nb and Ti form a substitutional solution with random occupation of metal sublattice sites, while N atoms occupy the nonmetal sublattice [91, 98, 100, 104]. The NaCl structure is maintained over a range of stoichiometries $Nb_{1-x}Ti_xN$ [61, 92, 99].

Pure niobium nitride is itself a candidate for SRF thin films: its cubic NaCl-type phase (referred to as the δ phase) has a critical temperature of approximately 16 K [105,106]. However, at temperatures below 1300°C the δ phase exists over a narrow range of nitrogen concentrations. Outside that range, the tetragonal γ-Nb_4N_3 and hexagonal, non-superconducting ϵ-NbN phases may also form, resulting in films with lower critical temperatures [101,107]. The Nb-N phase diagram is reproduced in Figure 4.2 from [108]. By contrast, the cubic δ phase of TiN is quite stable, existing over a wide range of temperatures and nitrogen concentrations but with a very low critical temperature, closer to 5 K [90]. The Ti-N phase diagram is shown in Figure 4.3. It seems that adding titanium to the Nb-N system[2] beneficially stabilizes the NaCl crystal structure at lower

[1] This is sometimes referred to as a B1 structure.

[2] As an alternative to Ti, some groups stabilize the δ-NbN phase by adding carbon [111]. This can be accomplished by introducing small amounts of CH_4 (around 2%) to the Ar/N_2 gas [105].

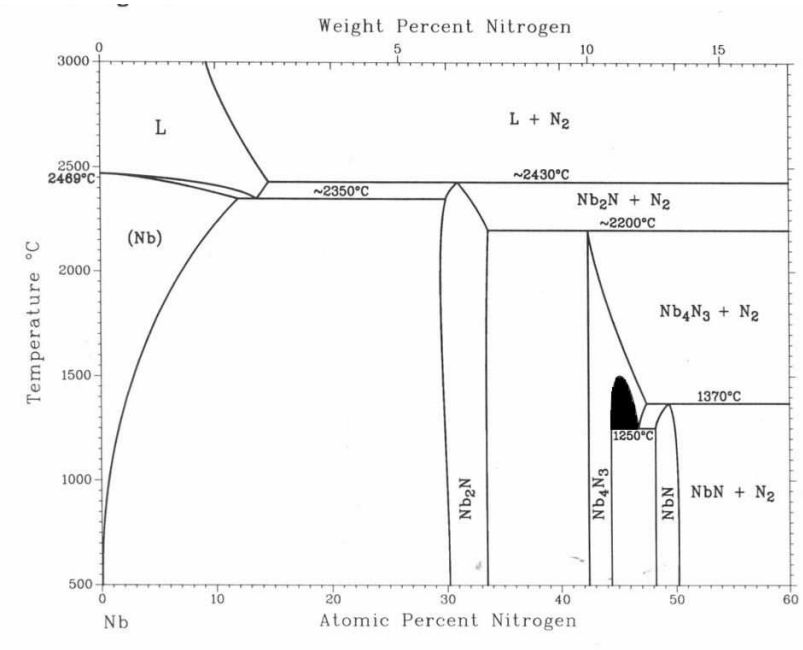

Figure 4.2: The Nb-N binary phase diagram, reproduced from [108]. According to Zhitomirsky *et al.*, the δ phase is formed in the black shaded region [107]. However, this seems topologically impossible in a binary phase diagram [109]. A more likely interpretation is that δ-NbN is formed in the region between approximately 48 and 50 atomic percent nitrogen. While this is a narrow range of compositions, δ-NbN is not evidently unstable at low temperature. This is supported by data in the ICDD Powder Diffraction File (04-004-2895, 04-004-2918) [110].

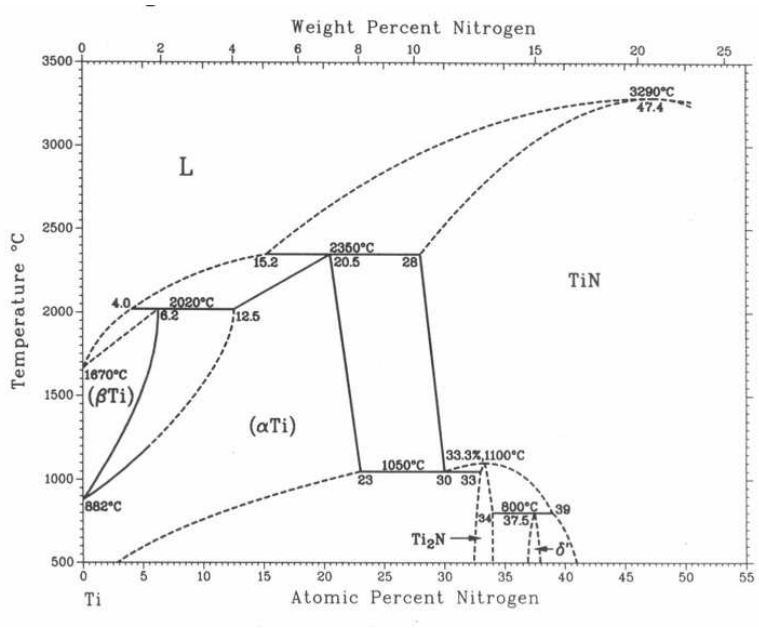

Figure 4.3: The Ti-N binary phase diagram, reproduces from [108]. The δ-TiN phase is shown at the right of the diagram, for temperatures up to 3290°C and compositions of >30 atomic percent N.

temperatures while retaining a high superconducting critical temperature [90, 101]. This phenomenon is supported by the data presented below. But first, a discussion of the methods of film production is appropriate.

4.2 The UHV system

(Nb,Ti)N films were deposited by DC reactive sputtering of a $Nb_{0.7}Ti_{0.3}$ target in a nitrogen environment. This process was performed in a vacuum chamber capable of reaching base pressures of 10^{-9} Torr - the ultra-high vacuum (UHV) range. This chamber was first discussed by Valente-Feliciano *et al.* in [112]. As the chamber was assembled in-house, its layout and operation will be discussed below. This section also discusses the process by which (Nb,Ti)N and Al_2O_3 films are deposited. Lastly, the chamber is still in its commissioning phase. The deposition process is still being refined, and modifications will be made to the process and the system hardware for months to come. Potential modifications to the system will be discussed at the end of this section.

4.2.1 The deposition chamber

A drawing of the UHV chamber is shown in Figure 4.4, along with the make and model of its various components. A simplified schematic is shown in Figure 4.5. The main chamber is bell-shaped, roughly 1.5 m high. The chamber is opened via a mechanical hoist, which lifts the upper section straight up. A 26-inch Wheeler flange joins the two sections, sealed with a Viton gasket.

As is typical, the chamber is evacuated in stages. Once the chamber is sealed, a scroll pump brings the pressure to approximately 30 mTorr. During this stage, a UVB lamp is switched on to encourage desorption of contaminants from the chamber walls. Below 30 mTorr, the scroll pump is valved off and a gate valve is opened between the main chamber and a 14-inch diameter cryopump. The chamber pressure quickly drops to 10^{-7} Torr, and after 24 hours of pumping will reach the 10^{-9} Torr range. An ion gauge monitors chamber pressure during this stage.

A residual gas analyzer (RGA) monitors impurities in the chamber and is used for helium leak checks. As in Figure 4.5, the RGA is connected to the chamber in two ways: by a six-inch VAT UHV gate valve and by a narrow, valved, bypass conductance. The bypass conductance keeps the RGA functioning at low ($\sim 10^{-6}$ Torr) pressures, even when the main chamber at process pressures of ~ 2 mTorr. Process gasses are introduced via variable leak valves. Since the chamber is still in its commissioning phase, there is not currently a mass flow controller to regulate, e.g., partial pressures of N_2 vs. Ar. In lieu of a mass flow controller, partial pressures are controlled by manually adjusting the leak valves while reading the RGA output. This method allows regulation of partial nitrogen pressure to within roughly 10%.

Three AJA magnetrons (model A320) are installed at the base of the chamber. They are all are water-cooled and can be used for both DC and RF magnetron sputtering. An Advanced Energy MDX-1K DC power supply is used for DC sputtering. RF power is provided by an Advanced Energy RFX-600 RF generator, coupled to the magnetron guns via an RF matching network (Seren MC-2, AT-10). The matching network is composed of two variable vacuum shunt capacitors, bridged by an inductor. The capacitors are automatically adjusted to match the chamber's plasma load to the RF generator impedance,

ensuring that minimal power is dissipated in the power cables (RG-393), the chamber walls, etc.

The chamber is housed in a cleanroom. All components installed in the system are first de-greased in an ultrasonic bath of Micro 90, an industrial detergent, followed by ultrasonic baths in various solvents. Copper components are additionally given an acid etch (55% phosphoric acid, 20% nitric acid, 25% acetic acid) in order to remove oils and other contaminants from the surface. These precautions help to ensure the purity of deposited films, and their regular practice helps ensure process control.

4.2.2 The sample holder

To ensure adequate film uniformity during reactive sputtering of NbTiN, a heated sample holder was constructed. A schematic is shown in Figure 4.6. The eight-inch CF flange is mounted horizontally into the UHV system at position "G" in Figure 4.4. The sample holder has several functions: it fixes the sample in place, provides uniform heating across the sample, and serves as a guide for a pattern mask (whose function is discussed below). The design also accommodates several chamber requirements. For example, the sample holder is mounted in a horizontal, 8-inch CF flange because all other work performed in the UHV system is mounted similarly.

The sample is bolted to the front of an OFHC copper heater block. The block is a cylinder, 12.7 cm in diameter and 6.35 cm long. The rear of the heater block, which is always under atmospheric pressure, houses sockets for a cartridge heater and a thermocouple for heating and temperature control.

A Waltow"Firerod" 500 W cartridge heater is inserted into a socket on the rear of the heater block. A K-type thermocouple mounted in the cylinder provides feedback for temperature control. Temperature regulation is handled via a Fuji Electronic Systems PXR-9 temperature controller, which opens and closes an Omron G3NA-210B solid state relay connected to 240 V AC. That wall-plug power drives the cartridge heater.

The main concern in designing the heated sample holder was the thermal gradient across the sample. This is complicated by the size of the sample substrate: $8 \times 10 \times 0.6$ cm. (Although the disk resonator itself is only 4 cm in diameter, accommodating the microstrip

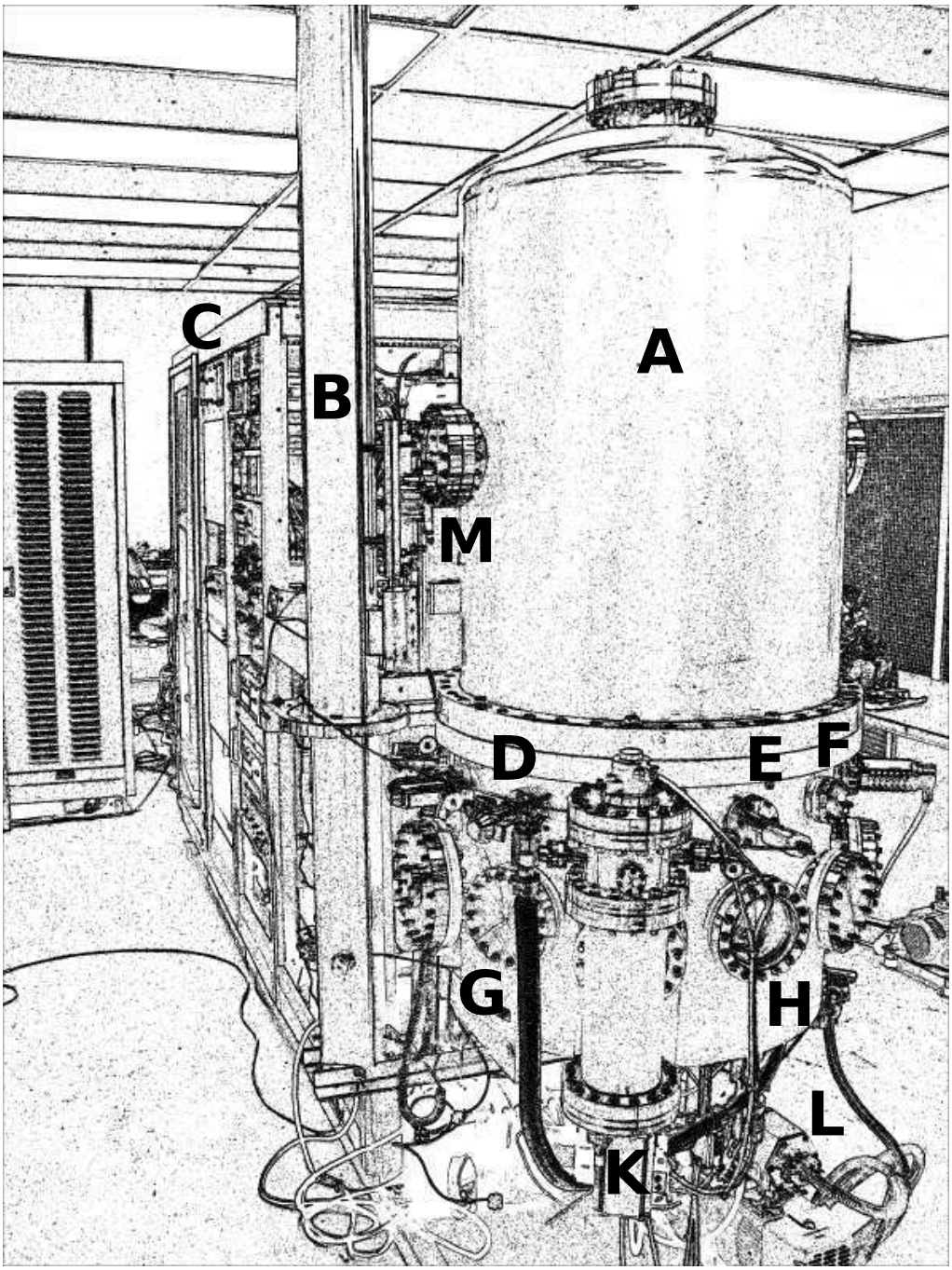

Figure 4.4: UHV chamber drawing. (A) Chamber; (B) Chamber hoist & support; (C) Instrumentation, control, RF/DC power supply; (D) N_2, O_2, Ar, Kr gas inputs (Varian variable leak valves); (E) Oscillator (Sycon OSC-100A), coupled to Sycon STM-100 thickness monitors; (F) Granville-Phillips 275 convection gauge; (G) 8" and 6" conflat ports for heater and shutter; (H) view port; (K) AJA Int'l. A320 magnetron guns, with coolant and power supply lines; (L) Itawa 5700 scroll pump; (M) UVB lamp. NOT SHOWN: Granville-Phillips Stabil-Ion process ion gauge; CTI Cryo-Torr 10 14" cryo-pump; VAT gate valve; Pfeiffer TMU-071 turbopump, residual gas analyzer (Pfeiffer Prisma 80).

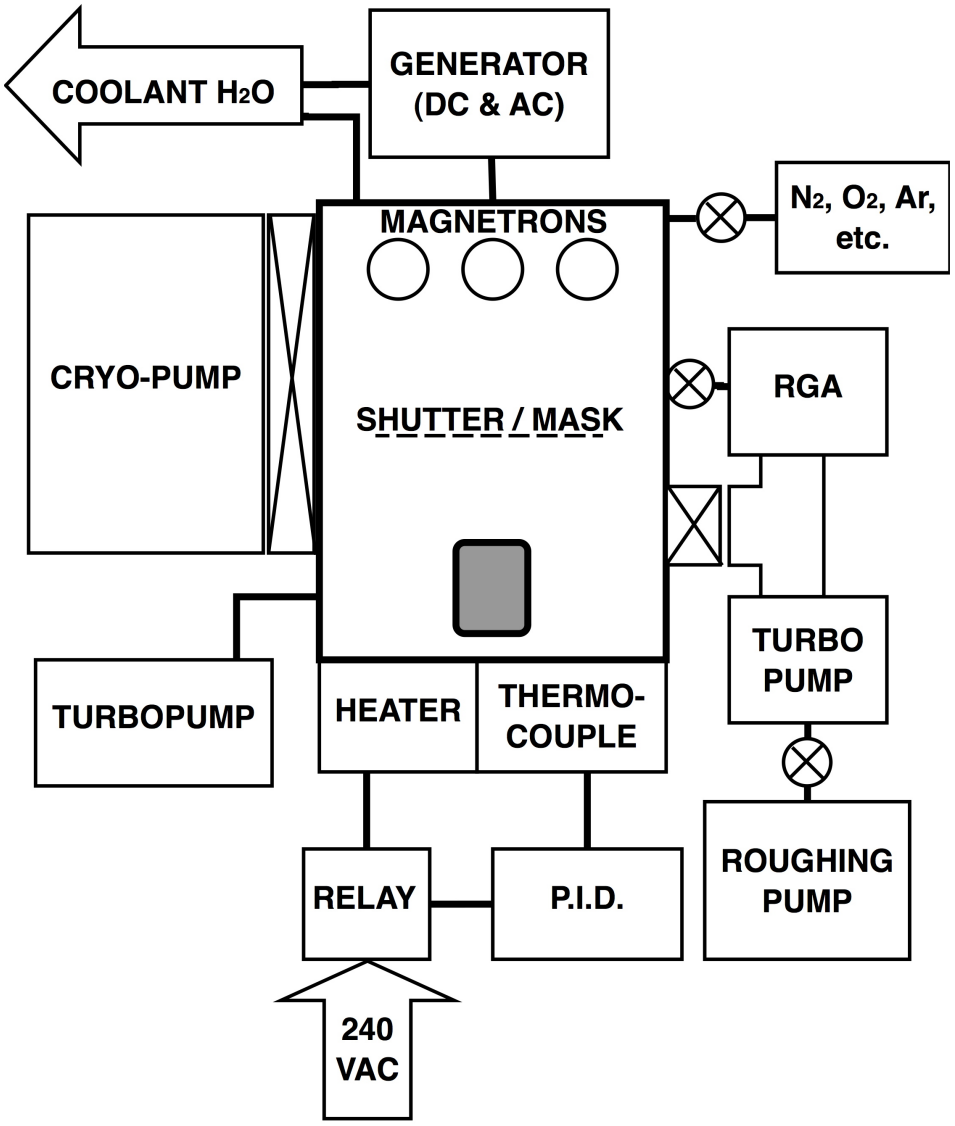

Figure 4.5: Simplified UHV chamber block diagram.

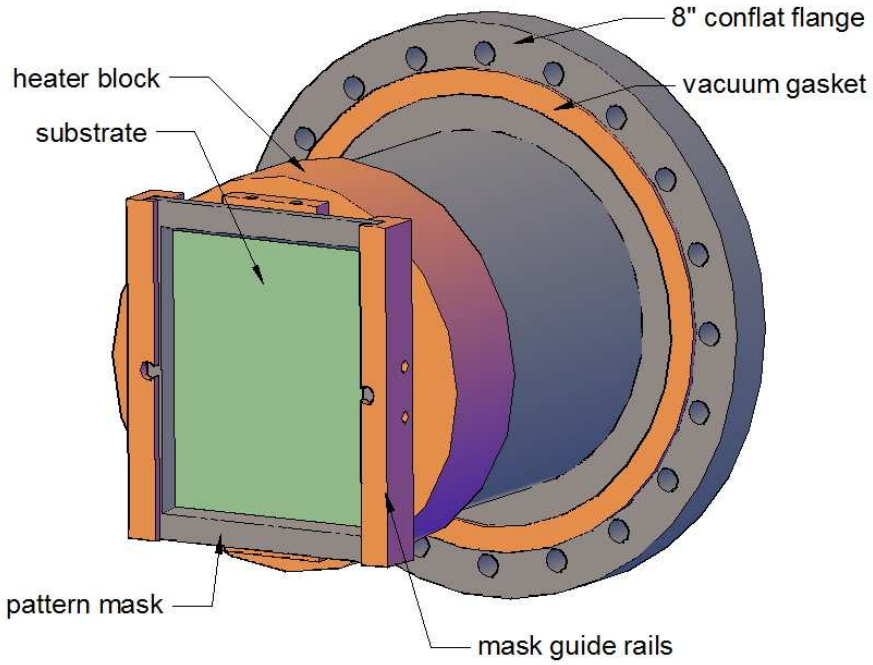

(a) Front view (chamber side).

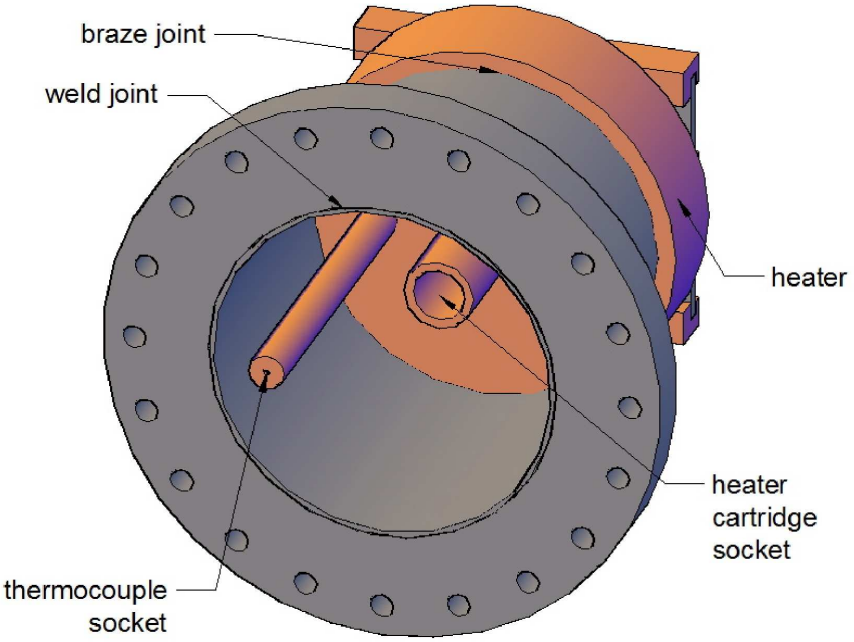

(b) Rear view (atmosphere side).

Figure 4.6: Heated sample holder schematic.

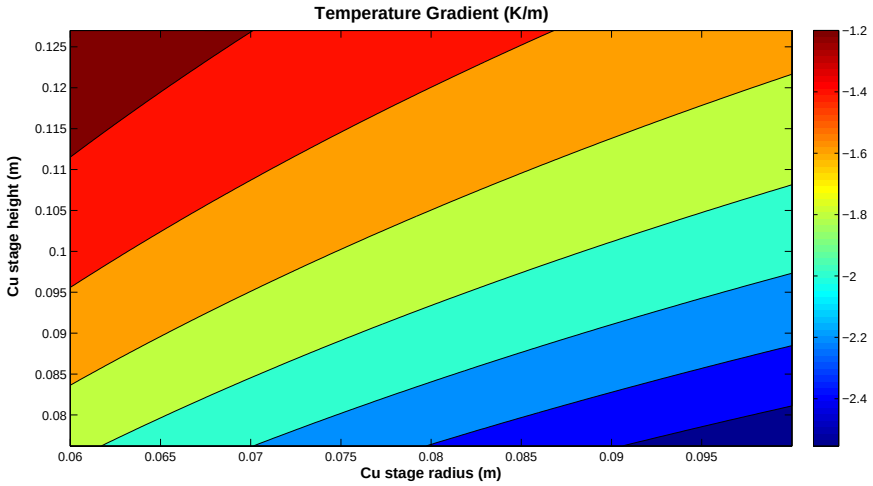

Figure 4.7: Thermal gradient across sample for various sizes of heater. No reasonable choice of heater dimensions results in a gradient of more than a few Kelvin.

input and output couplers requires a larger substrate.) The temperature of the substrate must be uniform across its face to within a few Kelvin. This is verified by integrating Fourier's law for heat conduction

$$\dot{Q} = -kA\frac{dT}{dr},$$

where r is the radial coordinate, $\dot{Q}$ is the rate of heat transferred to the copper cylinder, $k = 401$ W/m·K is the thermal conductivity of copper, A is the area normal to the heat flux (which in this case varies with r), and T is temperature.

The heater block is modeled as a uniform cylinder with length ℓ and an outer radius r_2. A hole of radius r_1 is drilled through the center to accommodate the cartridge heater. Integrating in cylindrical coordinates gives the thermal gradient across the heater face as

$$\Delta T = -\frac{Q\ln(r_2/r_1)}{2\pi k\ell}.$$

For reasonable values of r_2 and ℓ, with $r_1 = 1.9$ cm, the thermal gradient is shown in Figure 4.7. Evidently, any reasonable choice of cylinder dimensions will give negligible thermal gradient across the sample.

In preparation for deposition, the heater block is brought to 600°C and kept at that temperature for four hours. This heat treatment stimulates desorption of impurities from

the sample and facilitates the transition from the high vacuum regime at 10^{-7} Torr to the UHV regime at 10^{-9} Torr.

4.2.3 Magnetron sputtering

Deposition begins once the chamber has been evacuated to UHV pressures, a helium leak check has been performed, and the substrate has been held at 600°C for some time. At that point, the sputtering gas is introduced and the gas pressure is adjusted as described above. (Nb,Ti)N films are reactively sputtered so the ratio of partial pressures $P(N_2)/P(Ar)=0.15$ for an overall process pressure of 2 mTorr[3], as measured by an ion gauge.

For both (Nb,Ti)N and Al_2O_3 films, the sputtering target is covered with a movable shutter. The target face is then conditioned for thirty minutes. That is, a plasma is struck and the target is sputtered for some time to remove impurities and stabilize the temperature at the target face. The mask ensures that no sputtered particles reach the substrate before the system is in equilibrium.

Sputtering of (Nb,Ti)N films

As mentioned above, (Nb,Ti)N films are formed by reactively sputtering a $Nb_{0.7}Ti_{0.3}$ target in an N_2/Ar gas mixture. The plasma is lit with 60 W DC power from a power-stabilized ENI DCG-100 generator, designed for plasma operation. The power is then ramped to 300 W, corresponding to 0.88±0.01 A and 340±5 V at the cathode. Power stabilization, as well as the ensuing stability of cathode voltage and current settings, support an equilibrium deposition rate.

For "good" films, these gas and cathode settings give a deposition rate of 16.0±0.3 nm/min as measured afterward with a profilometer. Although there are two thickness monitors mounted in the deposition chamber, these are used mainly for qualitative assessments of sputter conditions. That is, plasma density varies with distance from the target face, so meaningful quantitative measurements with thickness monitors are only possible if they obstruct the path between the target and the substrate. As an alternative, trial films were deposited on a-plane sapphire substrates (single crystals, polished to 90 Å mean surface

[3]Since an RGA is used in lieu of a mass flow controller, it is more accurate to say that "15%" describes the ratio of ion currents in the RGA chamber. The partial pressures are inferred, but not measured directly.

roughness, with ∼1 cm^2 surface area) and the thickness of these films was measured later using a profilometer. Similarly, during deposition on the large, 8×10 cm substrates used for the disk resonators, sapphire witness samples were used to perform *post-facto* analysis of superconducting and surface properties; the full-size samples are too large and heavy to fit in, e.g., a diffractometer.

Those small sample measurements, then, form the basis for all statements of thickness and deposition rate. Film thickness is controlled, then, by controlling the partial gas pressures and timing each deposition according to the above-stated deposition rate. Excluding target conditioning, it takes approximately 9 minutes and 20 seconds to deposit 150 nm of (Nb,Ti)N. At the end of the deposition window, the target shutter is replaced and the gas and magnetron power are switched off.

Sputtering of Al_2O_3 films

Alumina films are formed by RF magnetron sputtering of an alumina target in an Ar plasma. The plasma is lit with 65 W, 13.56 MHz RF power, at gas pressures above 8 mTorr. Once the plasma is lit, the forward power is ramped slowly to 120 W, beyond which there is no appreciable change in the deposition rate. The working Ar pressure is held as low as is reliably possible (roughly 0.8 mTorr) to maximize the mean free path of sputtered particles and to keep the cryopump temperature stable. After the matching network is tuned, most of the forward power is delivered to the magnetron and only 1-3 W are reflected back. Deposition rates are characteristically low for the RF sputtering of alumina: approximately 1.2 nm per minute.

Al_2O_3 was chosen because it was readily available as a dielectric target material; as polished substrates for the creation of small samples; and as bulk, 2 mm sheet for the thick dielectric layer under the disk resonator. Using the same material for all three purposes simplifies multilayer analysis. However, there is a noteworthy complication. The best alumina films - that is, the films with the highest dielectric constant and breakdown voltage - are those in which alumina is deposited via *reactive* sputtering in an argon/oxygen mixture [113–115]. The presence of oxygen in the Nb-Ti-N system would form oxide compounds in the superconducting layers via reactive diffusion, with an oxidation rate on the

order of 1 mg/cm^{2}h [116, 117]. This is an unacceptable contamination that could result in lower T_c values via, for example, N→O substitution in the lattice [118].

After deposition, all samples are held at 600°C for several hours and then cooled over a period of 12 hours at UHV pressures. The small samples' surface and superconducting properties can then be studied directly, while the resonator substrates can be prepared for multilayer analysis.

4.3 Film analysis

Film analysis falls into two broad categories. Superconducting properties are studied chiefly by DC measurements of the critical temperature T_c. Assessments of crystal structure and surface properties are made using a suite of surface-analytical tools available at Jefferson Lab: profilometry, atomic-force microscopy (AFM), energy dispersive x-ray spectroscopy via scanning electron microscope (SEM-EDS), and x-ray diffractometry (XRD). The results of these studies are presented here.

The goal of this work is the development of an experimental program for multilayer film analysis. As such, a complete determination of the crystal structure of (Nb,Ti)N was not undertaken. However, there are several conclusions about crystal structure that were be made in the course of structural analysis for the sake of process refinement.

4.3.1 T_c measurements

The superconducting properties of thin films may be assessed and compared most conveniently at Jefferson Lab via simultaneous measurements of the critical temperature, T_c, and the residual resistivity ratio, RRR. This is accomplished via the standard four-point probe analysis [119–121]. Four parallel, spring-mounted, gold-plated probes are placed in contact with a sample film. The two outer probes (see Figure 4.8) supply a known DC current, while the two inner probes measure the subsequent induced voltage. The resistivity can then be measured.

The apparatus is placed in a dewar in the VTA and cooled to cryogenic temperatures. Then a heater in the dewar slowly warms the test apparatus so that resistivity can be measured between 2 and 300 K, typically at intervals of 0.1 K over a period of roughly

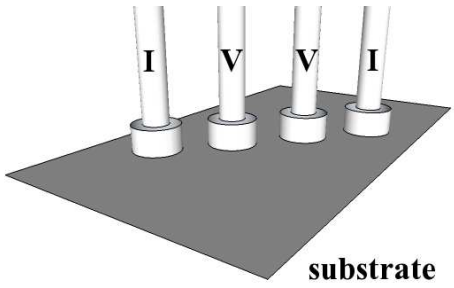

Figure 4.8: Cartoon showing four-point probe configuration for T_c and RRR measurements. Current leads **I** and voltage leads **V** are shown.

12 hours. The transition between the superconducting and normal states is indicated by a sharp increase in the measured DC resistivity, as shown in the figures below.

Process development for (Nb,Ti)N films in the JLab UHV system is still underway. Maximizing T_c and film uniformity is an ongoing part of chamber commissioning. For the purposes of this thesis, it is sufficient to determine a chamber state that will repeatably produce films with values of T_c comparable to those found in the literature for similar substrates and deposition methods. The chamber state is found empirically by depositing and characterizing a wide range of thin films under varying deposition conditions.

The nitrogen partial pressure during deposition strongly influences the superconducting properties of the resulting films. A subset of the film data is presented, then, in two groups. One group, "Group A", shows the influence of partial nitrogen pressure on film characteristics. Three Group A films are referenced below to illustrate differences resulting from nitrogen partial pressure $P(N_2)$: Sample 01 ($P(N_2)$ =10%), Sample 02 ($P(N_2)$ =15%), and Sample 03 ($P(N_2)$ =5%). Another group, "Group B", is composed of films deposited under nominally identical conditions and showing similar, relatively high values of T_c. The Group B films represent some degree of process control and repeatability. T_c and RRR measurements of both groups are shown in Figures 4.9a and 4.9b, respectively. The net result is that for this experiment, $T_c = 13.2 \pm 0.5$ K and RRR=1.46±0.58. RRR is far more variable that T_c, suggesting relative control of stoichiometry (which strongly influences T_c, see Section 4.1) but run-by-run changes in microstructure.

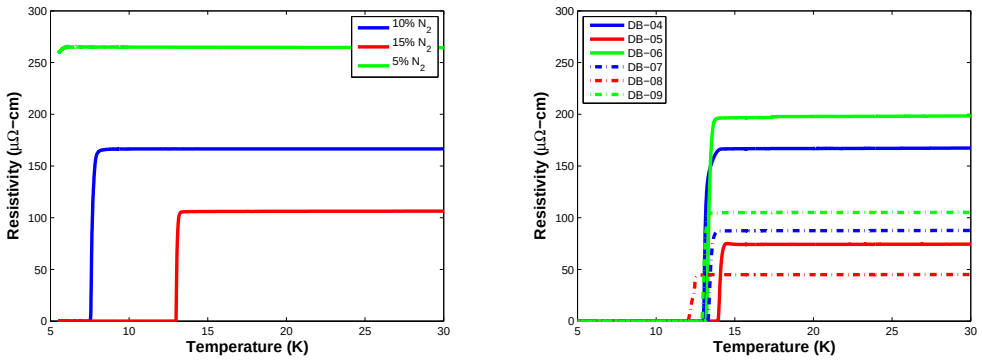

(a) Group A: T_c varies with $P(N_2)$.

(b) Group B: $T_c = 13.2 \pm 0.5$ K.

Figure 4.9: Varying the partial nitrogen pressure during deposition results in widely varying superconducting parameters. Figure 4.9a shows Group A films: Sample 01 (blue, 10% $P(N_2)$), Sample 02 (red, 15%), and Sample 03 (green, 5%). Sample 03 has a transition temperature below 5.6 K. Group B results are comparable to those found in [63], e.g. Figure 4.9b shows data for six films, all deposited under nominally identical conditions and demonstrating the repeatability of creating films with $T_c \approx 13$ K.

4.4 Surface analysis

Apart from superconductivity, in order for films to be useful for the analysis and interpretation of multilayer structures, they must be smooth and their thickness must be known. A smooth film ensures a clean interface between superconducting and insulating layers, with no pinholes or shorts between conducting layers. It also drastically simplifies the vortex image problem, so that the calculations from Chapter 2 might still apply. And in order to have any *a priori* understanding of Q or H_v in a multilayer resonator, the film thickness must be known. Atomic force microscopy (AFM) and profilometry measurements were conducted to address these issues. The results are discussed below.

The present work is the beginning of a long-term multilayer film study in which (Nb,Ti)N will have a nontrivial role. To the extent that the deposition process may be better understood, both for this and for future analyses, some further amount of material characterization is useful. To this end, x-ray diffraction (XRD) and energy-dispersive x-ray spectroscopy (EDS) measurements were conducted, and are discussed below.

All surface analysis was conducted on small samples. As discussed in the previous section, there are two groups of samples. In the first group, Group A, the partial nitrogen

pressure was varied during deposition Samples made at three different values of $P(N_2)$ give a rough idea of the influence of sputter conditions on film structure. In the second group, Group B, samples were deposited with the goal of uniformity and repeatability, resulting in critical temperatures of 13.2±0.5 K. Group A is used to show the effects of varying deposition conditions on the resulting film structure. Group B is used to discuss the general properties of (Nb,Ti)N.

It is worth stating explicitly that more measurements must be made on more samples before any sound, statistical conclusions can be drawn. The results presented below form the basis for *qualitative* analysis.

4.4.1 Thickness measurements

Measurements of film thickness were made using a Dektak 3ST surface profiler. Small samples are clipped to the heater block. The clip masks part of the sample substrate, creating a step in the film height which can then be measured. A stylus, scanned across the step, records the change in film height. Multiple scans across each step give the results shown in Figure 4.10.

The samples in Figure 4.10b were made under varying partial nitrogen pressures, but with equal deposition time. This variable deposition rate may be influenced by the reaction of nitrogen with the target surface. A partial nitridation of the target would lower both the sputtering yield and the secondary electron emission coefficient[122]. Furthermore, the cross section for ionization of N_2 by electrons is 40% lower than that of Ar, leading to a reduced ion density in the plasma [123]. As stated above, films in Group B have deposition rates on the order of 16 nm/min.

4.4.2 AFM

Recall from Chapter 2 that the Gurevich model of vortex behavior in a multilayer structure is dependent on a smooth interface between film layers. Quantifying the RMS surface roughness is then one way of evaluating multilayer films. Root meas square (RMS) surface roughness measurements were conducted using a Digital Electronics scanning probe microscope in tapping AFM mode. Data from each sample reflects three separate measurements, each taken over an area of 25.30±0.11 μm^2. Typical results are shown in

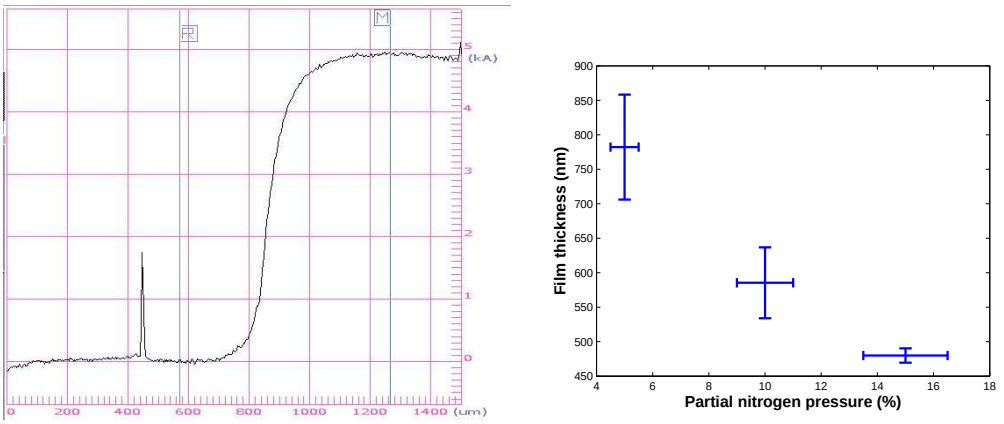

(a) Dektak 3ST sample output. (b) Thickness vs. $P(N_2)$.

Figure 4.10: Measurements of film thickness for samples under varying deposition conditions, but equal deposition time.

Figure 4.11. RMS surface roughness as a function of partial nitrogen pressure is shown in Figure 4.12. The RMS surface roughness is then on the order of 1 nm for films up to 800 nm thick. From Figures 4.11b and 4.11d, the lateral length scale is estimated[4] to be on the order of 50 nm. There are several mechanisms contributing to the surface roughness shown in Figures 4.12 and 4.10. It is well-known that films deposited via magnetron sputtering (i.e. with limited adatom mobility) tend to have small grain sizes with irregular columnar morphologies. Consider the Thornton zone structure model, developed from earlier work by Movchan and Demchishin, which qualitatively relates morphology to homologous deposition temperature[5] and sputtering gas pressure [124]. From Figure 4.2, the homologous temperature during deposition $T/T_{\mathrm{m}} \approx 0.25$ suggests small, columnar grains with grooved, metallurgical boundaries. Such grains grow slowly during deposition, resulting in conical grain structures. Given the estimated lateral length scale of $\sim$50 nm discussed above, this morphology suggests 50 nm as a rough grain size at the film surface. In addition, the random deposition of particles may lead to roughening via kinetic processes [125]. Given that surface roughness and grain boundary density have an effect on the behavior of magnetic flux vortices, this suggests avenues for further study. That is, an increased grain size could result in increased surface roughness, suggesting a

[4] Unfortunately, the original AFM data files could not be recovered, precluding a more precise measurement of lateral length scales via power spectral density analysis, e.g.

[5] "Homologous" refers to material temperature T normalized to its melting temperature T_{m}.

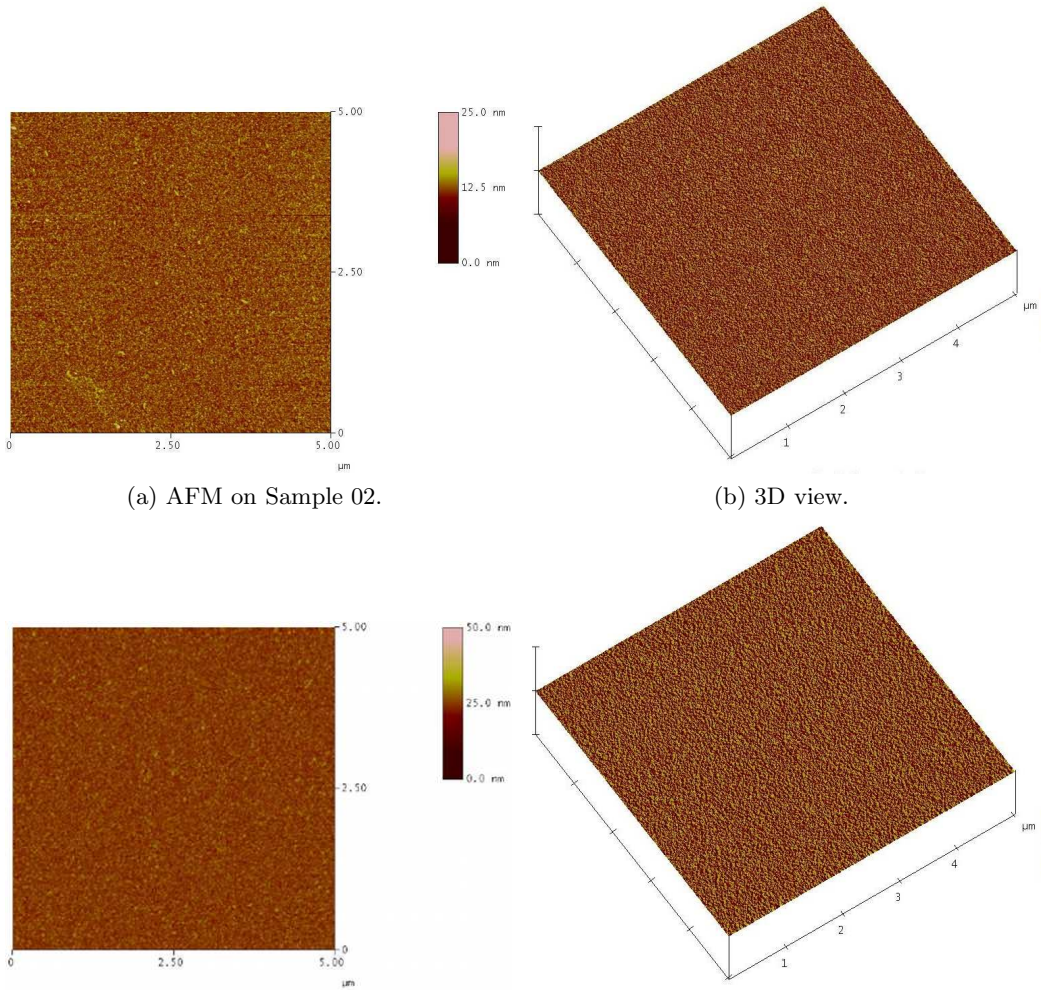

(a) AFM on Sample 02.

(b) 3D view.

(c) AFM on Sample 03.

(d) 3D view.

Figure 4.11: 25 μm^2 AFM scans of Sample 02 (T_c=13 K) and Sample 03 ($T_c < 5.6$ K), showing a uniform surface.

compromise between the two might be necessary.

4.4.3 Further analysis

Composition and phase studies have also been conducted using XRD and SEM-EDS. A full crystallographic analysis of (Nb,Ti)N will be conducted after the UHV chamber is fully commissioned and the deposition process has been further refined. However, several conclusions can be drawn at this preliminary stage.

First, standardless FAZ component analysis [126] was conducted using an EDAX

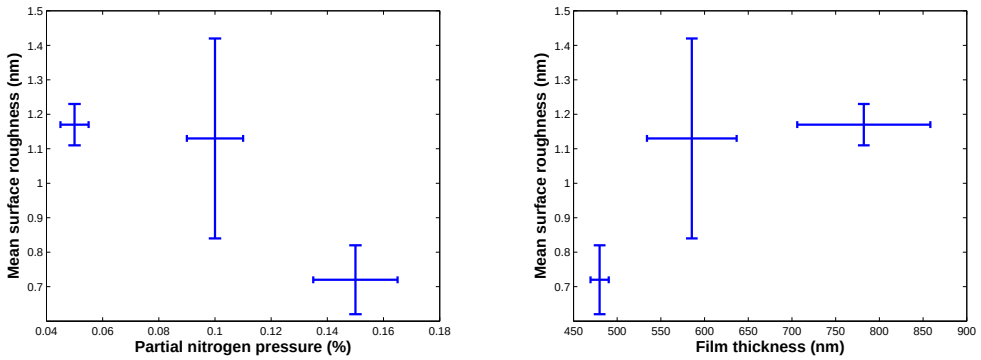

(a) Group A RMS surface roughness vs. $P(N_2)$. (b) RMS surface roughness vs. thickness.

Figure 4.12: RMS surface roughness data for Group A samples 01-03, showing a trend towards roughness as films increase in thickness. Since these films were all deposited at different nitrogen partial pressures, a clear determination of the dependence of roughness on film thickness is difficult.

SEM-EDS system. A typical x-ray emission spectrum (Figure 4.13) shows the films to be quite clean. That is, the films are composed primarily of nitrogen, niobium, and titanium. There is evidence for carbon contamination in a small minority of samples, explained by the solubility of carbon in transition metal nitride systems [99]. Hydrogen and oxygen are also likely contaminants. However, SEM-EDS is ineffective for elements with $Z \leq 4$ and so insensitive to hydrogen, and the presence of oxygen in the sample substrates makes its detection in the film impossible. Compound identification via X-ray photoelectron spectroscopy is therefore a likely next step in material analysis.

X-ray diffraction studies were performed using a Panalytic X'Pert Pro four-circle diffractometer. $\theta - 2\theta$ measurements in the Bragg-Brentano geometry (Figure 4.14) suggest a B1 configuration, as discussed above. Coherent reflections are evident for "unmixed" Miller indices, from which a lattice parameter $a_0 = 4.3$ Å is calculated. Only the [111] and [200] orientations are visible. A high degree of disorder is suggested as well, since these peak intensities are quite low compared with that of the sapphire substrate. A natural degradation of intensity with increasing θ may be the reason why no peaks were visible above $2\theta \sim 45°$ [127].

Data from the ICDD[6] powder diffraction file (PDF, Reference [110]) are compared

[6]International Centre for Diffraction Data. http://www.icdd.com

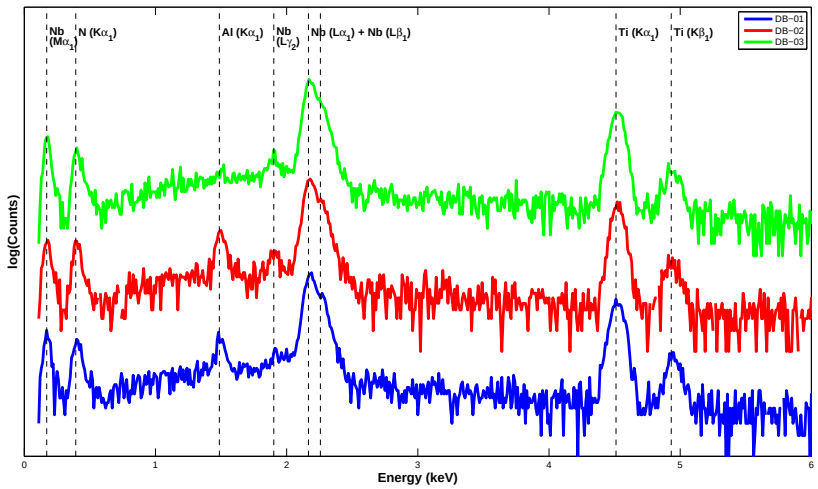

Figure 4.13: EDS peak intensity vs. critical emission energy (keV) for Group A. Only N, Nb, Ti are present - film contamination is atypical. The "shoulder" on the Nb Mα_1 peak is likely from C $K\alpha$.

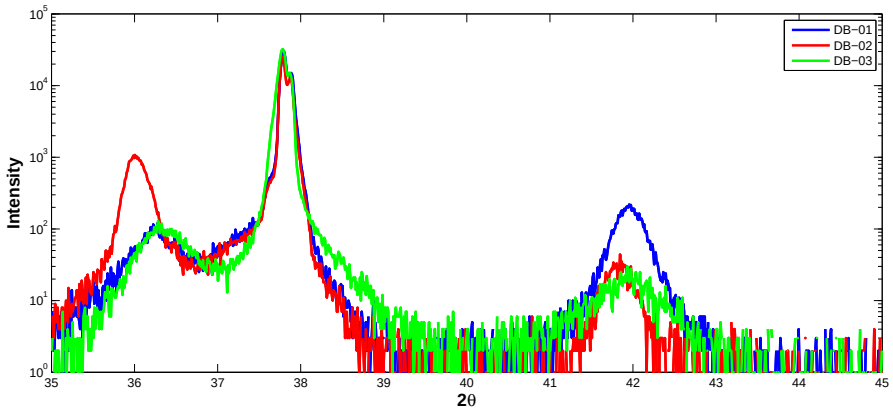

Figure 4.14: Bragg-Brentano XRD scan for samples in Group A. The prominent center peak is created by the sapphire substrate.

with Group A data in Figure 4.15. In particular, diffraction peaks from the possible cubic phases of the Nb-N and Ti-N systems are shown. A comparison of 2θ-values for these phases strongly suggests that δ-(Nb,Ti)N is indeed formed during reactive sputtering.

As previously stated, SEM-EDS measurements suggest the predominance of Nb, Ti, and N in the films used for this work. Figure 4.15 shows the relationship between the structure of those films and that of the various δ phases that are possible in the Nb-Ti-N system. Of course, there are other, non-cubic phases possible given the deposition temperature. Figure 4.16 compares PDF x-ray diffraction spectra [110] for various non-cubic phases of the Nb-Ti-N system. Again, the location of diffraction peaks strongly suggests the formation of δ-(Nb,Ti)N films.

Figure 4.17a shows a closeup of the (111) peak from Figure 4.14. The 2θ value is compared with those of ideally stoichiometric NbN and TiN [128, 129]. The lattice parameter of (Nb,Ti)N therefore seems to be a compromise between those of NbN and TiN, also shown in Figure 4.15. The lattice parameter also seems to vary with the relative concentrations of Nb and Ti. However, SEM-EDS composition data empirically show no substantial variation in Nb-Ti relative composition. Then (Nb,Ti)N does not appear to follow Vegard's law [130], so plots like Figure 4.17c do not trivially yield composition data. Variations in the lattice parameter a_0 are likely due to a combination of film stress and nitrogen partial pressure.

The XRD peaks for Group B samples tend to be quite broad and of low intensity, compared with those measured by other groups [90, 120]. The low intensity is likely due to very small grain size. A rigorous study of grain size in (Nb,Ti)N films will require measurements made using a transmission electron microscope. Absent such a set of measurements, a rough estimate of grain size can be made from the width of diffraction peaks. Specifically, the Scherrer equation [131] relates the full width at half maximum (FWHM) of a diffraction peak to the width β of a crystallite:

$$\text{FWHM} = \frac{K\lambda}{\beta \cos\theta}. \tag{4.1}$$

Here, $\lambda = 0.154$ nm is the x-ray wavelength (Cu Kα), θ is the Bragg diffraction angle, and K is a dimensionless factor of order 1, determined by the grain shape. Using the peak widths in Figures 4.17a and 4.17b, and assuming a spherical grain shape ($K \approx 1.3$), the

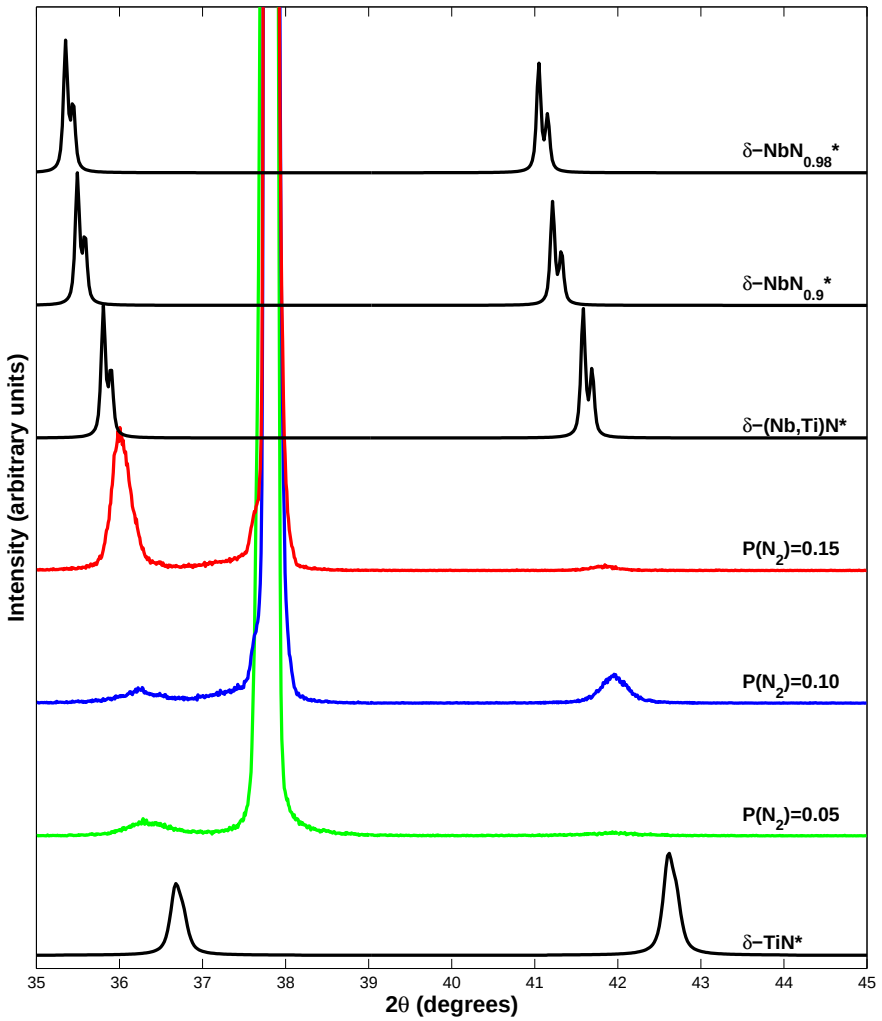

Figure 4.15: Bragg-Brentano x-ray diffraction spectra for Group A films deposited at various partial nitrogen pressures, compared with PDF data for other possible cubic phases: δ-TiN (PDF 00-038-1420), δ-$Nb_{0.5}Ti_{0.5}N$ (PDF 01-089-5134), δ-$NbN_{0.9}$ (PDF 04-004-2918), and δ-$NbN_{0.98}$ (PDF 04-004-2895). In the plot, an asterisk (e.g. "δ-TiN*") indicates a diffraction spectrum that was obtained from the ICDD powder diffraction file rather than measured directly. There is a gradual shift in 2θ values between stoichiometric TiN and NbN peaks, with δ-(Nb,Ti)N peaks in the middle. The strong peak at $2\theta = 37.8°$ for the Group A films originates from the a-plane sapphire substrates.

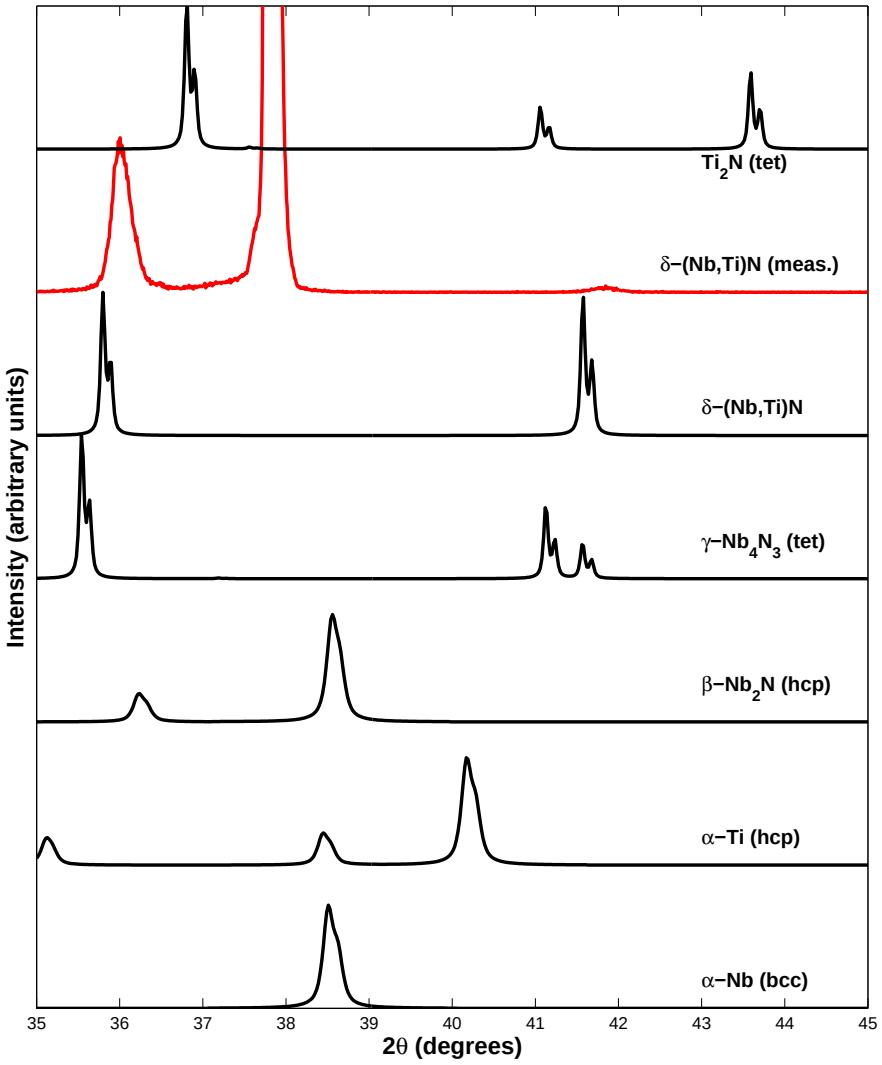

Figure 4.16: Bragg-Brentano x-ray diffraction spectra for deposited films (shown in red) compared with PDF spectra for δ-$Nb_{0.5}Ti_{0.5}N$ (PDF 01-089-5134), α-Nb (PDF 00-034-0370), α-TiN (PDF 00-044-1294), β-Nb_2N (PDF 00-039-1398), γ-Nb_4N_3 (PDF 01-089-5132), and Ti_2N (PDF 04-007-0773). The abbreviation "bcc" indicates a body-centered cubic phase, "hcp" indicates hexagonal, and "tet" indicates tetragonal. The measured diffraction peaks correspond closer to the δ-(Nb,Ti)N phase than to any other accessible, non-cubic phase of the Nb-Ti-N system.

Scherrer equation gives a grain size between 30 and 50 nm, in rough agreement with the estimates from AFM discussed above. Note that Equation 4.1 represents a lower bound on grain size. Other phenomena, such as inhomogeneous film strain, can also contribute to peak broadening [127]. Small grain sizes result in a high density of grain boundaries, which can in turn influence the behavior of flux vortices in the film. Specifically, vortices may penetrate a superconductor at lower magnetic fields than in equivalent single-crystal material [132].

Eventually, the experimental system described in Chapter 3 will be used to accumulate a statistically large amount of data, such that concrete conclusions may be made concerning (Nb,Ti)N film composition and its effect on superconducting behavior. In addition, the commissioning of the UHV system (Section 4.2) will involve small (Nb,Ti)N samples made under a variety of deposition conditions. For example, it is not now clear where the maximum lies in the relationship between partial nitrogen pressure and T_c, from Figure 4.9a. The qualitative observations made in this section suggest directions of inquiry for future work in (Nb,Ti)N process development.

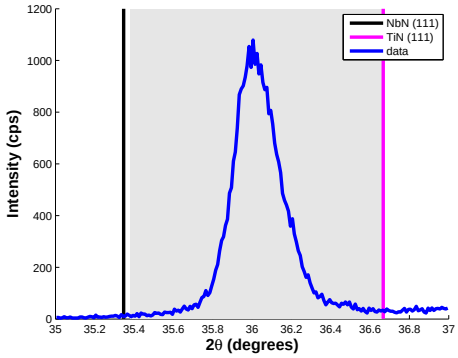

(a) Closeup of 111 peak, Group B.

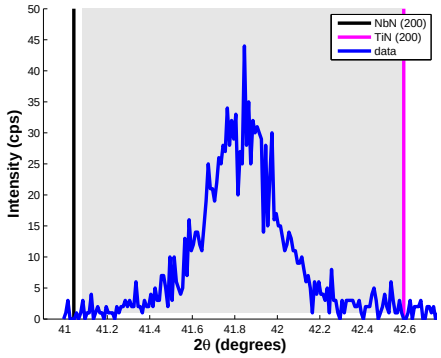

(b) Closeup of 200 peak, Group B.

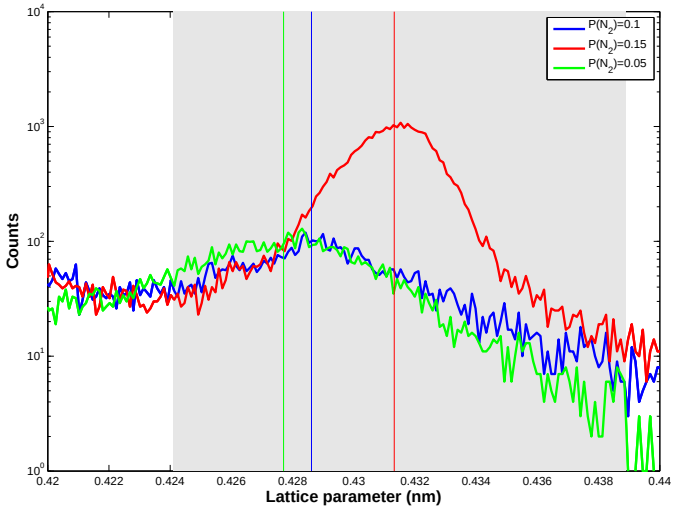

(c) a_0 varies with partial N_2 pressure.

Figure 4.17: Plots of the (111) and (200) peak for various samples, giving information about the lattice parameter a_0. The gray band in Figures 4.17a-4.17c represents the range of a_0 values given in [100].

Chapter 5

Preliminary RF measurements and conclusions

This dissertation has presented an experimental program to evaluate multilayer films for SRF. Preliminary results are presented here, and the RF measurement apparatus is described. Finally, since the present work represents the start of a long-term analysis, plans are discussed for modifications and improvements to the apparatus.

The measurements discussed in this chapter demonstrate a proof of principle. The resonator works at its design frequency, the measured Q is close to predicted values, and the variable couplers can be manipulated to obtain critical coupling, as discussed in Section 3.6.2.

5.1 RF measurement apparatus

It is often the case that measurements of SRF cavities require special hardware for frequency stabilization of RF power sources. A cavity with $Q_0 \sim 10^9$ may have a bandwidth on the order of 1 Hz. In that case, slight changes to the cavity from vibration or electromagnetic field pressure are enough to move the cavity off-resonance. For example, the VTA at Jefferson Lab uses phase-locked loops to correct the forward RF power in real time, constantly adjusting the frequency to compensate for any detuning effects.

By contrast, the disk resonator has a calculated bandwidth $\Delta f = f/2Q_0 = 1.3$ MHz. Operation at resonance is therefore stable, and can be maintained simply by using a vector network analyzer (VNA) as a source of RF power. The low output power (< 10 mW) of

the VNA is amplified through a 34.4 dB S-band traveling-wave tube amplifier (TWTA), which nominally provides up to 25 W forward power to the resonator. The configuration of this and other assorted RF hardware is shown in Figure 5.1. Note that, at the time RF measurements were conducted, it was not possible to calibrate the VNA. Measurements of Q, S_{11}, and S_{21} therefore include all sources of loss between the ports of the network analyzer. Measurements with a Hewlett-Packard 437B RF power meter show that, in

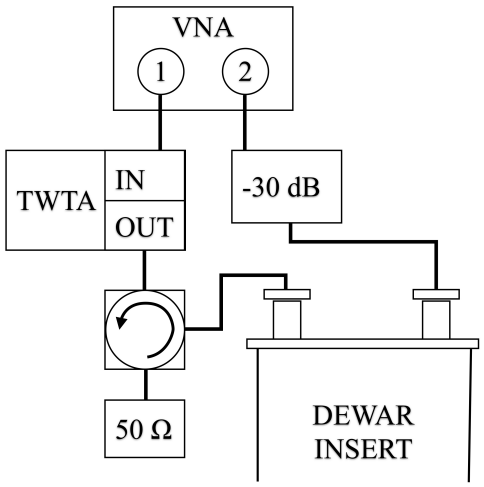

Figure 5.1: Schematic of RF measurement setup. Counter-clockwise from the top, the components are: an Agilent E5071C four-port vector network analyzer; a Varian VZS 6951K1D traveling wave tube amplifier (2-4 GHz, 34.4 dB gain); a UTE Microwave Inc. CT-3041-N circulator (2-4 GHz); a Narda 367NM 50Ω load (2-18 GHz, 40 W max.); the dewar insert described in Chapter 3; and a Narda 769-30 -30 dB attenuator (DC to 6 GHz, 150 W max.).

practice, the TWTA saturates at a maximum of 20 W output power [1]. This is likely because the amplifier is almost 20 years old. Between 14 and 20 W, there is a nonlinear region in which the amplification falls from the nominal 34.4 dB. In this nonlinear region the TWTA can generate harmonics, exciting higher-order modes in the resonator. These first measurements of the control resonator were therefore made in the linear region, below 14 W output power.

[1]The power sensor used with the 437B has a maximum input power of 300 mW. The measurements of output power were therefore made by inserting a Narda 769-30 S-band attenuator in between the amplifier and the power meter. At 2.75 GHz, the 769-30 has an attenuation of -29.8 dB.

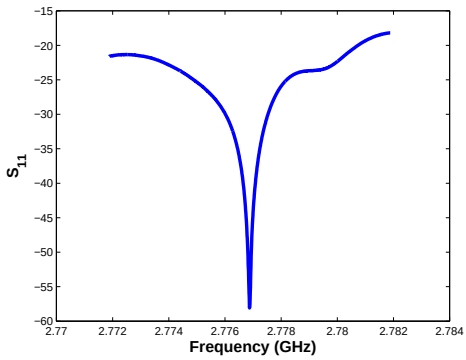

(a) s_{11}

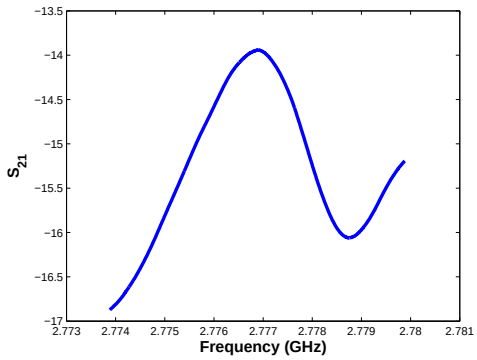

(b) s_{21}

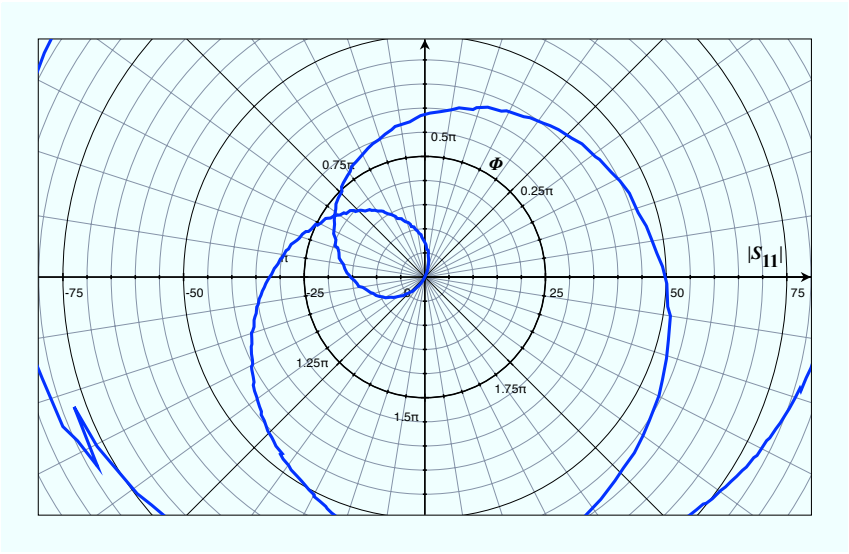

(c) Polar plot, reflection coefficient.

Figure 5.2: A section of the polar plot of S_{11}, showing magnitude $|S_{11}$ (dB) and phase Φ. The passage through the origin indicates critical coupling.

5.2 Measurements and analysis

The TM_{01} mode of the disk resonator was measured at 2.779±0.004 GHz. Critical coupling, as discussed in Section 3.6.2, was easily found and maintained, indicating that the variable couplers function as designed. Figure 5.2c shows a polar plot of S_{11} in the region of the origin, showing zero reflection at 2.78 GHz. The loaded $Q_L = 488 \pm 6$ was calculated from the bandwidth of S_{21} (Figure 5.2b), measured over a range of input power between 2.7 and 13.8 W. Then, from Equation 3.18, $Q_0 = 976 \pm 12$. For reference, recall that from Chapter 3, $Q_0^{\text{calc.}} \approx 1100$. The difference between these values can be accounted for by

losses inherent in the RF measurement circuit, including the 141-R transmission lines.

The multilayer sample shows no resonance for a 100 MHz range about the central frequency. The only difference between this sample and the control is the presence of two thin films: (Nb,Ti)N and Al_2O_3. Large RF surface losses in the thin film layers may explain why no resonance was observed during multilayer testing. Since the (Nb,Ti)N deposition process is still being refined, there is a good opportunity here to test films of different qualities under RF conditions. It's possible that the (Nb,TiN)N films currently being made are simply too lossy for RF applications. This question will be resolved via a further evaluation of the RF surface resistance of sputtered (Nb,Ti)N films, as well as equivalent measurements made with other materials.

5.3 Conclusions

An experimental program has been developed to evaluate the efficacy of multilayer thin film coatings for SRF. A disk resonator was simulated, built, and tested. Supporting systems were also designed and built: a dewar insert to hold and tune the resonator, and to supply RF power during cryogenic tests; and a sample holder to heat and stabilize substrates during UHV deposition. In addition, the production of thin (Nb,Ti)N films in JLab's UHV system was evaluated and improved.

The system works as designed. That is, the resonator operates at the design frequency. Notably, the variable couplers are effective in finding and maintaining a state of critical coupling throughout RF measurements. Q_0 is also close to predicted values.

A comprehensive evaluation of multilayer films will require several more years of experimentation. Films of different materials, with varying thickness and surface roughness, should be tested. This dissertation demonstrates, though, that the system functions and can be used for such a long-term program.

5.4 Future work

Ultimately, a complete multilayer film evaluation should be conducted in such a way that samples can be coated with films and then measured quickly and easily. The main improvement to be made, then, is procedural. The relatively new Thin Film Group

at Jefferson Lab will begin using the disk resonator for multilayer analysis. From an administrative standpoint, the analysis will be incorporated into the broader goals of Jefferson Lab. This means improved access to lab resources, such as a regular place in the VTA schedule.

Apart from administrative improvements, the film deposition process must be refined. Largely, this means completing the commissioning of the UHV system. Mass flow control will be installed, for example. From the perspective of an extended analysis of multilayer films, one significant improvement would be to reconfigure the chamber interior. A center-mount setup would allow several substrates to be coated simultaneously, speeding up sample production and eliminating chamber environment variations between samples. A turntable configuration would allow the magnetrons to be mounted on the chamber walls, freeing up functional space in the chamber and allowing precise masking and patterning of the samples.

Some modifications can be made to the apparatus itself. For example, Figure 3.15 indicates that the TWTA provides insufficient power to quench bulk Nb. Procuring a higher-gain S-band TWTA would solve this problem, but radiative losses could also be reduced by replacing the input coupler with a coaxial probe [133, 134]. Furthermore, the 141-R line used to transmit power through liquid helium to the disk resonator is quite lossy, which makes coupling more difficult. Semirigid, small-diameter heliax line may be a better alternative.

The frequency of the disk resonator is not fixed. That is, testing samples at other frequencies in principle requires only the fabrication of a new disk with a different radius. A disk with an 8 cm diameter could make multilayer measurements at CEBAF's 1.5 GHz, for a more direct evaluation of materials for elliptical cavity applications. Or, a higher frequency could be used to accommodate smaller samples, with the aim of improved control over film uniformity. The only limitation here is the availability of RF amplifiers and other hardware that function at the required frequency.

The UHV system is not the only system capable of producing multilayer coatings. The Thin Film Group at Jefferson Lab is currently exploring methods of energetic deposition via plasma and electron-cyclotron resonance. At Argonne National Lab, atomic layer film

deposition has been generating a fair amount of excitement in the SRF community [116]. And other labs are developing new and promising materials like MgB_2 [59]. Since the disk resonator system only requires flat samples, multilayer substrates do not have to be prepared in-house.

Finally, the disk resonator system has other applications besides an evaluation of multilayer films. The RF surface resistance of various materials can be measured over a broad range of frequencies and temperatures. In addition, there is some debate about the influence of grain boundary density during vortex penetration [132]. To study this phenomenon, Q vs. H curves could be measured for bulk niobium substrates with a broad range of grain boundary densities and surface treatments.

Appendix A

Field solutions in a pillbox cavity

A derivation is presented here of the analytic field solutions in a pillbox cavity. This is an extension of the material in Section 1.2.1.

As stated above, the starting point is a differential equation obtained from Maxwell's equations.

$$\nabla \times \mathbf{E} = -\imath\omega\mu\mathbf{H} \tag{A.1a}$$

$$\nabla \times \mathbf{H} = \imath\omega\epsilon\mathbf{E} + \mathbf{J} \tag{A.1b}$$

$$\nabla \cdot \mathbf{D} = \rho \tag{A.1c}$$

$$\nabla \cdot \mathbf{B} = 0. \tag{A.1d}$$

Within the volume of the cavity $\mathbf{J} = 0$, simplifying Equation A.1b. Solving for H in Equation A.1a and substituting gives

$$\nabla \times \nabla \times \mathbf{E} = \omega^2\epsilon\mu\mathbf{E}. \tag{A.2}$$

The left-hand side of Equation A.2 is simplified by using the vector identity $\nabla \times \nabla \times \mathbf{A} = \nabla(\nabla \cdot \mathbf{A}) - \nabla^2\mathbf{A}$ and Equation A.1c, which gives $\nabla \cdot \mathbf{E} = 0$. Then

$$\nabla^2\mathbf{E} + \epsilon\mu\omega^2\mathbf{E} = 0.$$

In cylindrical coordinates (r, ϕ, z),

$$\frac{1}{\rho}\frac{\partial E_z}{\partial \rho}\left(\rho\frac{\partial E_z}{\partial \rho}\right) + \frac{1}{\rho^2}\frac{\partial^2 E_z}{\partial \phi^2} + \frac{\partial^2 E_z}{\partial z^2} + \omega^2\mu\epsilon E_z = 0. \tag{A.3}$$

A solution to Equation A.3 is obtained using the separation of variables approach. Assuming that each of the coordinate dependencies of E_z can be factored,

$$E_z(\rho, \phi, z) = R(\rho)P(\phi)Z(z).$$

The boundary conditions at $z = 0, L$ require $Z(z) = \sin(\beta z)$. Substituting the above form into Equation A.3, multiplying by ρ^2, and dividing by RPZ gives

$$\frac{\rho}{R}\frac{\partial}{\partial\rho}\left(\rho\frac{\partial R}{\partial\rho}\right) + \frac{1}{P}\frac{\partial^2 P}{\partial\phi^2} + \rho^2(\omega^2\mu\epsilon - \beta^2) = 0.$$

Both of these terms are then independent of the other and can therefore each be expressed as a separation constant. That is,

$$\frac{1}{P}\frac{\partial^2 P}{\partial\phi^2} \equiv n^2$$

which can be solved by inspection:

$$P(\phi) = E_0' \cos(n\phi). \tag{A.4}$$

(An arbitrary choice of phase, $\phi \rightarrow \phi + \phi_0$, allows Equation A.4 to be expressed in simplified form, rather than as a linear combination of sines and cosines. The associated coefficient is rolled into E_0.)

$R(\rho)$ is similarly solved.

$$\frac{\rho}{R}\frac{\partial}{\partial\rho}\left(\rho\frac{\partial R}{\partial\rho}\right) - n^2 + \rho^2(\omega^2\mu\epsilon - \beta^2) = 0.$$

This is Bessel's equation and the solution is a linear combination of Bessel functions, $R(\rho) = AJ_n(k_c\rho) + BY_n(k_c\rho)$. A cutoff wavenumber is defined, $k_c^2 \equiv \omega^2\mu\epsilon - \beta^2$. The cutoff wavenumber is so called because for small values of ω, the argument $k_c\rho$ becomes imaginary[1]. In physical terms, the cavity fields are evanescent and propagation gives way to attenuation. Finally, note that $Y_n(k_c\rho)$ is singular at $\rho \rightarrow 0$. Physical solutions then require $B = 0$. The full field solution is therefore

$$E_z(\rho, \phi, z) = E_0 J_n(k_c\rho)\cos(n\phi)\sin(\beta z). \tag{A.5}$$

[1]In fact, the "cutoff frequency" is a more widely-used term.

The boundary condition $E_z(z = L) = 0$ constrains the possible values of β such that $\sin(\beta\ell) = 0$, or $\beta = p\pi/\ell$ where p is an integer. Similarly, k_c is constrained at the outer radius R of the cavity.

$$E_z(\rho = R) = 0 \qquad \Rightarrow \qquad J_n(k_c R) = 0$$

so $k_c R$ must equal x_{mn}, the set of zeroes to the Bessel function J_n.

$$k_c^2 = k^2 - \beta^2$$
$$\frac{x_{nm}^2}{R^2} = \omega^2\mu\epsilon - \frac{p^2\pi^2}{\ell^2}$$

or, solving for the resonant frequency $f = \omega/2\pi$,

$$f_{nmp} = \frac{c}{2\pi\sqrt{\mu\epsilon_r}}\sqrt{\left(\frac{x_{mn}}{R}\right)^2 + \left(\frac{p\pi}{\ell}\right)^2}. \tag{A.6}$$

Implicit in the above statement is the relation between c and the dielectric constant ϵ_r. That is, $c = 1/\sqrt{\mu\epsilon_0\epsilon_r}$. The cavity material here is assumed to be nonmagnetic, such that $\mu = \mu_0$.

The indices (n, m, p) give the various eigenfrequencies of the cavity fields. The fundamental, accelerating mode is denoted TM_{010}. Since $n = p = 0$ and $\beta = 0$ for this mode, Equation A.6 simplifies to

$$f_{010} = \frac{c}{2\pi\sqrt{\epsilon_r}}\left|\frac{x_{nm}}{R}\right|.$$

For $\ell = 10$ cm and $\epsilon_r = 1$ (i.e. vacuum), $f_{010} = 1.1$ GHz. The magnetic field corresponding to Equation A.5 is found directly using Maxwell's equations, specifically Equation A.1a. For the TM_{010} mode,

$$\mathbf{H}(\mathrm{TM}_{010}) = -\frac{\imath E_0}{\eta}J_1(k\rho)\hat{\phi} \tag{A.7}$$

where $\eta = \sqrt{\mu/\epsilon} = 377\ \Omega$ is the wave impedance of free space.

Bibliography

[1] A. Gurevich, Applied Physics Letters **88**, 1 (2006).

[2] J. Cockcroft and E. Walton, Proc. of the Royal Society A **129**, 477 (1930).

[3] J. Cockcroft and E. Walton, Proc. of the Royal Society A **137**, 229 (1932).

[4] R. Van de Graaff, K. Compton, and L. Van Atta, Phys. Rev. **43**, 149 (1933).

[5] L. Van Atta, D. Northrup, C. Van Atta, and R. Van de Graaff, Phys. Rev. **49**, 761 (1936).

[6] T. Aitken, Nuclear Instruments and Methods in Physics Research A **338**, 10 (1993).

[7] G. Alton and J. Beene, J. Phys. G: Nucl. Part. Phys. **24**, 1347 (1998).

[8] G. Norton and J. Duggan, in *Handbook of accelerator physics and engineering*, 3rd ed., edited by A. Chao and M. Tigner (World Scientific Publishing Co. Pte. Ltd., Hackensack, NJ, 2006), Chap. 1.6.10, p. 30.

[9] E. Lawrence and M. Livingston, Phys. Rev. **40**, 19 (1930).

[10] A. Grinberg, Sov. Phys. Usp. **18**, 815 (1975).

[11] R. Wideroe, in *The Infancy of Particle Accelerators: Life and Work of Rolf Wideröe*, edited by P. Waloschek (Friedr. Vieweg Verlagsgesellschaft, London, UK, 1994), No. DESY-Red-Report 94-039.

[12] D. Sloan and E. Lawrence, Phys. Rev. **38**, 2021 (1931).

[13] L. Brillouin, Phys. Rev. **74**, 90 (1948).

[14] L. Brillouin, J. Phys. Radium **1**, 377 (1930).

[15] L. Brillouin, Proc. of the National Academy of Sciences **41**, 401 (1955).

[16] S. Lee, *Accelerator Physics*, 2nd ed. (World Scientific Publishing Co. Pte. Ltd., Hackensack, NJ, 2004).

[17] P. Farnsworth, Multipactor phase control, U.S. Patent 2,071,517, 1935.

[18] W. Gallagher, in *Proc. of the 1989 Particle Accelerator Conference*, IEEE (, Chicago, IL, USA, 1989), pp. 2008–2009.

[19] P. Kneisel, O. Stoltz, and J. Halbritter, J. Appl. Phys. **44**, 1785 (1973).

[20] J. Halbritter, in *Proc. 1st Workshop on RF Superconductivity*, edited by M. Kuntze (Kernforschungszentrum Karlsruhe, Karlsruhe, Germany, 1980), No. KfK-3019, pp. 190–214.

[21] H. Padamsee and A. Joshi, J. Appl. Phys. **50**, 1112 (1979).

[22] H. Piel, in *Proc. 1st Workshop on RF Superconductivity* (Kernforschungszentrum Karlsruhe, Karlsruhe, Germany, 1980), No. KfK-3019, pp. 85–118.

[23] P. Kneisel, IEEE Transactions on Applied Superconductivity **9**, 1023 (1999).

[24] R. Sundelin, IEEE Transactions on Nuclear Science **NS-32**, 3570 (1985).

[25] H. A. Grunder *et al.*, Nuclear Physics A **478**, 831 (1988).

[26] H. Padamsee and et al., in *Proc. of the 1991 Particle Accelerator Conference* (IEEE, San Francisco, CA, 1991), pp. 786–788.

[27] G. Ciovati and et al., in *Proc. 10th Workshop on RF Superconductivity* (, Tsukuba, Japan, 2001), No. PT016, pp. 512–516.

[28] W. Weingarten, in *Proc. 7th Workshop on RF Superconductivity*, CERN (, Gif-sur-Yvette, France, 1995), No. CERN-SL-95-122 RF, pp. 23–26.

[29] R. Geng, G. Eremeev, H. Padamsee, and V. Shemelin, in *Proceedings of PAC07*, IEEE (, Albuquerque, New Mexico, USA, 2007), No. WEPMS006, pp. 2337–2339.

[30] H. Hayano, in *Proceedings of 2005 Particle Accelerator Conference* (IEEE, Knoxville, TN, 2005), No. WOAA002.

[31] ITRP, Technical report, ILC (unpublished).

[32] J. Wang *et al.*, in *Proceedings of the 1995 Particle Accelerator Conference* (IEEE, Dallas, Texas, USA, 1995), Vol. 1, pp. 653–655.

[33] E. Vogt, IEEE Transactions on Nuclear Science **NS-30**, 3684 (1983).

[34] J. Calarco *et al.*, IEEE Transactions on Nuclear Science **NS-24**, 1091 (1977).

[35] J. Halbritter, Z. Physik **266**, 209 (1974).

[36] H. Padamsee, J. Knobloch, and T. Hays, *RF Superconductivity for Accelerators*, 2nd ed. (Wiley-VCH Verlag GmbH & Co. KGaA, Weinheim, Germany, 2008).

[37] D. Boussard and T. Linnecar, in *Proceedings of the 1999 Cryogenic Engineering and International Cryogenic Materials Conference* (CE-ICM, Montreal, Canada, 1999), No. LHC-PR-316.

[38] M. Tinkham, *Introduction to Superconductivity*, 2nd ed. (Dover Publications, Inc., Mineola, NY, USA, 1996).

[39] A. Leggett, *Quantum Liquids: Bose condensation and Cooper pairing in condensed-matter systems* (Oxford University Press, Oxford, England, 2006).

[40] A. Abrikosov, L. Gorkov, and I. Dzyaloshinski, in *Methods of Quantum Field Theory in Statistical Physics*, 2nd ed., edited by R. A. Silverman (Prentice-Hall, Inc., Edgewood Cliffs, NJ, USA, 1963).

[41] C. Kittel, *Quantum Theory of Solids*, 2nd ed. (J. Wiley & Sons, Inc., New York, NY, 1963).

[42] F. London and H. London, in *Proceedings of the Royal Society of London*, No. 866 in *A: Mathematical and Physical Sciences* (The Royal Society, London, UK, 1935), pp. 71–88.

[43] R. Cohen and B. Abeles, Phys. Rev. **168**, 167 (1968).

[44] K. Kanoda *et al.*, Phys. Rev. Lett. **65**, 1271 (1990).

[45] J. Bardeen, L. Cooper, and J. Scrieffer, Physical Review **108**, 1175 (1957).

[46] K. Saito, in *Proceedings of the 2003 Particle Accelerator Conference*, IEEE (, Portland, OR, USA, 2003), pp. 462–466.

[47] T. Yogi, G. Dick, and J. Mercereau, Phys. Rev. Lett. **39**, 826 (1977).

[48] D. Proch, Reports on Progress in Physics **61**, 431 (1998).

[49] A. Valente-Feliciano, in *Proc. 13th Workshop on RF Superconductivity* (Beijing University, Beijing, China, 2007).

[50] S. Deambrosis *et al.*, in *Proceedings of the 14th International Conference on RF Superconductivity* (pending publication, Berlin, Germany, 2009), No. TUOBAU07.

[51] C. Leemann, D. Doublas, and G. Krafft, Annu. Rev. Nucl. Part. Sci. **51**, 413 (2001).

[52] P. Kneisel, G. Myneni, and G. Ciovati, in *Proceedings of 2005 Particle Accelerator Conference* (IEEE, Knoxville, TN, 2005), No. TPPT076.

[53] R. Geng, H. Padamsee, A. Seaman, and V. Shemelin, in *Proceedings of 2005 Particle Accelerator Conference*, PAC (, Knoxville, TN, 2005), No. ROAC009.

[54] G. Wu, L. Cooley, C. Antoine, and H. Edwards, in *Proceedings of SRF2007*, SRF (Peking University, Beijing, China, 2007), No. TU204.

[55] P. Bauer *et al.*, in *Proc. 12th International Workshop on RF Superconductivity* (, Ithaca, NY, 2005).

[56] H. Wang *et al.*, in *Proceedings of 2005 Particle Accelerator Conference*, PAC (IEEE, Knoxville, TN, 2005), No. TPPT085.

[57] P. Fabbricatore and et al., IEEE Transactions on Applied Superconductivity **3**, 1761 (1993).

[58] A. Rossi *et al.*, in *Proceedings of the 14th International Conference on RF Superconductivity* (pending publication, Berlin, Germany, 2009), No. TUOBAU06.

[59] T. Tajima and et al., in *Proceedings of the 2006 Applied Superconductivity Conference* (IEEE, Seattle, WA, USA, 2006), No. LA-UR-06-6143.

[60] C. Wyss, in *Record of the 1991 IEEE Particle Accelerator Conference* (IEEE, San Francisco, CA, USA, 1991), pp. 150–152 vol. 1.

[61] R. Di Leo, A. Nigro, G. Nobile, and R. Vaglio, Journal of Low-Temperature Physics **78**, 41 (1990).

[62] G. Stejic *et al.*, Phys. Rev. B **49**, 1274 (1994).

[63] M. Marino, in *Proc. 8th Workshop on RF Superconductivity*, CERN (, Abano-Terme, Italy, 1997), Vol. 1-4, pp. 1074–1080.

[64] S. Bedorf, Ph.D. thesis, University of Köln, Köln, Germany, 2005.

[65] A. Gurevich and R. Mints, Rev. Mod. Phys. **59**, 941 (1987).

[66] Z. Zhang and M. Lagally, Science **276**, 377 (1997).

[67] I. Petrov and et al., J. Vac. Sci. Technol. A **21**, S117 (2003).

[68] B. Josephson, Rev. Mod. Phys. **36**, 216 (1964).

[69] N. Lütke-Entrup, B. Plaçais, P. Mathieu, and Y. Simon, Phys. Rev. Lett. **79**, 2538 (1997).

[70] D. Vodolazov, I. Maksimov, and E. Brandt, Physica C **384**, 211 (2003).

[71] C. Antoine and et al., in *Proceedings of the 14th International Conference on RF Superconductivity* (SRF, Berlin, Germany, 2009), No. TUPPO070.

[72] R. Russo and et al., IEEE Transactions on Applied Superconductivity **19**, 1394 (2009).

[73] L. Lilje, in *Proc. Linear Accelerator Conference* (, Lübeck, Germany, 2004), No. WE102.

[74] G. Ciovati *et al.*, Physical Review Special Topics - Accelerators and Beams **13**, 1 (2010).

[75] C. Reece and et al., in *Proceedings of 2005 Particle Accelerator Conference*, IEEE (, Knoxville, TN, 2005), pp. 4081–4083.

[76] K. Saito and et al., in *Proc. 14th International Conference on RF Superconductivity* (, Berlin, Germany, 2009), No. THOAAU05, pp. 467–472.

[77] G. Ciovati *et al.*, in *Proc. 13th International Workshop on RF Superconductivity* (, Beijing, China, 2007).

[78] A. Derneryd, IEEE Transactions on Antennas and Propagation **AP-27**, 660 (1979).

[79] A. Jenkins *et al.*, IEEE Transactions on Applied Superconductivity **7**, 2793 (1997).

[80] I. Wolff and N. Knoppik, IEEE Transactions on Microwave Theory and Techniques **MTT-22**, 857 (1974).

[81] C. Grebenkemper and J. Hagen, Phys. Rev. **80**, 89 (1950).

[82] N. M. Alford and et al., Journal of the European Ceramic Society **21**, 2605 (2001).

[83] A. Bhattacharyya and R. Garg, IEEE Transactions on Antennas and Propagation **AP-33**, 1067 (1985).

[84] T. Itoh and W. Menzel, IEEE Transactions on Antennas and Propagation **AP-29**, 63 (1981).

[85] J. James and G. Wilson, Microwaves, Optics and Acoustics **1**, 165 (1977).

[86] W. Harokopus and et al., IEEE Transactions on Microwave Theory and Techniques **39**, 1098 (1991).

[87] M. Bartsch and et al., Computer Physics Communications **72**, 22 (1992).

[88] T. Weiland, International Journal of Numerical Modeling: Electronic Networks, Devices and Fields **9**, 295 (1996).

[89] A. Andreone and et al., J. Appl. Phys. **73**, 4500 (1993).

[90] C. Benvenuti, P. Chiggiato, L. Parrini, and R. Russo, Nuclear Instruments and Methods in Physics Research B **124**, 106 (1997).

[91] N. Iosad and et al., IEEE Transactions on Applied Superconductivity **11**, 3832 (2001).

[92] H. Myoren and et al., IEEE Transactions on Applied Superconductivity **11**, 3828 (2001).

[93] C. Reece, J. Susta, T. Powers, and B. Almeida, in *Proceedings of the 1991 Particle Accelerator Conference* (IEEE, San Francisco, CA, USA, 1991), pp. 2325–2327.

[94] R. Barron, in *Cryogenic Systems*, 2nd ed., edited by R. Scurlock (Oxford University Press, New York, NY, 1985).

[95] S. Cantacuzéne *et al.*, in *Proceedings of European Particle Accelerator Conference* (, Lucerne, Switzerland, 1994), pp. 2074–2076.

[96] B. Jackson and et al., J. Appl. Phys. **97**, 1 (2005).

[97] C. Tong and et al., in *Proc. 12th International Symposium on Space Terahertz Technology*, edited by I. Mehdi (, Pasadena, CA, 2001), pp. 253–261.

[98] S. Boelens and H. Veltrop, Surface and Coatings Technology **33**, 63 (1987).

[99] U. König, Surface and Coatings Technology **33**, 91 (1987).

[100] *Handbook of Ternary Alloy Phase Diagrams*, edited by P. Villars, A. Prince, and H. Okamoto (ASM International, Materials Park, OH, USA, 1995), Vol. 10.

[101] V. Buscaglia and et al., Journal of Alloys and Compounds **226**, 232 (1995).

[102] E. Felten, Journal of the Less-Common Metals **17**, 207 (1969).

[103] V. Buscaglia and et al., Journal of Alloys and Compounds **283**, 241 (1999).

[104] C. Yen and et al., J. Appl. Phys. **38**, 2268 (1967).

[105] E. Cukauskas, W. Carter, and S. Qadri, J. Appl. Phys. **57**, 2538 (1985).

[106] Z. Wang and et al., J. Appl. Phys. **79**, 7837 (1996).

[107] V. Zhitomirsky and et al., Thin Solid Films **326**, 134 (1998).

[108] *Binary Alloy Phase Diagrams*, 2nd ed., edited by T. Massalski, H. Okamoto, P. Subramanian, and L. Kacprzak (ASM International, Metals Park, OH, USA, 1990), Vol. 3.

[109] R. Reed-Hill and R. Abbaschian, *Physical Metallurgy Principles*, 3rd ed. (PWS-Kent Pub., Boston, MA, USA, 1992).

[110] in *Powder Diffraction File*, edited by S. Kabekkodu (International Centre for Diffraction Data, Newton Square, PA, USA, 2011).

[111] E. Cukauskas, J. Appl. Phys. **54**, 1013 (1983).

[112] A.-M. Valente-Feliciano *et al.*, in *Proceedings of the 14th International Conference on RF Superconductivity* (, Berlin, Germany, 2009), No. TUPPO084.

[113] M. Voigt and M. Sokolowski, Materials Science and Engineering B **109**, 99 (2004).

[114] M. Voigt and et al., J. Vac. Sci. Technol. A **27**, 234 (2009).

[115] B. Segda, M. Jacquet, and J. Besse, Vacuum **62**, 27 (2001).

[116] T. Proslier and et al., Applied Physics Letters **93**, 1 (2008).

[117] B. Argent and B. Phelps, Journal of the Less-Common Metals **2**, 181 (1960).

[118] G. Jouve, C. Séverac, and S. Cantacuzéne, Thin Solid Films **287**, 146 (1996).

[119] G. Wu, Ph.D. thesis, Virginia Polytechnic Institute, Blacksburg, VA, USA, 2002.

[120] T. Matsunaga, H. Maezawa, and T. Noguchi, IEEE Transactions on Applied Superconductivity **13**, 3284 (2003).

[121] P. Bosland, F. Guémas, and M. Juillard, in *Proceedings of European Particle Accelerator Conference* (, Paris, France, 1992), pp. 1316–1318.

[122] I. Safi, Surface and Coatings Technology **127**, 203 (2000).

[123] L.-J. Meng and M. dos Santos, Surface and Coatings Technology **90**, 64 (1997).

[124] J. Thornton, J. Vac. Sci. Technol. A **4**, 3059 (1986).

[125] Z.-J. Liu and et al., J. Appl. Phys. **92**, 3559 (2002).

[126] J. Goldstein and et al., *Scanning electron microscopy and x-ray microanalysis*, 3rd ed. (Springer Science + Business Media, Inc., New York, NY, 2003).

[127] B. Cullity and S. Stock, *Elements of x-ray diffraction*, 3rd ed. (Prentice-Hall, Inc., New York, NY, 2001).

[128] M. Torche and et al., Thin Solid Films **436**, 208 (2003).

[129] J. Sundgren, Thin Solid Films **128**, 21 (1985).

[130] A. Denton and N. Ashcroft, Physical Review A **43**, 3161 (1991).

[131] A. Patterson, Phys. Rev. **56**, 978 (1939).

[132] P. Lee and et al., Physica C **441**, 126 (2006).

[133] A. Tulintseff and S. Ali, IEEE Transactions on Antennas and Propagation **39**, 381 (1991).

[134] M. Davidovitz and Y. Lo, IEEE Transactions on Antennas and Propagation **AP-34**, 905 (1986).